PUBLICATIONS OF
THE UNIVERSITY OF EASTERN FINLAND

Dissertations in Forestry and Natural Sciences

ANTONIE DANIËL VERHOEVEN

DIFFRACTIVE ELEMENT DESIGN THEORY AND SPATIAL COHERENCE IN X-RAY BEAMLINE

UNIVERSITY OF
EASTERN FINLAND

PUBLICATIONS OF THE UNIVERSITY OF EASTERN FINLAND
DISSERTATIONS IN FORESTRY AND NATURAL SCIENCES

N:o 367

Antonie Daniël Verhoeven

DIFFRACTIVE ELEMENT DESIGN THEORY AND SPATIAL COHERENCE IN X-RAY BEAMLINE

ACADEMIC DISSERTATION

To be presented by the permission of the Faculty of Science and Forestry for public examination in the Auditorium M101 in Metria Building at the University of Eastern Finland, Joensuu, on December 20th, 2019, at 12 o'clock noon.

University of Eastern Finland
Department of Physics and Mathematics
Joensuu 2019

Grano Oy
Jyväskylä, 2019
Editors: Pertti Pasanen, Raine Kortet,
Jukka Tuomela, and Matti Tedre

Distribution:
University of Eastern Finland Library / Sales of publications
julkaisumyynti@uef.fi
http://www.uef.fi/kirjasto

ISBN: 978-952-61-3289-7 (print)
ISSNL: 1798-5668
ISSN: 1798-5668
ISBN: 978-952-61-3281-4 (pdf)
ISSNL: 1798-5668
ISSN: 1798-5668

Author's address:
University of Eastern Finland
Department of Physics and Mathematics
P.O. Box 111
80101 JOENSUU
FINLAND
email: antonie.verhoeven@uef.fi

Supervisors:
Professor Jari Turunen
University of Eastern Finland
Department of Physics and Mathematics
P.O. Box 111
80101 KUOPIO
FINLAND
email: jari.turuen@uef.fi

Professor Frank Wyrowski
Friedrich-Schiller-University
Institute of Applied Physics
Albert-Einstein-Strasse 15
D-07745 Jena
Germany
email:frank.wyrowski@uni-jena.de

Reviewers:
Adjunct Professor Mihail Dumitrescu
Tampere University of Technology
Optoelectonics Research Centre
33014 Tampere
FINLAND
email: mihail.m.dumitrescu@gmail.com

Dr. Hagen Schweitzer
Jenoptik Optical Systems
07745 Jena
Germany
email: hagenschweitzer@gmx.de

Opponent:
D.Sc. (Tech.), Doc. Andriy Shevchenko
Aalto University
Department of Applied Physics
P.O. Box 13500
00076 Aalto
FINLAND
email: andriy.schevchenko@aalto.fi

Antonie Daniël Verhoeven
Diffractive element design theory and spatial coherence in X-ray beamline 367: University of Eastern Finland, Joensuu
Publications of the University of Eastern Finland
Dissertations in Forestry and Natural Sciences
2019

ABSTRACT

This work contains several theoretical and numerical studies on diffractive optics with absorbing media and modeling of a x-ray optics setup. The first part of the work is devoted to the theory and design of diffractive elements on the basis of scalar diffraction theory. A general upper bound theorem is introduced. This theory is incorporated into a diffractive element design method for lossy diffractive elements based on the Iterative Fourier-Transform Algorithm (IFTA). The resulting method is used to investigate and design diffractive elements made with absorbing media. In the second part of the work the spatial coherence theory is introduced. From this the elementary mode description for spatially partially coherent light is derived and applied to x-ray sources. The modeling methods for field propagation are described and used with the x-ray source description to determine the focal spot of a grazing mirror beam-line setup.

Universal Decimal Classification: *53.084.85, 535.3, 535.4, 681.7.02*
OCIS codes: *340.7440, 110.7440*
Keywords: *Optics; micro-optics; diffraction gratings; diffractive optics; X-ray imaging; light propagation; modeling; wavefront propagation; x-ray optics simulation*

ACKNOWLEDGEMENTS

First and foremost I wish to thank both Prof. Jari Turunen and Prof. Frank Wyrowski for their diligence, patience and guidance they have provided throughout my PhD. Their help has been an invaluable asset throughout my PhD, both when discussing the topics found in this thesis and in what direction to go.

I also wish to take this time to thank Mr. Weingaard, Dr. N. Bhattacharya and Dr. M. Zeitouny, people who changed the course of my life, inspired me and guided me to reach the place I got to now.

My thanks also go out to my parents for their care, love and support and ofcourse my brother and sister for being there at inconvenient times.

Lastly I wish to thank my friends and fellow students who made me feel at home in UEF. Special shoutouts go to Gaurav & Bisrat who I often saw outside of office hours and Matias & Henri who were excellent people to have as office-mates.

Joensuu, September 21, 2019

Antonie Daniël Verhoeven

LIST OF PUBLICATIONS

This thesis consists of the present review of the author's work in the field of optical phenomena and the following selection of the author's publications:

I G. Bose, A.D. Verhoeven, I. Vartiainen, M. Roussey, M. Kuittinen, J. Tervo and J. Turunen, "Diffractive optics based on modulated subwavelength-domain V-ridge gratings," *J. Opt.* **18**, 085602 (2016).

II A.D. Verhoeven, H. Aagedal, F. Wyrowski and J. Turunen, "Upper bound of signal-relevant efficiency of constrained diffractive elements," *J. Opt. Soc. Am. A* **33** 2425–2430 (2016).

III A.D. Verhoeven, F. Wyrowksi and J. Turunen, "Iterative design of diffractive elements made of lossy material," *J. Opt. Soc. Am. A* **35**, 45–54 (2018).

IV A.D. Verhoeven, C. Hellmann, F. Wyrowski, M. Idir and J. Turunen, "Genuine-field modeling of partially coherent X-ray imaging systems,"*J. Synchrotron Rad.*, submitted for publication (2019).

Throughout the overview, these papers will be referred to by Roman numerals.

AUTHOR'S CONTRIBUTION

The publications selected in this dissertation are original research papers in the field of diffractive optics and x-ray optics simulation. All publications are the result of group work. The author has developed the ideas in collaboration with the co-authors. He was responsible for designing and analyzing the diffractive element described in Paper I. Regarding the theoretical papers II-IV, he participated actively in working out the theory ,was responsible for writing the design algorithms and analyzing the results. He had a key role in writing each of the manuscripts.

TABLE OF CONTENTS

1 Introduction

In everyday life we see light all around us, coloring the surfaces we see. Some surfaces such as the CD and DVD disks show colorful rainbow patters when illuminated. These patterns occur because the CD and DVD contain a very regular grid of dips and divots in their surface due to the way we store data on them. These regular patterns of tiny structures are referred to as gratings and cause the different colors to propagate in different and multiple directions. The optical principle responsible for this is called diffraction and is used to design optical elements that do exactly that: split the light into multiple light beams and/or send the different colors in strongly different directions.

In certain cases it can become useful or necessary to take absorption into account when designing these optical elements. For instance, when designing for very short wavelengths such as Deep Ultra Violet light. In this region most materials and media that are transparent to the light we see start absorbing the light instead. Therefore the use of thin or reflecting elements such as (thin) gratings can become advantageous to use over bulky lens elements. Another domain where absorption can also come into play is when a set of microstructure's of similar size to the wavelength of light is used to create a grating. These domains are the main focus when covering diffractive element design theory in this thesis.

When moving to even smaller wavelengths of light the photons will eventually be referred to as X-rays. These highly energetic photons are among other things used to image tiny structures such as the structure of molecules and atoms themselves. The problem however is that these X-rays tend to fly straight through materials and be absorbed only if the material is dense and thick enough. As such creating the tiny focal spot that is needed with lens systems is out of the question. In practice gratings are used but these tend to lose much of light as they split the light into multiple directions while only the direction that goes to the focus is of interest. Another way to focus the light is by using grazing mirrors. To reflect the majority of the X-rays gold coated mirrors are orientated such that the X-ray graces the mirror surface with angles on the order of fractions of a degree. These small grazing angles cause the setup to become many meters long and such setups are typically referred to as X-ray beam lines. As these setups are time-consuming and expensive to make, accurate modeling of them is highly desired. This is the focus of the second part of this thesis.

The thesis is organized as follows. In chapter 2 introduces the mathematics behind the concept of Signal Relevant Efficiency (SRE) along with its upper bound. In chapter 3 the scalar theory of diffraction is introduced when considering lossy media and the theory from chapter 2 is applied to a scalar diffraction element design algorithm, enabling higher quality design of beam-splitters and holographic elements with lossy materials. Chapter 4 shows the results of this design algorithm when considering lossy media or loss induced by micro-structures structured as gratings and functioning as beam splitters. Chapter 5 introduces the spatial coherence theory for X-ray sources while Chapter 6 explains which methods are used to propagate wavefronts accurately and quickly. Chapter 7 details the grazing mirror

X-ray beam-line setup to be simulated and shows the results when the description and methods provided in Chapters 5 and 6 are used. Some conclusions are drawn in Chapter 8. The more mathematically focused derivations have been placed in appendices for ease of navigating this thesis.

2 Signal Relevant Efficiency

The Signal Relevant Efficiency (SRE) describes how much of the energy that goes into the system ends up in a specified output function. This way of representing efficiency originates from [1] and will be used extensively when talking about the design of diffractive optical elements.

In this chapter the mathematical concepts to describe and define the SRE are introduced. First the definitions of fields along with the general description of the optical system are given. In the sections that follows the concept of SRE is explained. The chapter ends with deriving the upper bound of said SRE as this will be used both conceptually and as a tool throughout the diffractive optics design part of the thesis.

2.1 DEFINITIONS

The systems that are considered here are assumed to lie in the domain of scalar optics where a single electric field $E(\mathbf{r}, t)$ component of light at position $\mathbf{r} = (\rho, z) = (x, y, z)$ and time t is considered. At times it is more convenient to represent the field in frequency domain where [2]

$$E(\mathbf{r}, \omega) = \frac{1}{2\pi} \int_{-\infty}^{\infty} E(\mathbf{r}, t) \exp(i\omega t) dt \tag{2.1}$$

defines the field in frequency domain at frequency $\omega = 2\pi c/\lambda$ and inversely

$$E(\mathbf{r}, t) = \int_{0}^{\infty} E(\mathbf{r}, \omega) \exp(-i\omega t) d\omega \tag{2.2}$$

expresses the temporal field.

The scalar field $E(\mathbf{r}, \omega)$ is assumed to be of finite energy and therefore square integrable, allowing it to be defined on a set of orthonormal basis functions and with that defined in the Hilbert space. In this Hilbert space the inner product between two fields at plane z can be expressed as

$$\langle E_1 | E_2 \rangle := \int_{\mathcal{R}^2} E_1(\rho, z, \omega) E_2^*(\rho, z, \omega) d\rho, \tag{2.3}$$

with $\mathcal{R}^2$ the area/plane where the field is considered and $*$ denoting conjugation. The norm of the field is correlated to the amount of energy in it and is given by

$$||E|| = \sqrt{\langle E | E \rangle}. \tag{2.4}$$

In these equations the coordinates have been omitted for the sake of brevity and this abbreviation will be used extensively in the upcoming chapters.

2.2 SYSTEM REPRESENTATION

An optical system can, in a very broad sense, be divided into an input plane where a field is defined, an optical system through which this field is propagated and an output plane at the end of the optical system. The input and output planes are connected by the propagation operator $\mathbf{L}$ that propagates the input field through the system and computes the output field

$$E_{\text{out}}(\widetilde{\rho}, \omega) = \mathbf{L}\left\{E_{\text{in}}(\rho, \omega)\right\}. \tag{2.5}$$

For the purpose of diffractive optics design the propagation operator $\mathbf{L}$ is assumed to be linear meaning that the statements $\mathbf{L}\left\{E_1 + E_2\right\} = \mathbf{L}\left\{E_1\right\} + \mathbf{L}\left\{E_2\right\}$ and $\mathbf{L}\left\{a \cdot E\right\} = a \cdot \mathbf{L}\left\{E\right\}$ are true for any given fields E_1, E_2 and a scalar a. It is also assumed that the operator $\mathbf{L}$ is invertible so that the input field is uniquely defined by the output $E_{\text{in}} = \mathbf{L}^{-1}\left\{E_{\text{out}}\right\}$. The form of the linear operator depends on the system and can be for example a Fresnel propagation operator, Fourier transform, or Collins operator describing a paraxial lens system [3].

A general illustration of such a system is shown in Figure 2.1. In this system the location where the desired output of the field E_{desired} is defined is called the signal window W.

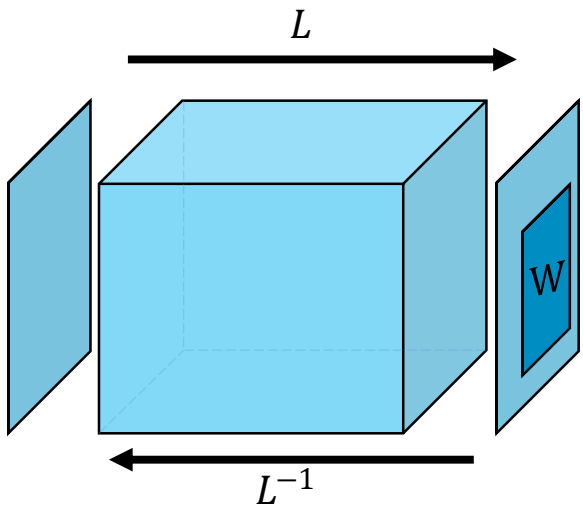

Figure 2.1: A general optical system can be divided into an input plane, output plane and optical system in between. The fields are assumed to be scalar and the operator $\mathbf{L}$ that propagates the field through the system and computes the output field is assumed to be linear and invertible. The area denoted by W in the output plane is referred to as the signal window.

2.3 SIGNAL RELEVANT EFFICIENCY

When designing or testing an optical system the output field E_{out} that is produced typically does not match what was desired E_{desired}. To quantify this mismatch the

output field can be divided into three separate contributions. The first contribution is the field outside the defined signal window and will be referred to as E_{freedom} for in this region no constraints or expectations are placed on the field. Inside the signal window area W the part of the field that matches the desired outcome falls under E_{desired} while the rest is attributed to errors as E_{err}.

This decomposition can always be done uniquely as the three subspaces the field is divided into span the entire possibility space and lie orthogonal with respect to each other, that is to say the inner product given by Eq. (2.3) between any two different components is always zero. This is guaranteed by that inside the signal window W the contribution E_{desired} is orthogonal to E_{err} by definition. The contribution E_{freedom} shares no spatial coordinate with the other two and is therefore orthogonal to both.

The output can therefore be represented as a decomposition into these subspaces;

$$E_{\text{out}} = \alpha E_{\text{desired}} + E_{\text{error}} + E_{\text{freedom}}. \tag{2.6}$$

Here α is the direct measure of the amount of desired field in the output, its value is obtained by projecting E_{out} onto the subspace spanned by E_{desired}:

$$\alpha = \frac{\langle E_{\text{out}} | E_{\text{desired}} \rangle}{\langle E_{\text{desired}} | E_{\text{desired}} \rangle}. \tag{2.7}$$

Using the fact that projections are invariant under linear operations in Hilbert space [4] the quantity α can also be computed by using the field at the input plane:

$$\alpha = \frac{\left\langle E_{\text{in}} | \mathbf{L}^{-1} \left\{ E_{\text{desired}} \right\} \right\rangle}{\langle E_{\text{desired}} | E_{\text{desired}} \rangle}. \tag{2.8}$$

From here the Signal Relevant Efficiency (SRE) can be defined as the proportion of the incident field's power that ends up in the desired output signal which is mathematically expressed as

$$\eta_{\text{SRE}} = \frac{||\alpha E_{\text{desired}}||^2}{||E_{\text{in}}||^2}. \tag{2.9}$$

When Eq. (2.9) is combined with Eq. (2.7) the SRE can be written as

$$\eta_{\text{SRE}} = \frac{|\langle E_{\text{out}} | E_{\text{desired}} \rangle|^2}{||E_{\text{in}}||^2 ||E_{\text{desired}}||^2}. \tag{2.10}$$

Hence the SRE is limited to any real value between zero and unity where unity can only be reached if all the energy of the input field ends up in exactly the desired field, i.e.

$$\frac{E_{\text{out}}}{||E_{\text{in}}||^2} = \frac{E_{\text{desired}}}{||E_{\text{desired}}||^2}. \tag{2.11}$$

This definition is not to be confused with the definition for the efficiency, for efficiency itself is defined as the amount of energy that ends up in the target area over the amount one started with:

$$\eta = \frac{||\alpha E_{\text{desired}} + E_{\text{error}}||^2}{||E_{\text{in}}||^2} = \frac{||\alpha E_{\text{desired}}||^2 + ||E_{\text{error}}||^2}{||E_{\text{in}}||^2}. \tag{2.12}$$

The difference between SRE and the standard definition of efficiency shows in two different ways. Firstly efficiency deals with signal intensities only (amplitudes) whereas SRE uses the complex signal (amplitude and phase) for its computation. Therefore an output with the desired amplitude but with a 90° phase difference with respect to the desired field produces a zero SRE while its (normal) efficiency would be unity. The second difference is that the SRE weights the output in accordance to the complex desired output function whereas efficiency directly measures the amount of energy in target region regardless of how much error occurs. By these definitions SRE will always be lower then the total efficiency when any error is present and can only equal efficiency if no error is present in either amplitude or phase.

Ideally the system maximizes the amount of energy in the desired signal, but the system is limited in how good it can do this. Calculating this upper bound for the Signal Relevant Efficiency (SRE) will provide two things. Firstly it can provide a measure of how good a design can be, making it useful as a crude benchmark tool. More importantly it will give the projection method that will be used in the design of thin diffractive element and a mathematical justification of when this projection method should be used.

2.4 UPPER BOUND SRE FOR ELEMENT DESIGN

Suppose an optical system in which an element has to be designed or optimized. This element is tasked to alter the field in the signal window W at the output plane to be as close to E_{desired} as possible. In practice the element can only make a finite set of changes to the incoming field for which all allowed changes to the field are denoted as A_c. For example A_c can present a phase-change only as would be the case for transmitting phase gratings and reflection gratings.

Suppose a known input field E_{in} is located directly before the to be designed element, the element can alter the input field in accordance to some linear bijective operator $\mathbf{t}$ where $\mathbf{t} \in A_c$. Bijective refers to that each input coordinate only affects a single output coordinate and vice versa, and the field directly after the element is therefore given by a point-wise multiplication between the operator and the input field: $\mathbf{t}E_{\text{in}}$. When this field is propagated through the system that is characterized by a known linear operator $\mathbf{L}$ the output field is given by

$$E_{\text{out}} = \mathbf{L}\left\{\mathbf{t}E_{\text{in}}\right\}. \tag{2.13}$$

The goal is to find out how closely the output field will resemble both amplitude and phase of E_{desired} given that the element can only alter the incoming field in accordance to $\mathbf{t} \in A_c$. If only the amplitude is defined, then the phase function of E_{desired} that results in the upper bound should also be determined. For small functions systematic search is used, for the design of complex DOE elements via IFTA as described in section 3.3 this is an integral part of the design algorithm.

Using the criteria of Signal Relevant Efficiency (SRE) to determine this, the upper bound for the SRE is given by

$$\eta_{\text{SRE}}^{\max} = \frac{\left|\left\langle E_{\text{opt}} | E_{\text{desired}} \right\rangle\right|^2}{||E_{\text{in}}||^2 \, ||E_{\text{desired}}||^2} = \frac{\left|\left\langle \mathbf{L}\left\{\mathbf{t}_{\text{opt}}(E_{\text{in}})\right\} | E_{\text{desired}} \right\rangle\right|^2}{||E_{\text{in}}||^2 \, ||E_{\text{desired}}||^2}, \tag{2.14}$$

where E_{opt} is the output field from optical element with linear operator $\mathbf{t}_{\text{opt}}$ that would result in the highest possible SRE. A visualization of this output field and

its computation (projection) is shown in Figure 2.2. The largest SRE comes from the

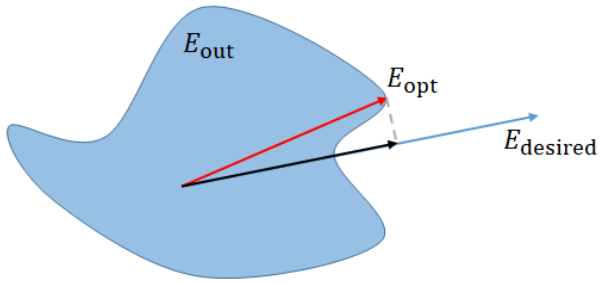

Figure 2.2: A cross section of Hilbert space that contains the fields at the output plane represented as vectors. The blob visualizes all possible output fields under element constrain A_c. The optimal field E_{opt} is the output that results in the largest projection onto the desired field E_{desired} and would result in the highest SRE.

possible output that gives the largest projection onto E_{desired} which also holds under the limit

$$\lim_{r\to\infty} rE_{\text{desired}}. \tag{2.15}$$

To this purpose maximizing η_{SRE} is the same as minimizing $1-\eta_{\text{SRE}}$ as $0 \leq \eta_{\text{SRE}} \leq 1$. In other words, finding the projection that lies closest to the desired output by extension lies closest under the limit of Eq. (2.15). In this limit the distance from the projection to E_{desired} is the same as the distance from E_{opt} to E_{desired} allowing one to ignore the projection operation altogether and use E_{opt} directly to find the field that results in the SRE upper bound;

$$E_{\text{opt}} = \underset{E_{\text{out}}\in A_c}{\text{argmin}} \lim_{r\to\infty} ||E_{\text{out}} - rE_{\text{desired}}||^2. \tag{2.16}$$

A visualization of this equivalence is shown in Figure 2.3. Now let $t_{\text{opt}} \in A_c$ denotes

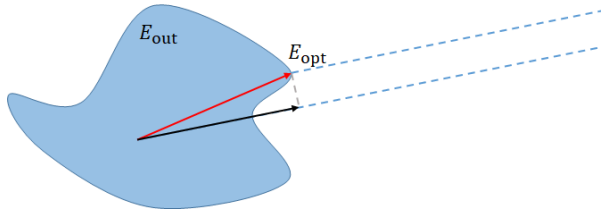

Figure 2.3: The projection of E_{opt} does not depend on the size of the norm of E_{desired} and in the limit of Eq. (2.15) the distance between E_{opt} and Eq. (2.15) becomes the same as the distance between the projection and Eq. (2.15).

the function of the to be designed element that results into output E_{opt}. Then t_{opt} is defined by

$$\mathbf{t}_{\text{opt}} = \underset{t\in A_c}{\text{argmax}} \frac{\langle \mathbf{L}\{\mathbf{t}E_{\text{in}}\} | E_{\text{desired}}\rangle}{||E_{\text{in}}||^2 ||E_{\text{desired}}||^2}. \tag{2.17}$$

As mentioned this is completely equivalent to minimizing the distance

$$\mathbf{t}_{\text{opt}} = \underset{t \in A_c}{\operatorname{argmin}} \lim_{r \to \infty} \left|\left| \mathbf{L}\left\{\mathbf{t} E_{\text{in}}\right\} - r E_{\text{desired}} \right|\right|^2 . \tag{2.18}$$

The evaluation of this equation is problematic still as it requires looking through all possible $t \in A_c$ to ensure that the global minimum is found. By making use of the fact that the smallest norm remains the smallest after applying a linear operator the optimal element function can also be found by

$$\mathbf{t}_{\text{opt}} = \underset{t \in A_c}{\operatorname{argmin}} \lim_{r \to \infty} \left|\left| \mathbf{t} - r \frac{\mathbf{L}^{-1}\left\{E_{\text{desired}}\right\}}{E_{\text{in}}} \right|\right|^2 , \tag{2.19}$$

or more briefly

$$\mathbf{t}_{\text{opt}} = \underset{t \in A_c}{\operatorname{argmin}} \lim_{r \to \infty} \left|\left| \mathbf{t} - r t_{\text{ideal}} \right|\right|^2 , \tag{2.20}$$

$$t_{\text{ideal}} = \frac{\mathbf{L}^{-1}\left\{E_{\text{desired}}\right\}}{E_{\text{in}}} . \tag{2.21}$$

The evaluation of this equation comes down to projecting onto the allowed values A_c which can be done point-wise as the operator $\mathbf{t}$ is bijective. The SRE upper bound is found by inserting the resulting t_{opt} into Eq. (2.14).

For the evaluation of the SRE upper bound it should be noted that an arbitrary constant phase factor $\phi_c \in [0, 2\pi)$ can be assigned to the desired output field $e^{i\phi_c} E_{\text{out}}$ without changing the field in any physical way. The choice of this phase factor will matter if neither the constraint A_c nor the to be projected transmission function t_{ideal} creates a rotationally symmetric pattern in the complex plane. If neither are symmetric one must evaluate the SRE for all ϕ_c so that the largest found SRE will represent the SRE upper bound.

3 Scalar Theory of Diffraction

In the scalar theory of diffraction of light the coupling between the electric and magnetic field components is neglected so that each component of the vectorial field can be dealt with independently. Using this assumption for diffractive structures requires that the smallest features in the diffracting structure are large compared to the incident wavelength and that the field of interest lies in the far field of the diffractive structure [5].

Diffractive elements that typically satisfy these conditions range from beam splitters, beam homogenizers, holograms and diffractive lenses. To design such elements various approaches have been developed. Some rely on rapid iteration, e.g. Iterative Fourier Transform Algorithms (IFTA) such as the Gerchberg-Saxton algorithm [6], the steepest decent methods [7,8] or methods based on evolutionary algorithms [9]. There are also approaches that compute the design in a single step [10,11].

From these methods IFTA has become a standard tool in industry to design diffractive optical elements [12]. This method assumes that the element lies in the paraxial domain and can be modeled by a complex amplitude transmission function that adheres to the thin-element approximation. It is this design method that is modified and shown later on in this chapter.

In this thesis the design of efficient optics in the Deep Ultra Violet (DUV), Extreme Ultra Violet (EUV) and X-ray regime are of interest. In these optical regions thin or reflective optical elements can become a necessity as the typical dielectric materials start to absorb light. In optical microlithography for instance, a (transmitting) Diffractive Optical Element (DOE) can be used to homogenize excimer lasers. Being thin makes the DOE greatly increases its survival when facing high incidence power [13]. The element needs not to homogenize the instantaneous field that fluctuates in both time and space but only time integrated beam intensity.

In this chapter the thin (diffractive) element approximation along with the effect of absorption on transmission is described first. This is followed by an overview of the design algorithm when it is combined with the SRE theorem to create an efficient design algorithm for (thin) transmission gratings made of absorbing materials.

3.1 THIN ELEMENT APPROXIMATION AND ABSORPTION

The use of rigorous Maxwell solvers to describe a grating, e.g. Fourier Modal Method (FMM) [14–17], finite difference [18], finite element [19], differential [20] or integral methods [21] can be computationally expensive. The required effort can become (prohibitively) expensive when a two dimensional grating with a grating period much larger than the wavelength is considered. In the geometrical optics limit these gratings can be approximately modeled with Thin Element Approximation (TEA). If this approximate description of the problem is sufficiently accurate, one can use significantly speed up iterative based design methods.

The thin element approximation makes the assumption that no energy is laterally displaced when the field is propagated through the element. Such an assumption requires that the incoming field has at most small oblique incidence ($\theta \lesssim 20^\circ$) and thin

enough to have lateral propagation in the element to be negligible. It also requires that the minimum feature size of the element is large with respect to wavelength ($\gtrsim 10\lambda$) and no non-linear effects occur in the element.

Under these conditions the lateral propagation in the element can be neglected and a scalar description for the field can be used. With this the response of the element can be modeled by a fixed bijective transmittance function $t(x, y)$. Assuming that the thin element does not affect the polarization of light, the scalar field component E_t after the element is given by

$$E_\mathrm{t}(x, y) = t(x, y)E_\mathrm{in}(x, y), \tag{3.1}$$

where $E_\mathrm{in}(x, y)$ denotes the field directly before the element. Taking that the thin material is made of a homogenous lossy material with refractive index

$$\hat{n} = 1 + \Delta n + i\kappa, \tag{3.2}$$

and has a surface profile profile $0 \leq h(x, y) \leq H$, then the refractive index profile of the thin element can be written as

$$\hat{n}(x, y, z) = \begin{cases} \hat{n} & \text{if } 0 \leq z \leq h(x, y) \\ 1 & \text{if } h(x, y) < z \leq H \end{cases}, \tag{3.3}$$

with the refractive index of the environment, be it air or vacuum, approximated to be one.

For such an element the transmittance operator becomes

$$t(x, y) = \exp\left[i\frac{2\pi}{\lambda} \int_0^H \hat{n}(x, y, z)dz \right] \tag{3.4}$$

which itself can be split into a phase and amplitude modulation part:

$$t(x, y) = |t(x, y)|\exp[i\phi(x, y)]. \tag{3.5}$$

The phase modulation is given by:

$$\phi(x, y) = (2\pi/\lambda)\Delta n h(x, y), \tag{3.6}$$

and amplitude modulation by:

$$|t(x, y)| = \exp[-(2\pi/\lambda)\kappa h(x, y)]. \tag{3.7}$$

Merging Eqs. (3.6) and (3.7) gives the values to which the transmittance function is limited to, denoted by A_c, and is written as

$$A_c(\phi) = \exp[-(\kappa/\Delta n)\phi], \quad \text{with} \quad \phi \geq 0. \tag{3.8}$$

Figure 3.1 illustrates this constraint for various values of $\kappa/\Delta n$ on the complex plane. If $\kappa = 0$ there is no absorption and therefore no amplitude modulation. In this case the element only alters the phase of the incoming field and this constraint is represented by the transmittance function only being allowed to choose the values that lie on unit circle in Figure 3.1. If absorption is present, $(\kappa > 0)$, Eq. (3.8) results in an inward spiral on which any value of $t(x, y)$ must lie for any given point (x, y).

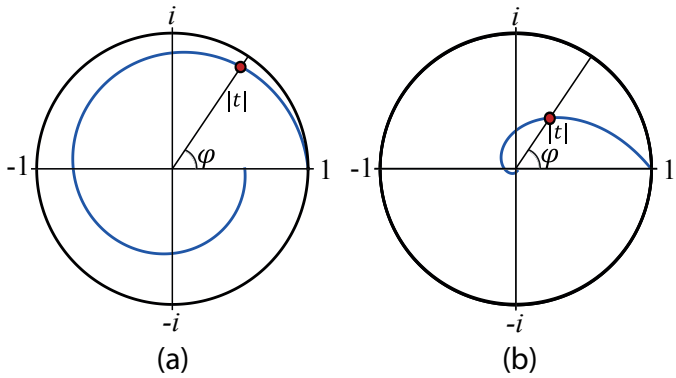

Figure 3.1: Representation of the possible values the transmission function can take for elements with complex refractive index $n = 1 + \Delta n + i\kappa$. The unit circle would represent the phase-amplitude values if no absorption is present ($\kappa = 0$). The blue lines depict for (a) κ/Δ n = 0.1 and (b) $\kappa/\Delta n = 0.8$ the possible transmission values on the spirals.

3.2 DIFFRACTION GRATING

If the thin element is a regular periodic structure it is referred to as a diffraction grating and can be represented by a Fourier series

$$t(x,y) = \sum_{(m,n)=-\infty}^{\infty} T_{\text{out}}(m,n)\exp\left[i2\pi(mx+ny)\right]dxdy, \tag{3.9}$$

where

$$T_{\text{out}}(m,n) = \int_0^1\!\!\int t(x,y)\exp\left[-i2\pi(mx+ny)\right]dxdy. \tag{3.10}$$

For ease of notation the periods are normalized to unity (without loss of generality) in both x and y direction. The Fourier transform itself is a linear operator and for brevity denoted as $T = \mathbf{F}\{t\}$ and inversely $t = \mathbf{F}^{-1}\{T\}$.

The coefficients $T_{\text{out}}(m,n)$ represent the complex amplitudes of the diffraction orders (m,n) and the efficiencies of these orders are given by

$$\eta_{(m,n)} = \frac{|T_{\text{out}}(m,n)|^2}{||E_{\text{in}}||^2}. \tag{3.11}$$

A basic property of the Fourier transform to be used later on is that displacement of the input by a given distance $t(x-x', y-y')$ does not change the amplitude of the diffraction orders, only introduce a linear phase shift: $T_{\text{out}}(m,n)\exp[i2\pi(mx'+ny')]$ is introduced.

3.2.1 SNR

To quantify how well a grating or grating design performs two measures are introduced, the gratings efficiency (η) and the Signal to Noise Ratio (SNR).

The gratings efficiency expresses how much of the incoming fields energy reaches the target window, i.e.

$$\eta = \sum_{(m,n)\in W} \eta_{(m,n)}, \tag{3.12}$$

where η is bound to lie in $0 \leq \eta \leq 1$.

On the other hand the Signal to Noise Ratio expresses the ratio between the amount of desired field and deviation from this in the signal window. If the output field is decomposed as in Eq. (2.6), then the SNR is given by

$$SNR = \frac{||\alpha T_{\text{desired}}||}{||T_{\text{err}}||}, \tag{3.13}$$

with T_{err} denoting the deviation from the desired amplitude distribution inside the target window area:

$$T_{\text{err}}(m,n) = T_{\text{out}}(m,n) - \alpha T_{\text{desired}}(m,n), \quad \text{with} \quad (m,n) \in W. \tag{3.14}$$

A good design attains a high efficiency with minimal noise. For the design process of diffractive elements in the paraxial domain these two competing criteria are satisfied by employing an Iterative Fourier Transform Algorithm (IFTA).

3.3 ITERATIVE FOURIER TRANSFORM ALGORITHM (IFTA)

For a given output T_{desired} the ideal grating's transmittance function is a complex function of the form

$$t_{\text{ideal}}(x,y) = \frac{\mathbf{L}^{-1}\left\{T_{\text{desired}}\right\}(x,y)}{E_{\text{in}}(x,y)}. \tag{3.15}$$

Such a transmittance function is rarely realizable as it does not adhere to the material and/or fabrication constraints A_c that are imposed. To this end an iterative method is applied where in quick iterative succession the constraint A_c is applied to the transmittance function and the desired output profile T_{desired}. The way how these constraints are applied can strongly affect the algorithm's performance.

3.3.1 Projection onto A_c

The constraint A_c that must be applied iteratively can be enforced in different ways. As argued it is expected that the best profile lies close to the profile that maximizes SRE and as such the projection should be done such that it maximizes SRE.

If the constraint is of the form of Eq. (3.8) then the projection onto A_c that maximizes the SRE is according to Eq. (2.21) to project the transmittance function from infinity onto the constraint A_c along the shortest path possible. As shown in Appendix A the most direct projection path results in

$$\phi_{\text{proj}} = \begin{cases} \theta - \arctan(\kappa/\Delta n) & \text{if } 0 \leq \theta - \arctan(\kappa/\Delta n) \leq \theta_{\text{M}} \\ 0 & \text{otherwise} \end{cases}, \tag{3.16}$$

where θ is the phase of the transmittance function before projection and the constant θ_{M} is determined numerically by solving

$$\sqrt{1+(\kappa/\Delta n)^2}\cos\left[\theta_{\text{M}} + \arctan(\kappa/\Delta n)\right]\exp\left(\theta_{\text{M}}\kappa/\Delta n\right) = 1. \tag{3.17}$$

Figure 3.2 shows that the direct projection method starts to deviate significantly from radial projection if the material becomes lossy ($\kappa/\Delta n > 0$).

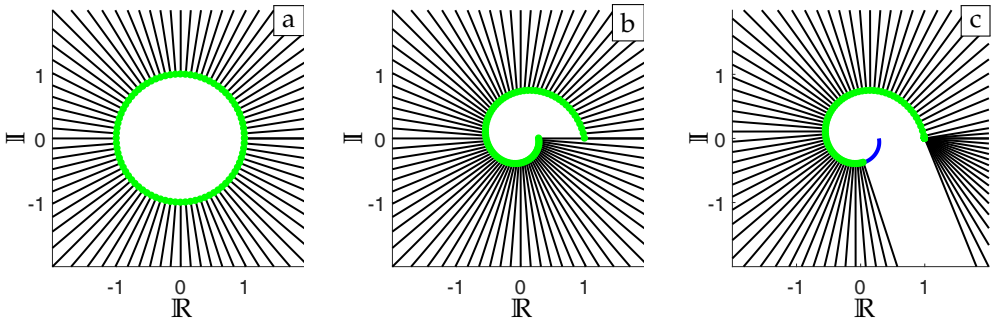

Figure 3.2: Two constraints for A_c shown in the complex plane along with two projection methods. a) Radial projection and direct projection are identical if no absorption is present. b) Radial projection when $\kappa/\Delta n = 0.2$, c) direct projection that maximizes SRE for $\kappa/\Delta n = 0.2$.

3.3.2 Applying output constraint

The iterative method for designing lossy elements is split up into two steps: the first step maximizes the SRE while the second step improves the Signal to Noise Ratio (SNR) of the design at the cost of efficiency. The assumption implicit here is that the design with maximum SRE lies relatively close to the design that achieves both high efficiency and good uniformity.

The concept of first maximizing the SRE has a historical precedent when using transparent materials with $A_c = \{|t(x,y)| = 1, \ \forall(x,y)\}$. It was argued that first any phase freedom should be used before sacrificing efficiency in favor of uniformity [12]. The only difference between the two steps is how the constraint at the output plane is applied. In the first step only the phase of the output is allowed to change while in the second step diffraction orders outside the signal window are allowed to appear in order to order to improve the Signal to Noise Ratio.

3.3.3 Step 1: SRE maximization

Every iterative method requires a starting point and here it is chosen to be

$$t_0(x,y) = \mathcal{F}\left\{|T_{\text{desired}}(m,n)|e^{i\phi_r(m,n)}\right\}, \tag{3.18}$$

where ϕ_r is a random phase distribution. The advantage of this starting point is that the profile already achieves the desired distribution and the random phase allows the algorithm to converge to different solutions (local minima) in the optimization landscape. This allows one to run the algorithm multiple times to see if a better design at different (local) minima can be found.

The next up is maximizing Signal Relevant Efficiency, which is done by first applying the phase-amplitude constraint by projecting onto A_c using Eq. (3.16):

$$t'(x,y) = \exp\left[i\text{atan}(\kappa/\Delta n)\right]\exp\left[(i-\kappa/\Delta n)\phi_{\text{proj}}(x,y)\right]. \tag{3.19}$$

The extra phase factor of $\text{atan}(\kappa/\Delta n)$ is applied in each iteration step to ensure that when that iteration converges to the global phase that maximizes the SRE it stays fixed at that global phase over the course of the iteration process. Hereafter the propagation operator is applied to compute the output field $T_{\text{out}} = \mathcal{F}\{E_{\text{in}}t'\}$, this is

in turn updated as

$$T'(m,n) = \begin{cases} T_{\text{desired}}(m,n)\exp\left(i\arg\{T(m,n)\}\right) & \text{when } (m,n) \in W \\ 0 & \text{otherwise} \end{cases}, \tag{3.20}$$

where $\arg\{T(m,n)\}$ are the phase values of $T(m,n)$ at the previous iteration step.

Figure 3.3 visualizes a single iteration step early during SRE maximization. The

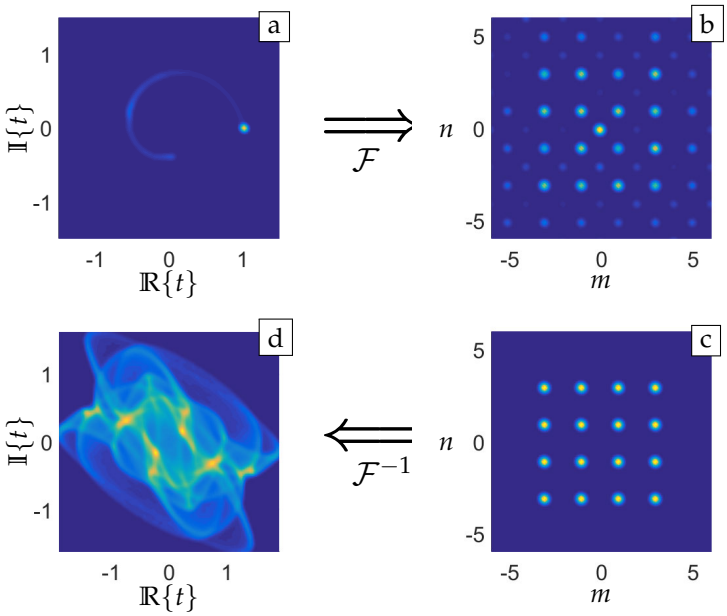

Figure 3.3: This figure displays the results during a single iteration of the SRE optimization algorithm. a) The real and imaginary part of the profile that obeys the constraint A_c , obtained by projecting the profile onto the constraints. b) The resulting diffraction orders amplitudes of the profile that obeys A_c. c) All amplitudes are replaced with the desired amplitudes but phase is kept. d) The profile shown in the complex plane would produce the desired diffraction orders with 100% efficiency.

iteration between these two constraints of Eq. (3.19) and Eq. (3.21) stops when the transmission profile and its output no longer change or if more then a 100 iterations have been performed.

3.3.4 Step 2: Signal to Noise Ratio maximization

The profile that maximizes the SRE upper bound is assumed to lie close to the best design and is therefore used as a starting point for this section of optimization. If the design only maximizes the SRE, it will typical have high efficiency but very poor Signal to Noise ratio. In order to improve uniformity efficiency is sacrificed by allowing some amplitudes outside of the signal window W to persist. To this end the constraint at the output field is altered to allow this:

$$T'(m,n) = \begin{cases} A|T_{\text{desired}}|\exp\left(i\arg\{T(m,n)\}\right) & \text{if } (m,n) \in W \\ T(m,n) & \text{otherwise} \end{cases}, \tag{3.21}$$

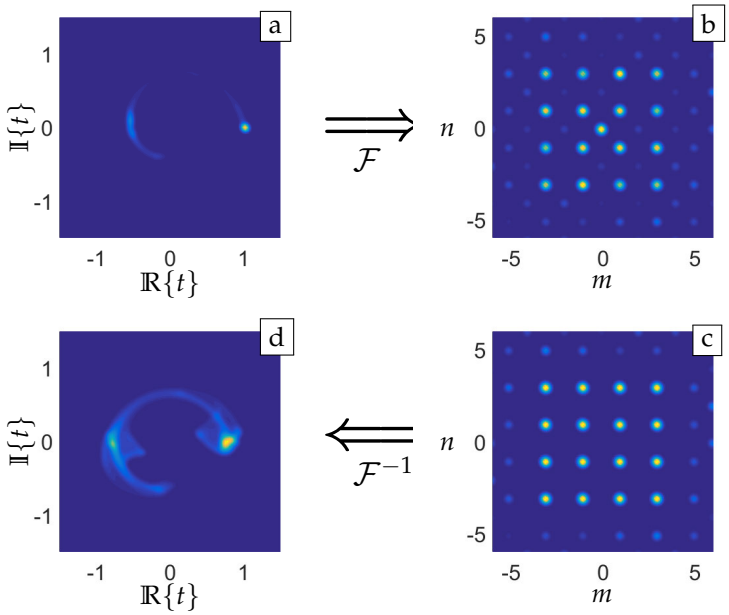

Figure 3.4: Same as Figure 3.3 when using the algorithm to maximize the Signal to Noise Ratio. a) The real and imaginary part of the profile that obeys the constraint A_c , obtained by projecting the profile onto the constraints. b) The resulting diffraction orders amplitudes of the profile that obeys A_c. c) Constraint changed to replace the amplitudes inside the signal window with the desired ones while keeping the rest unchanged. d) The profile required to produce the updated output shown in c.

with the constant A given by

$$A = \frac{\langle |T| | |T_{\text{desired}}| \rangle}{||T_{\text{desired}}||^2}. \tag{3.22}$$

With replacing the constraint the iterative algorithm is run for another 100 iterations or until the design and output no longer change. The second iteration cycle is depicted in Figure 3.4.

The next chapter will compare the performance of the algorithm when maximizing SRE if projecting onto the constraint A_c versus keeping the same angle when projecting on the constraints.

4 DOE Design with SRE

In this section the results for the IFTA algorithm are discussed, section 4.1 goes into detail about how the SRE-upper bound theorem directly gives the ideal design when only a single or two diffraction orders are of interest. In section 4.2 the algorithm's performance is compared against a known non-trivial solution, giving an idea of its effectiveness. The designs created by the algorithm are also compared to a more direct implementation. The last section 4.3 explains the objective and design for a V-groove grating, a broadband reflection grating.

4.1 1 & 2 DIFFRACTION ORDERS

The SRE upper bound theorem can be used to obtain the profile that exactly produces the desired output with the highest possible efficiency. This only works for any design problems where the SRE upper bound matches the efficiency of the profile itself. The SRE upper bound determines the maximum amount of energy that ends up in the desired signal while efficiency tells us the amount of energy in the target window. If these two are equal the desired signal is obtained without any errors in the target window while the SRE upper bound tells us the design can not get any better. For (paraxial) grating design this condition can be met for gratings where a single order or two diffraction orders are of interest.

4.1.1 One diffraction order

For an output field consisting of a single diffraction order the condition stated above is met automatically, as the Signal to Noise Ratio has no meaning for a single point, so the desired signal is always obtained without error. Hence SRE will equal efficiency. Now let us assume a plane wave input field and have the desired output field consisting of a single diffraction order located at $(\bar{m}, \bar{n})$:

$$T_{\text{desired}} = \delta_{m-\bar{m},n-\bar{n}}, \tag{4.1}$$

where δ is used to indicate the Kronecker delta symbol. To compute the SRE upper bound of this function it needs to be projected onto the constraints. The linear operator needed to go from the plane after the grating to the output plane is a Fourier transform $\mathbf{F}$. Therefore the ideal transmission function is given by

$$\begin{aligned} t_{\text{ideal}} &= \mathbf{F}^{-1}\left\{\delta_{m-\bar{m},n-\bar{n}}\right\} \\ &= \exp[-2\pi i(\bar{m}x + \bar{n}y)]. \end{aligned} \tag{4.2}$$

From here the profile that yields the SRE upper bound is defined by Eq. (2.21) as

$$\mathbf{t}_{\text{opt}} = \underset{t\in A_c}{\operatorname{argmin}} \lim_{r\to\infty} \left|\left| t - re^{-2\pi(\bar{m}x+\bar{n}y)} \right|\right|^2, \tag{4.3}$$

where the constraints A_c has yet to be defined. Let us suppose the transmission function is limited to $A_c = \exp[-(\kappa/\Delta n)\phi]$, $\phi \in [0, 2\pi)$ with $\kappa/\Delta n = 0.2$.

The first step is to note that the choice of global phase will not affect the projection as t_{ideal} is rotationally symmetric on $\mathcal{C}$ and for this reason will not influence the result of the projection of t_{ideal} onto A_c. As derived in Appendix A, the phase value where these projected points end up is given by

$$\phi_{\text{proj}} = \begin{cases} \theta - \arctan(\kappa/\Delta n) & \text{if } 0 \leq \theta - \arctan(\kappa/\Delta n) \leq \theta_{\text{M}}, \\ 0 & \text{otherwise,} \end{cases} \tag{4.4}$$

where the constrain θ_{M} is determined numerically by solving

$$\sqrt{1 + (\kappa/\Delta n)^2}\cos\left[\theta_{\text{M}} + \arctan(\kappa/\Delta n)\right]\exp\left(\theta_{\text{M}}\kappa/\Delta n\right) = 1. \tag{4.5}$$

Figure 4.1 shows how the projection is done point by point for projecting $t_{\text{ideal}}(x, y)$ on A_c. Suppose the transmittance values $t_{\text{ideal}} = \{1, i, -1, -i\}$ needs to be projected upon A_c, the projection takes the shortest path from $\lim_{r\to\infty} r\{1, i, -1, -i\}$ to A_c as illustrated in Figure 4.1(a). The projections to the other points are illustrated in Figure 4.1(b) with the resulting phase profile shown in Figure 4.1(c).

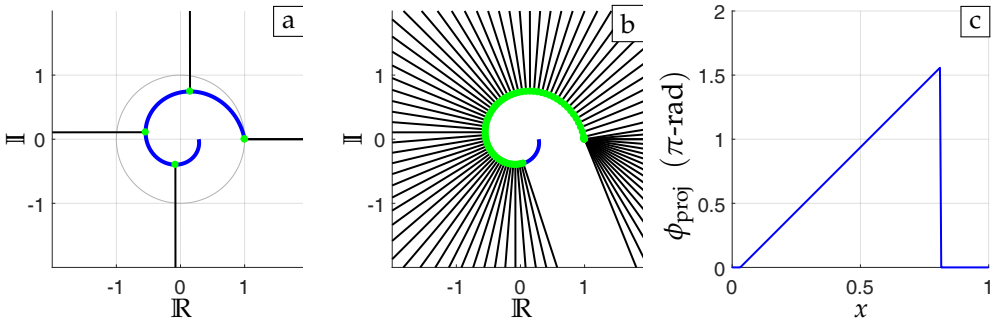

Figure 4.1: Projection onto A_c when $\kappa/\Delta n = 0.2$ where a) projecting the four values $\lim_{r\to\infty} r\{1, i, -1, -i\}$ onto A_c. b) Projection to all values and c) the resulting phase profile.

Note that in Figure 4.1(b) the two lines that run along the side of the 'gap' are mostly parallel as they originate from adjacent points at infinity but have different values of A_c that lie closest to them.

When the constraints are changed to be phase only $A_c = \exp(i\phi)$ with $\phi \in [0, 2\pi)$, quantized phase with $A_c = [1, i, -1, -i]$, or an amplitude only grating $A_c = [0, \ldots, 1]$ then the projection and resulting profile can be seen in Figure 4.2. From Figure 4.2(c) in specific one can easily answer the following question. Why is that from all possible gray scale gratings the highest efficiency grating has a binary-amplitude profile with a 50% duty cycle? The projection in this figure shows that picking any other value on the transmittance function lies further away from the to be projected values at infinity and thus would result in a smaller projection and hence a lower SRE.

Figure 4.2(b) shows the ideal grating when the phase levels are quantized. The expected efficiency of the resulting diffractive element can be approximated as [22]

$$\eta_{\text{quant}} \approx \text{sinc}(1/Z)^2 \times \eta, \tag{4.6}$$

where η is the efficiency of the grating before quantization. If this expected efficiency is compared to the efficiency of gratings obtained by SRE upper bound theory for blazed gratings with $\eta = 1$, then they are identical as shown in Figure 4.3.

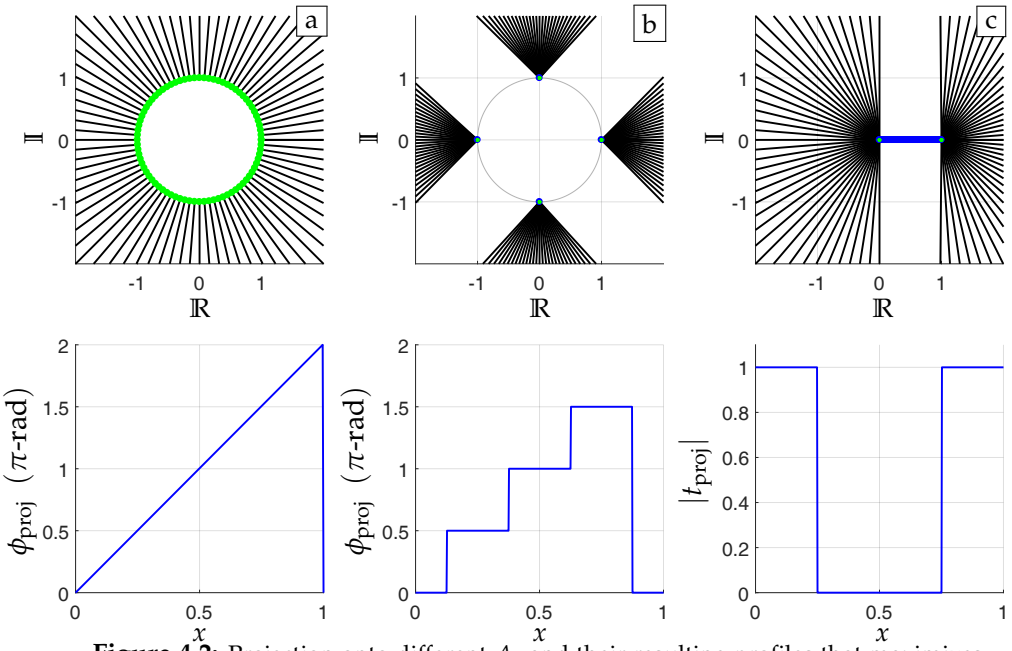

Figure 4.2: Projection onto different A_c and their resulting profiles that maximizes a single diffraction order. Top row shows the projection and bottom row the resulting phase or amplitude profiles.

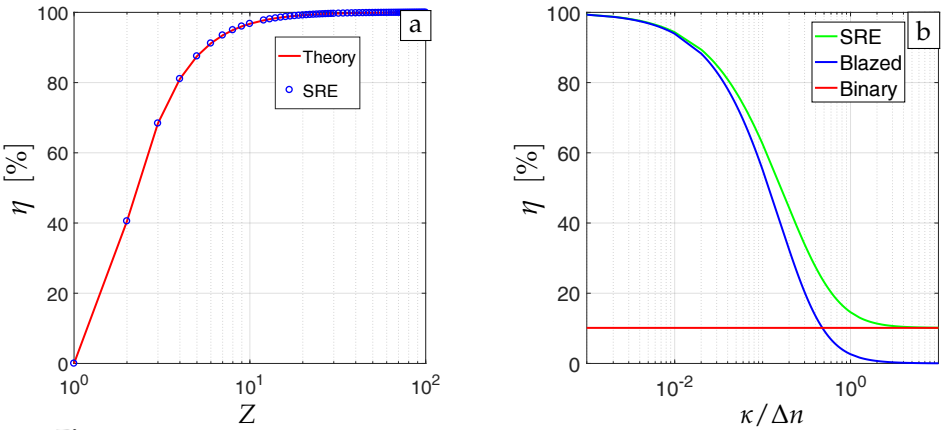

Figure 4.3: a) The phase-only grating efficiency for various quantized phase levels. The dots denote the resulting efficiency of the SRE theory and the line is the efficiency given by Eq. (4.6). b) The transmittance profile obtained via SRE theory compared with the efficiency of a blazed-phase and binary amplitude transmittance for various levels of absorption.

On the right side of this figure the single diffraction order efficiency for a blazed and binary grating are compared to the efficiency of the profile obtained by SRE theory for various levels of absorption. The efficiency of the blazed grating becomes inferior to the efficiency of 10.13% of the binary-amplitude grating with a fill-factor of 50% when $\kappa/\Delta n > 0.48$. The graph also gives a rough indication of when absorption should be taken into account in grating design. At $\kappa/\Delta n > 3.6 \cdot 10^{-3}$ the difference between a phase only design and the optimal design is more than 0.1% and grows to over 1% at $\kappa/\Delta n > 1.7 \cdot 10^{-2}$.

4.1.2 Two diffraction orders

For a signal consisting of two diffraction orders the desired output field is given by

$$T_{\text{desired}} = a_1\delta_{m-\bar{m}_1,n-\bar{n}_1} + a_2\delta_{m-\bar{m}_2,n-\bar{n}_2}, \tag{4.7}$$

with $|a_1|^2 + |a_2|^2 = 1$. The values $(\bar{m}_1, \bar{n}_1)$ and $(\bar{m}_2, \bar{n}_2)$ denote the different locations of the diffraction orders while $a_1 = |a_1|e^{i\phi_1}$ and $a_2 = |a_2|e^{i\phi_2}$ are complex valued constants.

For the design of the grating only the amplitudes of a_1 and a_2 are of interest, meaning that the phase should be chosen such that the efficiency is maximized. In actuality the choice of both phase factors are irrelevant in the same way it was for the single diffraction order design. When the phase of a_1 is shifted with respect to a_2 it will only result in a lateral displacement of the grating. Therefore freedom in lateral displacement and global phase imply that the design for a specific phase of ϕ_1 and ϕ_2 is the same as all others choices of phase for given amplitudes $|a_1|$ and $|a_2|$.

If for simplicity it is assumed that the input field is normalized as $||E_{\text{in}}||^2 = 1$, then it follows from Eq. (3.15) that the ideal transmission function becomes

$$t_{\text{ideal}} = e^{i\phi_1}\left(|a_1|e^{-2\pi i(\bar{m}_1 x + \bar{n}_1 y)} + |a_2|e^{-2\pi i(\bar{m}_2 x + \bar{n}_2 y + \Delta\phi)}\right), \tag{4.8}$$

with $\Delta\phi = \phi_2 - \phi_1$ chosen to be zero.

Unlike the single diffraction order signal, the two diffraction order signal has a defined SNR. Therefore it is no longer guaranteed that the profile that gives the SRE upper bound has no error, i.e. that it would guarantee the best possible design. In situations where the problem is totally symmetric, i.e. $(\bar{m}_1, \bar{n}_1) = (-\bar{m}_2, -\bar{n}_2)$ with $|a_1|/|a_2| = 1$, such an error does not occur. Symmetry implies that the output is of the form $T_{\text{out}}(m,n) = T_{\text{out}}(-m,-n)$. As a consequence, the transmission function is also invariant under 180 degree rotation $t(x,y) = t(-x,-y)$ because the Fourier transform maintains this relation. If t_{ideal} is symmetric, then its projection onto the symmetric constraints t_{opt} must be symmetric as well as the projection only alters the phase values and not their location on $t(x,y)$. If this t_{opt} is symmetric, then $|a_1|/|a_2| = 1$ and no error is present. For an output of the form of Eq. (4.7) the SRE upper bound is found by the profile

$$\mathbf{t}_{\text{opt}} = \underset{t\in A_c}{\operatorname{argmin}} \lim_{r\to\infty} \left|\left| t - re^{i\phi_c}\cos(2\pi(\bar{m}_1 x + \bar{n}_1 y))\right|\right|^2, \tag{4.9}$$

where the constraint A_c is for consistency taken to be $A_c = \exp[-\kappa/\Delta n\phi]$, $\phi \in [0, 2\pi)$.

Although t_{ideal} is invariant under a 180 degree rotation, it is not circularly symmetric, and thus global phase has to be taken into account when searching for the SRE upper bound. Projecting t_{ideal} onto A_c using Eq. (4.4) for various global phase values produces Figure 4.4(a) where the SRE is shown as a function of global phase. In here the SRE and efficiency are equal for all global phases meaning that all the profiles create the diffraction orders with the desired ratio, be it with a different efficiency. The highest SRE represents the SRE upper bound which in this case occurs at $\phi_c = 0$ or $\phi_c = \pi$. The resulting grating has an efficiency (SRE upper bound) of $\text{SRE}_{\text{UB}} = 0.487$ and is shown in Figure 4.4(c) for $(\bar{m}_1, \bar{n}_1) = (-3,-1)$ and $\kappa/\Delta n = 0.2$. As visualized in the projection only two angles that lie 180° apart will

determine the profile, each angle contains half the points regardless of the constraint or the locations of the two mirrored diffraction orders. The resulting optimum profile will therefore always be binary with a 50% duty cycle where the two phase levels are determined by the (SRE-upper bound) projection.

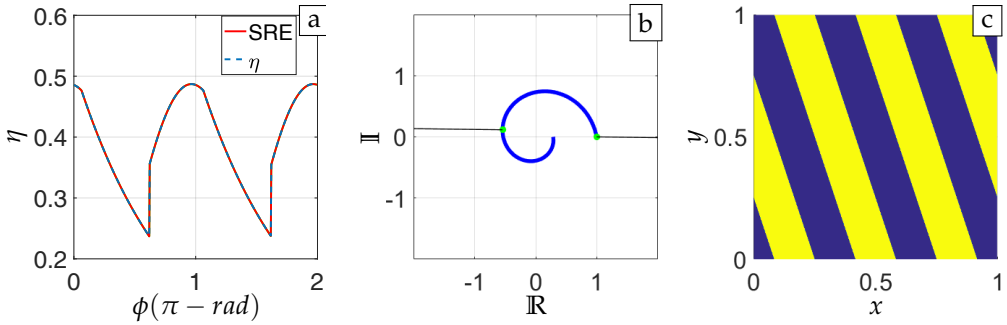

Figure 4.4: a) SRE for a two point signal with $|a_1| = |a_2|$ located at $(\bar{m}_1, \bar{n}_1) = (-3, -1)$ and $(\bar{m}_2, \bar{n}_2) = (3, 1)$ for $\kappa/\Delta n = 0.2$ as a function of global phase factor ϕ_c (b) The projection of the SRE maximizing profile onto A_c. (c) The profile that results in the maximum SRE.

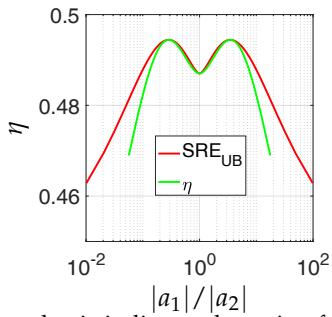

Figure 4.5: The horizontal axis indicates the ratio of the diffraction orders located at $(\bar{m}_1, \bar{n}_1) = -(\bar{m}_2, \bar{n}_2)$, the vertical axis denotes efficiency for the absorption constraint $\kappa/\Delta n = 0.2$. The red line shows the SRE upper bound as a function of the desired amplitude ratio while the green line denotes the efficiency of the profile that maximizes SRE re-scaled as a function of its amplitude ratio.

When the two desired diffraction orders are no longer equal or mirrored, the SRE upper bound no longer provides the desired profile without error as shown in Figure 4.5. In this figure the SRE upper bound shown in red is plotted as a function of the desired diffraction amplitude ratio while the efficiency shown in green is plotted as a function of the obtained profiles amplitude ratio, i.e. the obtained profile has a different amplitude ratio than desired. Note that the green line stops at $\eta_{\text{tot}} = 0.469$ at position $\eta_{(\bar{m}_1,\bar{n}_1)}/\eta_{(\bar{m}_2,\bar{n}_2)} = |a_1|^2/|a_2|^2 = 0.444/0.025$ where the obtained design results in exactly the same result/profile as when optimizing for a single diffraction order design located at $\eta_{\bar{m}_1,\bar{n}_1}$. This confides that no design exists that can have more energy located at $\eta_{\bar{m}_1,\bar{n}_1}$ as this is the SRE upper bound. Hence when looking at both diffraction orders there exists no profile that results in a higher efficiency for that amplitude ratio as that would entail the existence of a profile with more energy in $\eta_{\bar{m}_1,\bar{n}_1}$. Thus despite that the SRE upper bound and the found profile

efficiency do not match one can say that the found profile is the best possible profile in this specific case.

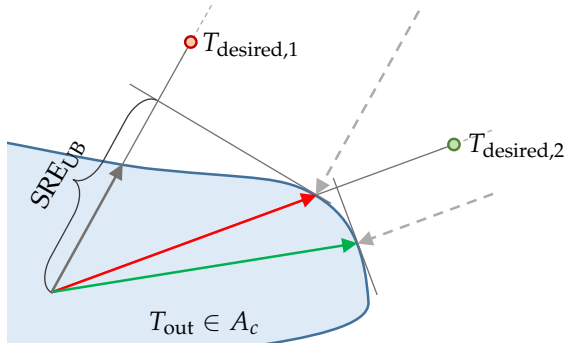

Figure 4.6: A visualization in a cross-section of Hilbert space showing how the upper bound for one design ($T_{\text{desired},1}$) can yield the highest efficiency design without error for another output ($T_{\text{desired},2}$). The accolade shows the SRE upper bound while the smaller black arrow indicates the highest efficiency possible when one does not accept any errors in the signal window W.

From the SRE upper bound point of view any profile resulting in the SRE upper bound for some output lies on the boundary of possible outcomes. To clarify this statement the possible outputs and a couple of desired outputs are depicted in a cross-section of Hilbert space in Figure 4.6. In this figure the red and green arrow indicate the designs that result in the SRE upper bound for the desired outputs $T_{\text{desired},1}$ and $T_{\text{desired},2}$ respectively. The lengths of the drawn arrows denote the amount of light that reaches the target window for that output and if an arrow does not point exactly towards T_{desired} then that output contains some errors in the target window. The red arrow therefore visualizes that no other design are possible under the constraints A_c that would result in a higher efficiency while not having any errors in the signal window when designing for $T_{\text{desired},2}$. The accolade in this figure indicates the maximum length any projection for $T_{\text{desire},1}$ can reach and the indicated length therefore represents the SRE upper bound.

From this analysis it is concluded that the found designs whose efficiencies are displayed in Figure 4.5 (in green) are the best possible designs for the found amplitude ratio if no error is allowed to exist in the signal window.

By extension this conclusion can be applied to any design regardless of symmetry or constraint A_c. For example if one would for instance want a solution for the non-symmetric problem where $\eta_{(m_1,n_1)}/\eta_{(m_2,n_2)} = 3$ with the diffraction orders located at $(m_1, n_1) = (1, 2)$ and $(m_2, n_2) = (0, -3)$ for $\kappa/\Delta n = 0.2$, then this method results in the phase-profile shown in Figure 4.7.

4.2 IFTA PERFORMANCE

To evaluate the performance of a design algorithm one could test its results against known design solutions for non-trivial cases. Such a nontrivial case occurs for a diffractive element that must result in three equal diffraction orders where $|T_{(-1,0)}| = |T_{(0,0)}| = |T_{(1,0)}|$, i.e. a triplicator design. Using the SRE upper bound to derive the optimal profile with three equal diffraction orders is difficult as now error can in principle occur in any of the three diffraction orders. Furthermore phase must be accounted for as it is included in the SRE definition: as only two phase values can

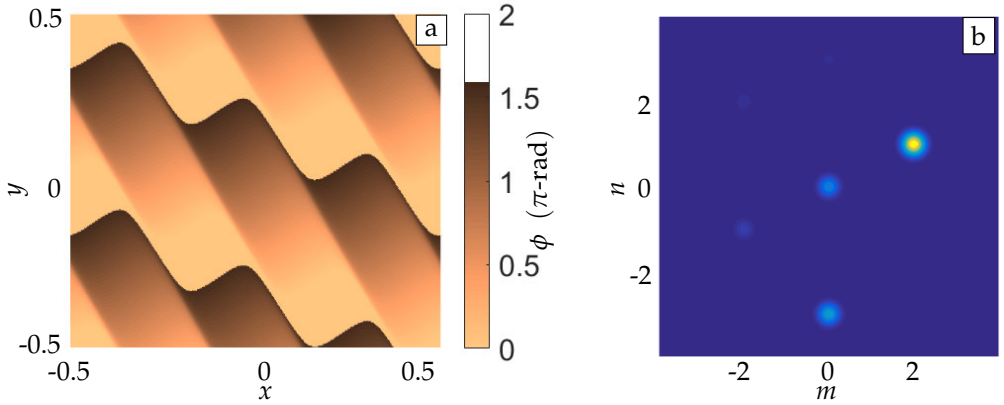

Figure 4.7: a) The phase profile of diffraction order profile for $\kappa/\Delta n = 0.2$ which the diffraction order output shown in b) located at $(m_1, n_1) = (1, 2)$ and $(m_2, n_2) = (0, -3)$ are to be maximized with $\eta_{(m_1,n_1)}/\eta_{(m_2,n_2)} = 3$. The resulting efficiencies of the diffraction orders are $\eta_{(1,2)} \approx 0.283$ and $\eta_{(0,-3)} \approx 0.094$.

be fixed by the global phase and spatial displacement redundancies, the choice for the third phase value will affect the SRE upper bound. For this reason the IFTA algorithm is employed to get around these problems.

4.2.1 Analytical design of a triplicator

The optimum transmittance function of a triplicator grating has been derived analytically for the purely dielectric case [23]. This derivation can be extended to include phase-dependent absorption as shown in Appendix B, giving a baseline to compare the performance of the IFTA algorithm against. As shown in the appendix the extended solution takes the form

$$\phi(x) = \begin{cases} 0 & \text{if } |x| < R \\ \varphi(x) + \phi_e & \text{if } R \leq |x| < 1/2, \end{cases} \tag{4.10}$$

where ϕ_c is the minimum of $\varphi(x), x \in [R, 1/2)$ and $\varphi(x)$ is the optimum solution of the equation

$$\begin{aligned} &(1-\alpha)[\cosh(\alpha\varphi) - a\cos(2\pi x)\sinh(\alpha\varphi)]\sin\varphi \\ &= (1+\alpha)[\sinh(\alpha\varphi) - a\cos(2\pi x)\cosh(\alpha\varphi)]\cos\varphi. \end{aligned} \tag{4.11}$$

The constant a is chosen such that $|T_{(-1,0)}| = |T_{(0,0)}| = |T_{(1,0)}|$ and the region in which the phase is zero, $R \in [0, 1/4]$, is chosen such that the efficiency is maximal.

It should be noted that this derived profile is only valid when $\kappa/\Delta n \lesssim 0.43$ for the derivation requires that $0 \leq \phi \leq \pi$, which is violated for $\kappa/\Delta n > 0.43$. A number of these optimal solutions to the triplicator design problem are depicted in Fig. 4.10(a) for various levels of absorption.

4.2.2 IFTA triplicator

Two different projection schemes are compared against the ideal triplication profile described by Eq. (4.10). The projection along radial lines is shown in Figure 4.8(a)

and referred to as radial projection. Whereas the direct projection method maximizes the SRE and is illustrated in Figure 4.8(b). It should be noted that when no absorption is present both methods are exactly the same as the most direct path is along the radial lines.

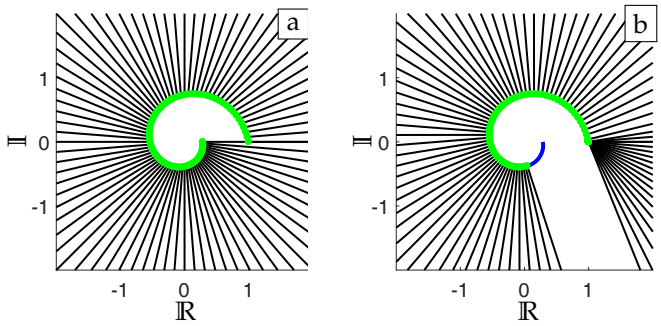

Figure 4.8: The phase dependent absorption constraint A_c shown for $\kappa/\Delta n = 0.2$ in the complex plane along with two projection methods. a) Radial projection, b) Direct projection.

The profiles that result from these two projection methods in the IFTA design process are compared to the found ideal result from Eq. (4.10) in Fig. 4.9. The data points represent the efficiencies of a triplicator design obtained from a single run, each time using a different random initial phase distribution as a starting point. The designs that did not result in three equal diffraction orders, i.e. an amplitude error of more then 10^{-5}% of the energy in the target window, were omitted from the graph in order to avoid making a poor comparison.

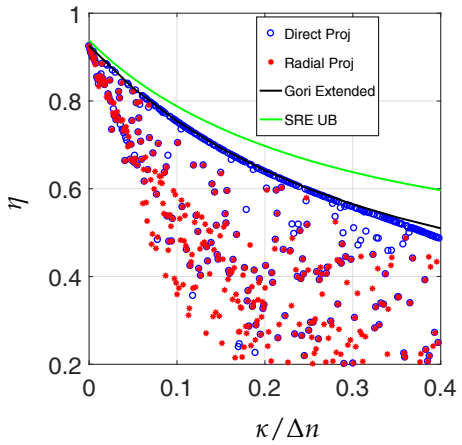

Figure 4.9: Comparing design efficiency between theoretical ideal profiles (shown in black), IFTA with direct projection (blue) and radial projection (red) for various levels of absorption. The SRE upper bound for various levels of absorption is also shown (green).

Figure 4.9 shows that the radial projection method leads to a large variation in performance and often does not come close to the theoretical ideal profile. As a

result the radial projection method would require a large number of runs in order to have a good chance, while not being guaranteed, to come close to the ideal result. Using the direct projection method of Eq. (3.16) yields a much better result on average, although it also gets stuck in local minima on occasion, resulting in a sub-optimal design.

As Figure 4.10(b) illustrates, the best performing profiles obtained with the IFTA algorithm for higher levels of absorption indeed violate the condition $0 \leq \phi \leq \pi$.

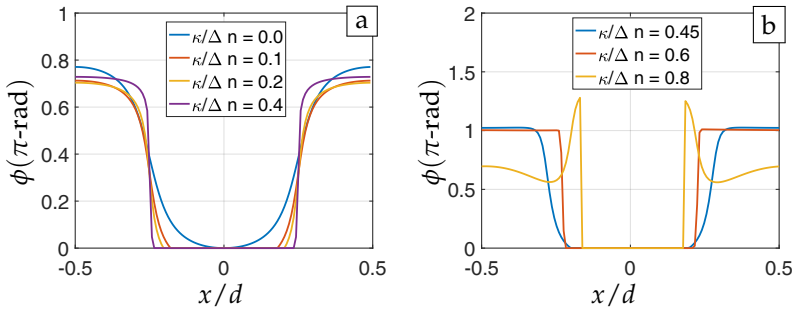

Figure 4.10: a) Theoretical ideal profiles given by Eq. (4.10) for various level of absorption. b) The (best performing) phase profiles found by IFTA for higher values of phase-dependent absorption.

4.2.3 On and off-axis design

In this section the performance of the IFTA algorithm for radial and direct projection are compared when designing either on or off-axis signals in general. An on-axis signal is defined to have the zeroth diffraction order be part of the desired signal, thus having it lie inside the signal window W. In the off-axis case the zeroth order lies outside of W.

On-axis design

For on-axis design the zeroth diffraction order will become an increasingly larger impediment when designing for greater values of $\kappa/\Delta n$. The strength of the zeroth diffraction order is determined by the averaged transmission function: $|T_0|^2 = |\iint t(x,y)dxdy|^2$ and can be roughly estimated by using a transmittance function that uses all phase values equally, such as the linear phase function $\phi(x) = 2\pi x, \;\; x \in [0,1)$:

$$|T_0|^2 = \frac{[1-\exp(-2\pi\kappa/\Delta n)]^2}{4\pi^2(1+\kappa^2/\Delta n^2)}. \tag{4.12}$$

Let f denote the amount of energy transmitted for such a transmittance function. For uniform use of phase values it is given by

$$f = \iint |t(x,y)|^2 dxdy = \frac{1-\exp(-4\pi\kappa/\Delta n)}{4\pi\kappa/\Delta n}, \tag{4.13}$$

so that when one considers an array illuminator consisting of N equal efficiency diffraction orders each can maximally attain an amplitude of f/N. Looking back at Eq. (4.12) this means that the zeroth order is expected to affect the design when the

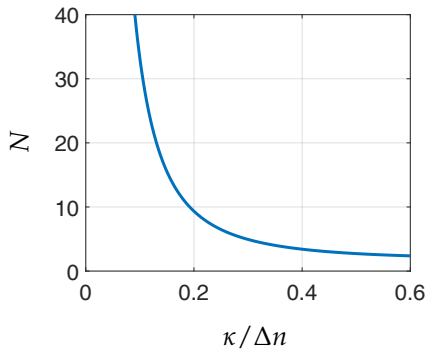

Figure 4.11: Any on-axis design with more than the indicated N diffraction orders expected to be (strongly) influenced by the zeroth order.

expected zeroth diffraction order amplitude is larger then the expected maximum attainable average diffraction order efficiency: $|T_0|^2 > f/N$. The relation $f/|T_0|^2$ is shown in Figure 4.11 as function of absorption and the desired number of equal diffraction orders. Any design that lies (far) above the shown curve is expected to (greatly) reduce the efficiency as the zeroth order will need to be actively suppressed. It should be noted that this is only a rough estimate as it was assumed that all phase values are used in equal amounts.

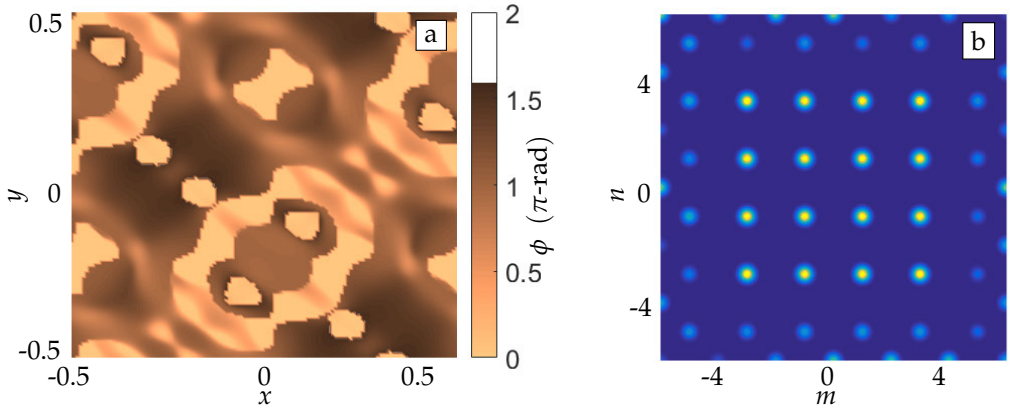

Figure 4.12: a) An example of a 4×4 fanout grating's phase profile by use of the IFTA algorithm with direct projection for $\kappa/\Delta n = 0.2$. b) The resulting diffraction pattern.

To see how absorption affects the design consider an on-axis fanout grating design with 4×4 equal diffraction orders for $\kappa/\Delta n = 0.2$. In the design the even numbered (m, n) diffraction orders and the zeroth order within the signal window are to be suppressed as illustrated in Figure 4.12(b). A single period of the corresponding phase profile is illustrated in Figure 4.12(a). It shows large areas where $\phi = 0$ and the profile lacks phase values $1.56\pi \lesssim \phi < 2\pi$, which is directly caused by using the SRE projection operator. The pixelation of the phase profile illustration is caused by the limited resolution of 128×128 discrete points used for the computation of this profile.

The probability distribution of the phase illustrated in Figure 4.13 shows the

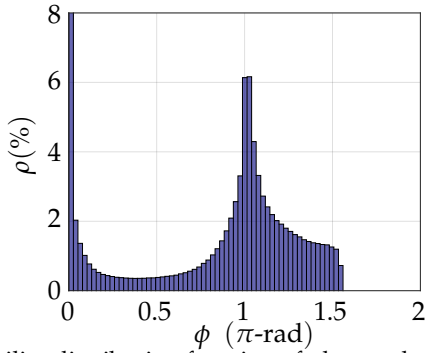

Figure 4.13: The probability distribution function of phase values of the design for a 4×4 on-axis fanout design at $\kappa/\Delta n = 0.2$. The y-axis has been clipped for clarity as the number of points with $\phi(x, y) = 0$ is $\sim 20\%$.

average phase distribution of a 1000 high efficiency designs. The zeroth order amplitude is most efficiently controlled by offsetting phase values around $\phi = 0$ with those around $\phi = \pi$ resulting in an almost binary design.

4.3 V-SHAPED GRATINGS

This section will focus on 1-D gratings consisting of a V-shaped groove or ridge micro structures. These structures are already common place in regular gratings and can be found in spectroscopy [24], reflection suppression [25] and beam splitting applications [26,27]. The advantage of V-shaped microstructures is that they can be accurately fabricated with silicon wet etching fabrication technology and can easily be replicated [28]. Such precision is useful when either the location or shape of the structure is modulated to encode a phase profile [29,31,32]. This encoding allows lens-like and diffractive elements to be encoded [12].

When the grating period is of the same order of magnitude as the wavelengths a rigorous electromagnetic grating theory would be required for computing the efficiencies of the diffraction orders [33]. Despite this the to be encoded grating function itself can still be represented by a linear bijective operator so that IFTA can be used for its design. This does require a translation map between the designed coding scheme and microstructure profile.

The coding scheme comes in an on and off-axis variant. The on-axis scheme is shown in section 4.3.1 and encodes the profile into the zeroth order of (a given) sub-wavelength carrier grating [32]. The fill factor of this grating is modified by changing the microstructure size in each period (smoothly) so that the effective refractive index is (locally) modulated. In this manner the grating profile can be encoded if the relationship between the fill-factor and effective refractive index is known.

For the off-axis variant shown in section 4.3.2 the phase of the field is modulated by varying the position of the V-shaped structure [29]. This scheme splits the first diffraction order of the carrier grating as described by the encoded (periodic) modulation of groove location.

4.3.1 V-groove modulation

V-groove modulation is based on modulating the fill factor analogously to what has been done with binary sub wavelength periodic gratings in the past [30]. As grooves are used the structure is y-invariant so that only 1-D designs are considered.

A side view of the V-groove structure and the fill factor modulation concept are illustrated in Figure 4.14. In this figure d denotes carrier grating period, i.e. the size of a single microstructure, while the super-period D encompasses one period of the entire encoded profile. The width of the V-grooves w is altered while the apex half angle α remains fixed. The grating structure that is considered and an FMM analysis of the microstructure are provided by [34]. The V-grooves with half angle $\alpha = 35.26°$ determined by the wet-etching characteristics of $\langle 100 \rangle$ Si wafer, allow easy fabrication. The grooves are carved into Cyclo Olefin Copolymer (COC), a material with refractive index $n = 1.52$. For this purpose the carrier grating with period $d \leq \lambda$ has its groove width altered as function of position as illustrated in Figure 4.14.

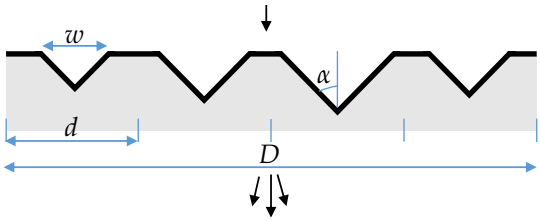

Figure 4.14: Using various sizes of V-grooves to encode a grating profile.

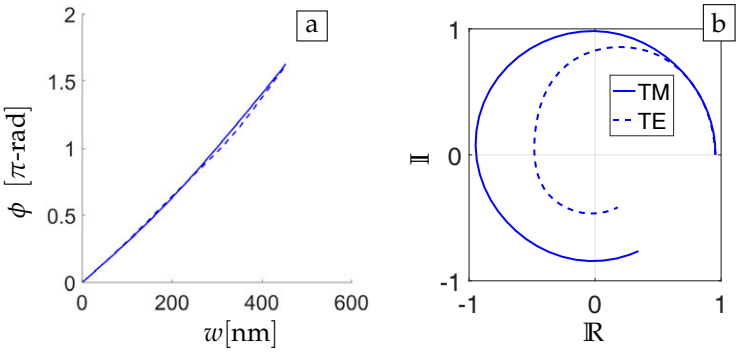

Figure 4.15: a) The relation between the induces phase shift of the transmitted light and the width V-groove grating structure. The for normal incident light of wavelength $\lambda = 457$ nm. In b) the phase-amplitude relation is shown on the complex plane. This data was obtained via the FMM method and provided by Gaurav Bose.

From FMM analysis the transmission of a single grating period with groove width w and fixed period $d = \lambda$ was obtained and is illustrated in Figure 4.15. The figure shows the relation between the induced phase delay and groove width for both TE and TM polarized light with a wavelength of $\lambda = 457$ nm. Figure 4.15(b) shows the amplitude-phase relation on the complex plane. The efficiency for TM polarized light suffers significantly when the groove width approaches the wavelength of the light while the phase remains more or less the same. The induced

phase shift is however limited to $0 \leq \phi \lesssim 1.65\pi$ and would be shrunk further to $0 \leq \phi \lesssim 1.5\pi$ in order to satisfy the $d - w \gtrsim 50$ nm fabrication constraint.

The difference in TE and TM response would require one to choose to design for either TE, TM, or a compromise between the two as projection onto the constraint A_c or its resulting output would differ. In this case the projection onto A_c is very similar for both TE and TM states of polarization so that the SRE is maximized for both in the target area W. But as the amplitudes differ the resulting (diffraction order) output will not match in uniformity when either designing for TE or TM only. This means that in IFTA one can not make the tradeoff of sacrificing some efficiency to improve uniformity for both TE and TM.

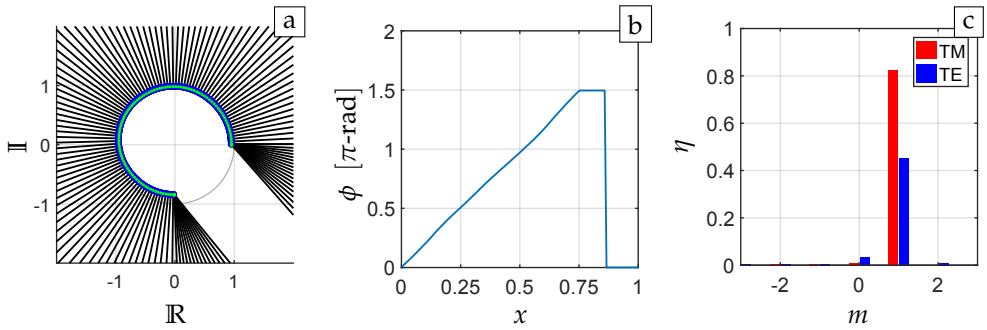

Figure 4.16: a) Projection onto A_c for TM polarized light. b) Phase profile from projection, the slight curve in the ramp is due to varying amplitudes of A_c. c) The diffraction order efficiencies for phase profiles for TE and TM polarized light (under paraxial-thin element approximation).

As a proof of principle Figure 4.16 shows the single diffraction order design for TM polarized light. The resulting profile lies very close to the ideal profile for TE polarized light as the projection operator ends up with basically the same phase profile. It should be noted that the diffraction profile was obtained from IFTA-consideration and was not rigourously modeled with FMM. Furthermore in practice the number of V-grooves used to encode the grating profile is limited which would make the profile itself discrete instead of continuous. These differences will be shown in the next section on V-ridge gratings.

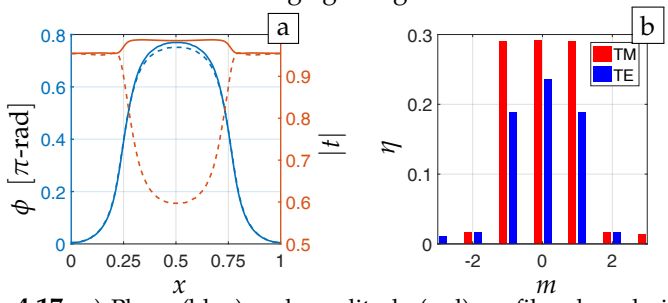

Figure 4.17: a) Phase (blue) and amplitude (red) profile when designing a triplicator, caring for TM polarization only. The solid line shows the TM response and dashed the TE response. b) The resulting diffraction order profiles for TE and TM polarized light. A mismatch occurs due to differences in amplitude response.

The V-grooves can also be used in reflection mode by applying an aluminium coating for instance. This configuration results in TE polarized light only weakly in-

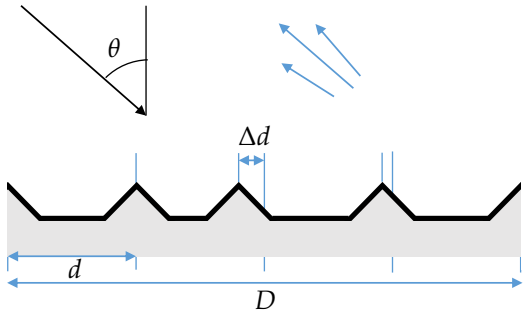

Figure 4.18: Lohmann's detour-phase principle shown for a V-ridge grating. The carrier grating maximizes the $m = -1$ diffraction order and the grating modulation splits it up into the encoded diffraction order profile.

teracting with the V-groove structures as light in this polarization state has trouble penetrating and this results in a minimal phase delay. At the same time TM polarized light excites a plasmon resonance that eat up the efficiency along a broad range of V-groove width's [34]. As will be shown in next chapter the V-ridge gratings do not suffer from these problems.

4.3.2 Detour-phase principle with V-ridge grating

Figure 4.18 illustrates a periodic V-ridge carrier grating that has the positions of the V-ridge's modulated to encode a desired grating profile. The carrier grating has a period d, is made of bulk aluminium with refractive index $n = 0.6402 + i5.5505$ and has a V-ridge with a base width of w and half-apex angle $\alpha = 35.26°$. Hence adjacent ridges are separated by flat sections of width d-w. The shape and size of the V-ridges is fixed while the positions of the structures are displaced with respect to their periodic position by Δd. This displacement does not affect the phase of the zeroth reflected diffraction order of the grating but will disturb the other diffraction orders such as the $m = -1$ diffraction order of the carrier grating. The advantage of this encoding method is that the properties of the encoded grating, such as acceptance angle and wavelength response, is in a large part determined by the carrier grating properties.

Carrier grating

Under the assumption of a TM polarized monochromatic plane wave illumination, the reflected $m = -1$ diffraction order efficiency was optimized. This was done by first choosing θ and d such that only the reflected diffraction orders $m = -1$ and $m = 0$ propagate, i.e. by satisfying the Bragg condition:

$$\sin\theta = \frac{\lambda_0}{2d}. \tag{4.14}$$

For this design the wavelength $\lambda_0 = 457$ nm and incidence angle $\theta = 42°$ are used so that the optimal carrier grating period becomes $d \approx 340$ nm. By use of FMM analysis the V-ridge width $w \approx 220$ was found to maximize the carrier efficiency η_{-1}. The resulting carrier grating has an efficiency of $\eta_{-1} \approx 87\%$, this lies close to the reflection coefficient of an air-aluminium interface which lies somewhere between

86% to 91% depending on the angle of incidence. The efficiency of $\eta_{-1} \approx 87\%$ does not change much under changing angle of incidence $\theta = [0^\circ \dots 60^\circ]$ or wavelength $\lambda = [406 \dots 520]$ nm [35]. With these choices the absorption due to plasmonic excitation is mainly avoided as the grating period is then smaller than what is required for plasmon resonance.

The TE polarization has difficulty in penetrating the metallic sub-wavelength grooves and as a consequence only a small phase modulation induced by the minimal interaction limits the η_{-1} diffraction order efficiency for TM polarized light to $\sim 50\%$.

Coding of the carrier grating

Shifting a grating laterally induces a phase shift in the first diffraction order proportional to the lateral shift as shown in Figure 4.18. A local displacement of the grating structures can be seen as a local displacement of the grating so that in turn the first diffraction order is phase-shifted in accordance to the introduced displacement [29]. The induced phase shift is not bound to the interval $[0, 2\pi)$ and is encoded by the detour phase principle as

$$\phi(x_n) = 2\pi \frac{\Delta d(x_n)}{d}. \tag{4.15}$$

In here the location $x_n = (n - 1/2)d$ denotes the undisturbed location of the n'th structure and $\Delta d(x_n)$ the shift of that structure with respect to location x_n. It is assumed that the phase function $\phi(x_n)$ varies slowly

$$|\phi(x_n) - \phi(x_{n+1})| \ll 2\pi \ \ \forall n, \tag{4.16}$$

so that adjacent ridges do not overlap and the grating can locally be considered periodic. By means of phase unwrapping any 2π jumps can be removed from a 1-D designs as the phase is not limited to the $[0, 2\pi)$ range. For jumps other then a 2π it is assumed that they lie isolated so that the encoded profile is only disturbed locally.

The resulting grating consists of a carrier grating design with period d that is designed to maximize the $m = -1$ diffraction order. This carrier grating is spatially modulated in accordance to Eq. (4.15) so that the encoded phase profile is repeated within every super period $D = Nd$, $\phi(x + D) = \phi(x)$, with N being the number of carrier grating periods in a single super period. As such the encoded phase profile splits the $m = -1$ diffraction order out into the desired diffraction order pattern.

V-ridge designs & results

A number of array-illuminator designs were considered for fabrication, namely a grating that distribute an incident TM-polarized plane wave in either three, five or eight equal-amplitude diffraction orders. As the Lohmann detour-phase principle only alters phase the three beam profile is given by the ideal triplicator profile of Eq. B.43 while the latter of the two can be obtained by IFTA.

For a V-ridge grating with super period $D = Nd$ consisting of N carrier grating periods, the diffraction orders of the beam-splitters are centered on the N^{th} diffraction order. The number of v-ridge elements will determine how well sampled the grating profile is and thereby the accuracy of the detour-phase principle. Increasing N will decrease the phase jumps between adjacent elements and thereby the periodic nature of the carrier grating becomes more apparent. The number of V-ridges

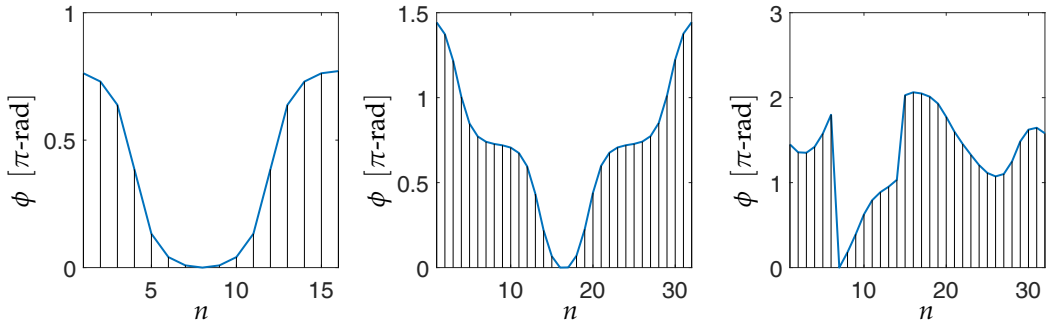

Figure 4.19: The IFTA profiles that create a three ($N = 16$), b) five ($N = 32$) and c) eight ($N = 32$) equal diffraction orders. *Adapted from Ref. [35]*

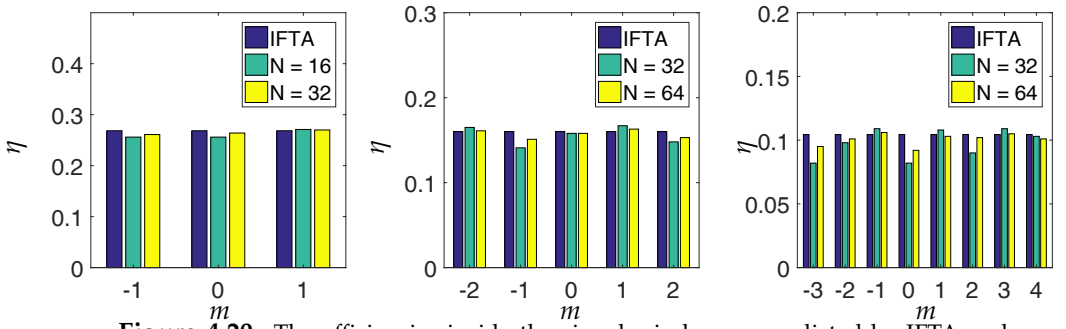

Figure 4.20: The efficiencies inside the signal window as predicted by IFTA and FMM for a) three, b) five and c) eight equal diffraction orders. The shown zeroth diffraction order is actuality centered on the $m = -N$ diffraction order for the V-ridge grating. *Adapted from Ref. [35]*

will also determine the complexity of the encoded modulation that one can achieve, a sufficient number of V-ridge elements should be taken to ensure that the desired signal can be adequately represented in the output domain.

Figure 4.19 shows the phase profiles of the three different beam splitter designs for the triplicator with $N = 16$ and the five and eight diffraction order design with $N = 32$. Under IFTA assumptions the shown phase profiles obtain the desired diffraction order pattern without error in the signal window. The three, five and eight beam designs have efficiencies of $\eta \approx 0.926$, $\eta \approx 0.92$ and $\eta \approx 0.96$ respectively.

To see how well the thin element approximation and Lohmann detour-phase principle hold up the phase profiles shown in Figure 4.19 were encoded in the V-ridge grating and simulated with FMM. In this computation it was assumed that the input field consists of a TM-polarized plane wave coming in under $\theta = 42^\circ$ with a wavelength of $\lambda = 457$ nm. The resulting diffraction order amplitudes are illustrated in Figure 4.20. In this figure the IFTA design efficiency was scaled by multiplying with the V-groove carrier grating efficiency $\eta_{-1} \approx 87\%$ for a more direct comparison. The figure also shows that the uniformity improves when the number of v-ridge elements is increased.

The triplicator with $N = 16$ was fabricated and tested in order to validate the simulation results. The measured grating response is shown in Figure 4.21 together with the simulated grating response. As the figure illustrates the grating has a consistent performance over a large set of incidence angles and wavelengths due to

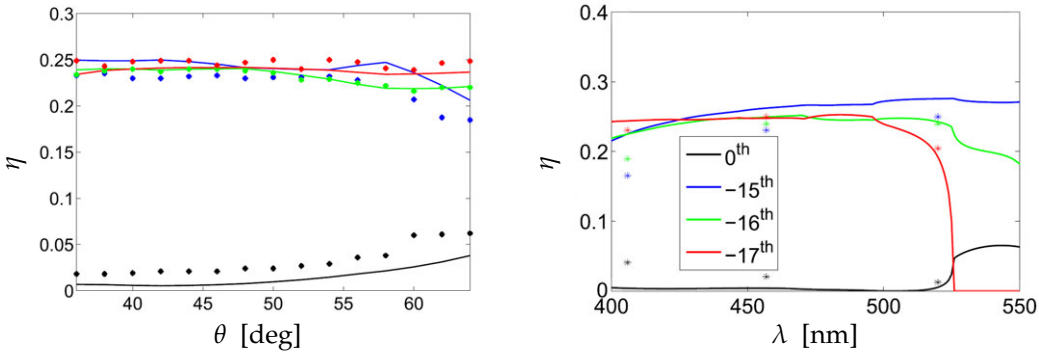

Figure 4.21: The diffraction order efficiencies of the simulated (solid lines) and measured (asterisk-symbol) v-ridge triplicator gratings as functions of a) angle of the incidence and b) wavelength. *Adapted from Ref. [35]*

the nature of the V-grooves. The experimental data is in good agreement with the theory, see [35] for more details.

5 Spatial Coherence

5.1 INTRODUCTION

This chapter starts off with the general description of the second order coherence properties of a non-stationary pulsed electromagnetic field. The conditions are found under which such a field can be accurately described by only using a stationary scalar description of its second order coherence properties. After this the Gaussian Shell Model (GSM) is introduced and the elementary mode model derived for this source description. These are the conditions on which the simulations of X-ray beam lines in Chapter 7 are based.

5.2 COHERENCE X-RAY ASSUMPTIONS

Suppose a pulsed non-stationary random electromagnetic field $\mathbf{E}(\rho;t)$, with $\mathbf{E} = [E_x \;\; E_y \;\; E_z]$ traveling along the z-direction. If one considers a series of field realizations $\mathbf{E}_i(\mathbf{r};t)$ at position $\mathbf{r} = (\rho,z) = (x,y,z)$ that more or less fluctuate randomly between two spatial and frequency coordinates then a statistical description would be appropriate. Looking at the ensemble averaged pulse fields at the transverse plane z = constant yields the second order coherence properties, which are fully described by the two-time Mutual Coherence Function (MCF) matrix

$$\Gamma(\rho_1,\rho_2;t_1,t_2) = \left\langle \mathbf{E}^*(\rho_1;t_1)\mathbf{E}^T(\rho_2;t_2) \right\rangle \tag{5.1}$$

$$= \lim_{N\to\infty} \frac{1}{N} \sum_{i=1}^{N} \mathbf{E}_i^*(\rho_1;t_1)\mathbf{E}_i{}^{\mathrm{T}}(\rho_2;t_2). \tag{5.2}$$

with the constant z coordinate omitted for brevity. The asterisk stands for the complex conjugation, T the transpose operator and the brackets $\langle\rangle$ denote the ensemble average over all electromagnetic field realizations. The ensemble average may represent the coherence properties of a pulse train where the individual fields $\mathbf{E}_i$ for example are individual pulses of a Free Electron Laser (FEL) X-ray source. The individual electric field realization (pulse) can be written both as a space-frequency realization and as a space-time realization as they form a Fourier transform pair [2]

$$\tilde{\mathbf{E}}(\rho,\omega) = \frac{1}{2\pi} \int_{-\infty}^{\infty} \mathbf{E}(\rho;t)\exp(+i\omega t)dt \tag{5.3}$$

$$\mathbf{E}(\rho;t) = \int_{0}^{\infty} \tilde{\mathbf{E}}(\rho,\omega)\exp(-i\omega t)d\omega. \tag{5.4}$$

This allows the statistical properties of the field also to be fully described by the Cross-Spectral Density (CSD) matrix

$$W(\rho_1,\rho_2;\omega_1,\omega_2) = \left\langle \tilde{\mathbf{E}}^*(\rho_1;\omega_1)\tilde{\mathbf{E}}^T(\rho_2;\omega_2)\right\rangle. \tag{5.5}$$

$$= \frac{1}{4\pi^2}\iint_{-\infty}^{\infty}\Gamma(\rho_1,\rho_2;t_1,t_2)\exp[-i(\omega_1 t_1-\omega_2 t_2)]\mathrm{d}t_1\mathrm{d}t_2. \tag{5.6}$$

When considering a paraxial field (such as produced by X-ray beams), the 3×3 matrices of the MCF and CSD can be reduced to 2×2 matrices by dropping the negligible E_z component [42].

For a field with spatially uniform polarization across the beam, the field can be written as

$$\mathbf{E}(\rho,t) = \mathbf{A}(t)e(\rho;t)\exp(-i\omega_0 t), \tag{5.7}$$

with $\mathbf{A}$ a random (fast-varying) polarization vector, $e(\rho;t)$ the scalar field envelope and ω_0 the mean optical frequency of the spectrum. For such fields the MCF matrix may be written as a product between a temporal polarization matrix

$$\mathbf{J}(t_1,t_2) = \left\langle \mathbf{A}^*(t_1)\mathbf{A}^T(t_2)\right\rangle \tag{5.8}$$

and the scalar MCF

$$\Gamma(\rho_1,\rho_2;t_1,t_2) = \langle e^*(\rho;t_1)e(\rho_2;t_2)\rangle\exp[i\omega_0(t_1-t_2)]. \tag{5.9}$$

If neither the polarization changes over the length of the pulse nor is altered by the system through which the field is propagated then just the scalar CSD is needed to describe the coherence properties,

$$W(\rho_1,\rho_2;\omega_1,\omega_2) = \langle\tilde{e}^*(\rho;\omega_1-\omega_0)\tilde{e}(\rho_2;\omega_2-\omega_0)\rangle \tag{5.10}$$

$$= \frac{1}{4\pi^2}\iint_{-\infty}^{\infty}\Gamma(\rho_1,\rho_2;t_1,t_2)\exp[-i(\omega_1 t_1-\omega_2 t_2)]\mathrm{d}t_1\mathrm{d}t_2. \tag{5.11}$$

The field is said to be stationary if the time correlation properties do not depend on the origin of time t_0 but only depend on time difference, i.e. $\Delta t = t_2 - t_1$. This is equivalent to saying that the different spectral components of the field are mutually uncorrelated [2] so that the two-frequency CSD would be

$$W(\rho_1,\rho_2;\omega_1,\omega_2) = W(\rho_1,\rho_2;\omega_1)\delta(\omega_1-\omega_2). \tag{5.12}$$

To see when the field can be approximated as quasi-stationary suppose that the scalar two-time MCF is separable in the form

$$\Gamma(\rho_1,\rho_2;\bar{t},\Delta t) = \Gamma_S(\rho_1,\rho_2;\bar{t},0)g(\Delta t), \tag{5.13}$$

with difference and average temporal coordinates denoted by $\Delta t = t_2 - t_1$ and $\bar{t} = (t_1+t_2)/2$ respectively. Then for a quasi-stationary field it is required that $g(\Delta t)$ is a narrow function while the spatial coherence fluctuations between two distinct points $\Gamma_S(\rho_1,\rho_2;\bar{t},0)$ vary slowly as a function of $\bar{t}$ with respect to the temporal intensity distribution $I(\rho,\bar{t}) = \Gamma(\rho,\rho;\bar{t},0)$.

Inserting Eq. (5.13) into Eq. (5.6) while using average and difference frequency coordinates $\bar{\omega} = (\omega_1 + \omega_2)/2$ and $\Delta\omega = \omega_2 - \omega_1$ gives the two-frequency CSD as

$$W(\rho_1, \rho_2; \Delta\omega, \bar{\omega}) = W_S(\rho_1, \rho_2; \Delta\omega, 0)\tilde{g}(\bar{\omega}), \tag{5.14}$$

where

$$W_S(\rho_1, \rho_2; \Delta\omega, 0) = \int_{-\infty}^{\infty} \Gamma_S(\rho_1, \rho_2; \bar{t}, 0) \exp(+i\Delta\omega\bar{t}) \mathrm{d}\bar{t} \tag{5.15}$$

and

$$\tilde{g}(\bar{\omega}) = \int_{-\infty}^{\infty} g(\Delta t) \exp(+i\bar{\omega}\Delta t) \mathrm{d}\Delta t. \tag{5.16}$$

In these equations the quasi-stationary case results in a wide $\tilde{g}(\bar{\omega})$ function (as its Fourier inverse was narrow) while $W_S(\rho, \rho; \Delta\omega, 0)$ is now narrow in the $\Delta\omega$ coordinate in comparison with the power spectrum $S(\rho, \bar{\omega}) = W(\rho, \rho, 0, \bar{\omega})$ for a given ρ.

The function $W_S(\rho_1, \rho_2, \Delta\omega, 0)$ can therefore be written as

$$W_S(\rho_1, \rho_2; \Delta\omega, 0) = W_S(\rho_1, \rho_2)\tilde{f}(\Delta\omega), \tag{5.17}$$

$$W_S(\rho_1, \rho_2) = W_S(\rho_1, \rho_2, 0, 0) = \Gamma_S(\rho_1, \rho_2, 0, 0), \tag{5.18}$$

with $W_S(\rho_1, \rho_2)$ being the spatial part of the CSD. This relation can only hold if the spatial coherence properties do not change (significantly) over a time scale in the order of the coherence time. Under this condition the field can be modeled at a single frequency, e.g. the central frequency ω_0 of the field.

Hence for a pulsed non-stationary field to be described by a scalar MCF requires that the field is paraxial and has a uniform polarization both spatially and temporally on the time scale of the pulse. Furthermore the system through which the field propagates should not change its polarization (significantly).

The pulsed non-stationary field can also be considered quasi-stationary if the MCF is of the form of Eq. (5.13) while also requiring that the spatial coherence properties do not vary significantly during the coherence time scale of the pulse. Under these conditions only the spatial component of the scalar MCF and CSD needs to be considered at the central frequency $\omega = \omega_0$ of the pulse.

5.3 REPRESENTING THE CSD/MCF

It is assumed that the field under consideration is a stationary field with frequency ω_0, and can be fully described by the scalar description of the CSD/MCF. In free space one could directly propagate the second order correlation functions directly as they, like the fields themselves, obey wave equations [2]

$$\nabla_1^2 \Gamma(\mathbf{r}_1, \mathbf{r}_2, \Delta t) = \frac{1}{c^2} \frac{\partial^2}{\partial \Delta t^2} \Gamma(\mathbf{r}_1, \mathbf{r}_2, \Delta t), \tag{5.19}$$

$$\nabla_2^2 \Gamma(\mathbf{r}_1, \mathbf{r}_2, \Delta t) = \frac{1}{c^2} \frac{\partial^2}{\partial \Delta t^2} \Gamma(\mathbf{r}_1, \mathbf{r}_2, \Delta t), \tag{5.20}$$

and Helmholtz equations

$$\nabla_1^2 W(\mathbf{r}_1, \mathbf{r}_2, \bar{\omega}) = k^2 W(\mathbf{r}_1, \mathbf{r}_2, \bar{\omega}), \tag{5.21}$$

$$\nabla_2^2 W(\mathbf{r}_1, \mathbf{r}_2, \bar{\omega}) = k^2 W(\mathbf{r}_1, \mathbf{r}_2, \bar{\omega}), \tag{5.22}$$

where $k = 2\pi n/\lambda$, $\lambda = 2\pi c/\omega$ the wavelength in vacuum and the symbol ∇_i represents the derivative with respect to $\mathbf{r}_i$, $i = 1, 2$.

This means that the same diffraction integrals (e.g. Rayleigh first diffraction integral and various approximations thereof) can be used to propagate the MCF/CSD but now integrating over all four space coordinates (x_1, y_1) and (x_2, y_2) instead of the usual two (x, y). This in itself is a numerically resource intensive task that one can avoid.

To circumvent the 4-D integrals one would like to expand the CSD into a set of basis functions that can be propagated independently. A Mercer-type coherent mode expansion [2, 70] would require that the cross-spectral density functions are Hermitian, non-negative definite Hilbert-Schmidt kernels. For this it is required that they are square integrable

$$\iint_{-\infty}^{\infty} |W(\rho_1, \rho_2)|^2 \mathrm{d}^2\rho_1 \mathrm{d}^2\rho_2 < \infty, \tag{5.23}$$

nonnegative definite

$$\iint_{-\infty}^{\infty} W(\rho_1, \rho_2) f^*(\rho_1) f(\rho_2) \mathrm{d}^2\rho_1 \mathrm{d}^2\rho_2 \geq 0, \tag{5.24}$$

with $f(\rho)$ being any square integrable function, and hermitian

$$W(\rho_1, \rho_2) = W^*(\rho_1, \rho_2). \tag{5.25}$$

Luckily in the real world, fields have finite extent and finite energy so that Eq. (5.23) is satisfied and any intensity function of a field is a real-non-negative function as required by Eq. (5.24). The CSD and MCF are also Hermitian functions, as for two complex random processes $z_1(t)$ and $z_2(t)$ that are jointly stationary, the relation $\langle z_1^*(t) z_2(t+\tau) \rangle = \langle z_2(t) z_1^*(t-\tau) \rangle$ holds so that likewise the MCF is Hermitian and by extension of Eq. (5.6) the CSD is as well. This Hermitian property will result in both MCF and CSD being mirror-symmetric with respect to the 'line' described by $\rho_1 = \rho_2$.

The Mercer-type coherent-mode expansion that follows from these requirements yields a CSD of the form [2, 44]

$$W(\rho_1, \rho_2) = \langle E^*(\rho_1) E(\rho_2) \rangle \tag{5.26}$$

$$= \sum_{m=0}^{\infty} a_m \psi_m^*(\rho_1) \psi_m(\rho_2), \tag{5.27}$$

where a_m are real non-negative weight factors of the eigenfunctions $\psi_m(\rho)$. The series in Eq. (5.27) is absolutely and uniformly convergent. The eigenfunctions and eigenvalues themselves can be computed from the CSD by solving the Fredholm integral equation

$$\int_{-\infty}^{\infty} W(\rho_1, \rho_2) \psi_m(\rho_1) \mathrm{d}^2\rho_1 = a_m \psi_m(\rho_2). \tag{5.28}$$

When these eigenvalues and eigenfunctions are known they can be propagated with two-dimensional integrals.

If the CSD can be expressed as a Mercer-type coherent mode expansion, it they can also be written in the form [69–71]

$$W(\rho_1, \rho_2) = \int_{-\infty}^{\infty} p(v_x) H^*(\rho_1, v_x) H(\rho_2, v_x) \mathrm{d}v_x \tag{5.29}$$

with $p(v_x)$ being a non-negative weight function and $H(\rho, v_x)$ an arbitrary kernel. This alternative representation also only needs two-dimensional integrals to be propagated and will be used in the next section for a simple representation of so called Gaussian Shell model sources.

5.4 GAUSSIAN SHELL MODEL SOURCES

Assuming a scalar field description and dropping the frequency dependency for brevity, the CSD of a stationary source is

$$W(\rho_1, \rho_2) = \langle E^*(\rho_1) E(\rho_2) \rangle \,. \tag{5.30}$$

The spectral density of the field indicates the intensity of the field at position ρ and frequency ω:

$$S(\rho) = \langle |E^*(\rho) E(\rho)| \rangle \,. \tag{5.31}$$

Using this one can normalize the CSD as

$$\mu(\rho_1, \rho_2) = \frac{W(\rho_1, \rho_2)}{\sqrt{S(\rho_1) S(\rho_2)}}, \tag{5.32}$$

which is also known as the complex degree of spectral coherence. The value of μ is bound by $0 \leq |\mu(\rho_1, \rho_2)| \leq 1$, where 1 indicates complete correlation and 0 no correlation between the fields at the two spatial points ρ_1 and ρ_2.

By approximation many light sources obey the Shell model, in which the spatial coherence properties of the source only depend on coordinate difference $\Delta\rho = \rho_2 - \rho_1$ and not their absolute values at ρ_1 or ρ_2. For a stationary scalar field description, the Shell Model CSD is of the form [37, 45]

$$W(\rho_1, \rho_2) = \sqrt{S(\rho_1) S(\rho_2)} \mu(\Delta\rho). \tag{5.33}$$

A special class of Shell model sources are those that have a Gaussian kernel so that it is referred to as the Gaussian Shell Model (GSM). In this model both the spectral density and degree of spatial coherence are assumed to be Gaussian in shape at the source plane:

$$S(\rho) = S_0 \exp\left(-\frac{2||\rho||^2}{w_0^2} \right), \tag{5.34}$$

$$\mu(\Delta\rho) = \exp\left[-\frac{||\rho_1 - \rho_2||^2}{2\sigma_0^2} \right]. \tag{5.35}$$

This gives

$$W(\rho_1,\rho_2) = S_0 \exp\left(-\frac{||\rho_1||^2 + ||\rho_2||^2}{w_0^2}\right) \exp\left[-\frac{||\rho_1 - \rho_2|\,|^2}{2\sigma_0^2}\right], \tag{5.36}$$

where w_0 represents the $1/e^2$ width of the intensity profile and σ_0 the spatial coherence width at the waist. The L2-norm was used to write $||\rho|| = \sqrt{x^2+y^2}$. In principle w_0 and σ_0 would depend on the wavelength, but as the sources are considered narrow-banded this dependency is omitted.

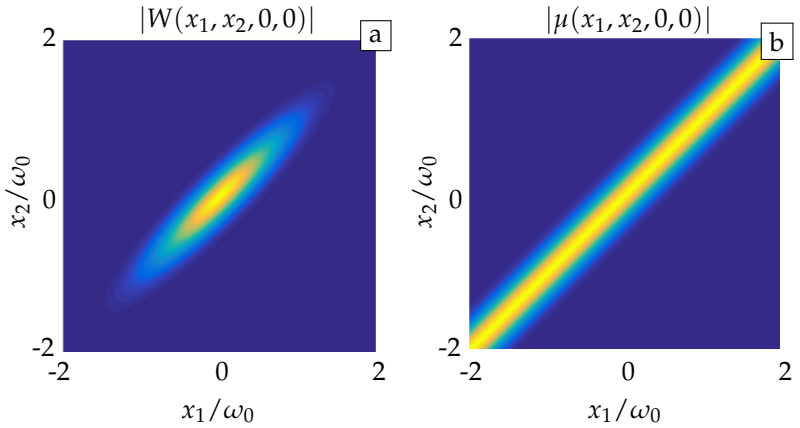

Figure 5.1: A cross-section of the (a) CSD and (b) normalized CSD for a GSM source with $\beta = 0.2$.

Propagating the GSM beam through free-space only alters its width, amplitude, and coherence width while keeping its shape of the spectral density and spatial coherence Gaussian [41]. The field expands as

$$w(z) = w_0\sqrt{1+(z/z_R)^2} \tag{5.37}$$

$$z_R = \pi w_0^2 \beta/\lambda \tag{5.38}$$

$$\beta = \left[1+(w_0/\sigma_0)^2\right]^{-1/2}. \tag{5.39}$$

so that the propagated CSD is obtained by replacing w_0 with $w(z)$ in Eq. (5.36) and σ_0 with $\sigma(z)$ by making use of the propagation invariant quantity $\sigma(z)/w(z) = \sigma_0/w_0$. The value

$$\theta_0 = \frac{\lambda}{\pi w_0 \beta} \tag{5.40}$$

defines the $1/e$ (far field) beam divergence angle and can be used in combination with the source size (and wavelength) to estimate the value of β for a GSM source.

Figure 5.1 illustrates the CSD and complex degree of coherence for this model as functions of x_1 and x_2 while $(y_1, y_2) = (0, 0)$.

5.4.1 Hermite Gaussian Shell Model

For the GSM source the solution to the Fredholm integral equation (5.28) is known in closed form and is given by [46]

$$W(\rho_1, \rho_2) = \sum_{m=0}^{\infty} a_m \psi_m^*(\rho_1)\psi_m(\rho_2), \tag{5.41}$$

where

$$\psi_m(x) = \left(\frac{2}{\pi}\right)^{1/4} \frac{1}{\sqrt{2^m m! w_c}} H_m\left(\frac{\sqrt{2}x}{w_c}\right) \exp\left(-\frac{x^2}{w_c^2}\right) \tag{5.42}$$

and

$$a_m = S_0 \frac{\sqrt{2\pi} w_0}{1 + 1/\beta} \left(\frac{1-\beta}{1+\beta}\right)^m, \tag{5.43}$$

with $w_c = \sqrt{\beta} w_0$ and the mode weight being indicated by a_m. This representation by Hermite Gaussian basis functions is also referred to as the Hermite Gaussian Shell Model (HGSM). Each mode represents a fully coherent field, allowing the use of 2-D integrals for propagating it.

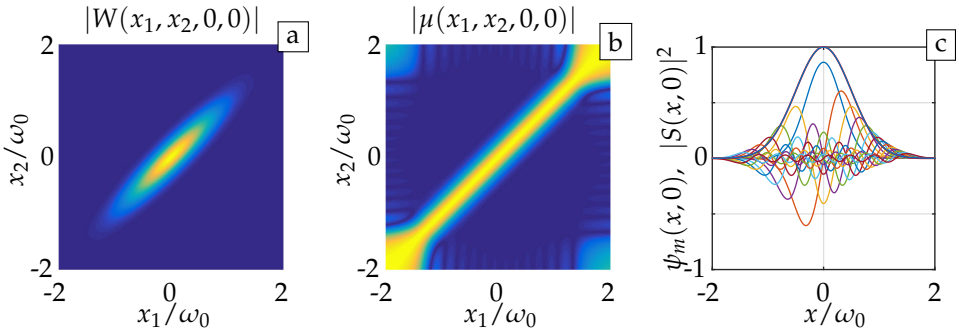

Figure 5.2: A cross-section of the (a) CSD and (b) normalized CSD for a HGSM source with $\beta = 0.2$ with (c) $N = 13$ modes. The figure with the 13 modes also shows the cross-section of the intensity profile $|S(x,0)|^2$ in red. The errors that pop up at the edges of the normalized CSD are located where the amplitude of the CSD becomes vanishingly small. These errors in the normalized CSD can therefore be safely ignored as almost no energy of the field is present where they occur.

In practice only a finite number of Hermite Gaussian modes are taken. Figure 5.2 illustrates where errors occur in the normalized CSD when a limited number of these Hermite Gaussian modes are taken. In this particular case the errors that occur at the edges of the shown complex degree of coherence function occur in regions where the field has almost no energy.

To know how many Hermite Gaussian modes are needed, let us define the error as the amount of energy difference ΔI in the intensity profile (spectral density) between the exact representation and truncating at N modes:

$$\Delta I = \frac{\iint \left| \sum_{m=0}^{\infty} a_m \psi_m^*(\rho)\psi_m(\rho) - \sum_{m=0}^{N} a_m \psi_m^*(\rho)\psi_m(\rho) \right| \mathrm{d}^2\rho}{\iint \left| \sum_{m=0}^{\infty} a_m \psi_m^*(\rho)\psi_m(\rho) \right| \mathrm{d}^2\rho}. \tag{5.44}$$

The functions $a_m \psi_m \psi_m^*$ are real and positive so that the truncated sum over those positive valued functions is always smaller than the full sum, which allows the absolute values to be dropped. Furthermore integrating over the normalized function

yields the same value for all m so that after inserting a_m the truncation error becomes

$$\Delta I = 1 - \frac{2}{1+1/\beta} \sum_{m=0}^{N} \left(\frac{1-\beta}{1+\beta}\right)^m \tag{5.45}$$

$$= \left(\frac{1-\beta}{1+\beta}\right)^{N+1}. \tag{5.46}$$

Note that for incoherent light, β close to 0, the number of modes needed for accurately representation grows greatly. Specifically the higher Hermite Gaussian modes oscillate rapidly, which makes numerical computation more expensive/difficult to do accurately.

As shown in Appendix C, the Gaussian Shell model can also be written in the form of Eq. (5.29). This description by way of a superposition of shifted Gaussian elementary modes is given in the next section.

5.4.2 Elementary Mode Representation

For the elementary mode description the CSD is written as [38–40]

$$W(\rho_1, \rho_2) = \int_{-\infty}^{\infty} P(\mathbf{v}) e^*(\rho_1 - \mathbf{v}) e(\rho_2 - \mathbf{v}) \, \mathrm{d}^2\mathbf{v} \tag{5.47}$$

where $e(\rho)$ denotes the fully-coherent elementary field and $P(\mathbf{v})$ the non-negative weight for the elementary mode at spatial coordinate $\mathbf{v} = (v_x, v_y)$.

In the sense of GSM, the normalized elementary field is a normalized coherent Gaussian mode. Taking the source plane at $z = 0$ and assuming a paraxial source description the shifted elementary field takes the form

$$e(\rho, \mathbf{v}, z) = \left(\frac{2}{\pi}\right)^{1/4} \frac{1}{\sqrt{w_\mathrm{e}}} \frac{w_\mathrm{e}}{w_\mathrm{e}(z)} \exp\left[i\left(kz - \Phi(z)\right)\right] \times \exp\left(-\frac{|\rho - \mathbf{v}|^2}{\omega_e^2}\right) \exp\left[\frac{ik}{2R(z)} |\rho - \mathbf{v}|^2\right], \tag{5.48}$$

with $w_\mathrm{e} = \beta w_0$ being the $1/e$ width of the elementary field at its waist. The parameters

$$w_\mathrm{e}(z) = w_\mathrm{e}\sqrt{1 + z^2/z_\mathrm{R}^2}, \tag{5.49}$$

$$\Phi(z) = \arctan\left(z/z_\mathrm{R}\right), \tag{5.50}$$

$$R(z) = z + z_\mathrm{R}^2/z, \tag{5.51}$$

$$z_\mathrm{R} = k w_\mathrm{e}^2/2 \tag{5.52}$$

are the propagation parameters of the standard fully coherent Gaussian beam [2].

The weight function $P(\mathbf{v})$ is given by

$$P(\mathbf{v}) = p_0 \exp\left(-\frac{2|\mathbf{v}|^2}{w_\mathrm{p}^2}\right), \tag{5.53}$$

$$p_0 = \frac{S_0}{\sqrt{1-\beta^2}}. \tag{5.54}$$

The quantities w_e and w_p are given by (Appendix C):

$$w_e = \beta w_0, \tag{5.55}$$

$$w_p = \sqrt{1-\beta^2} w_0. \tag{5.56}$$

The identical shape of each mode can be particulary useful if the input field is located at an aplanatic region of the optical system. In the aplanatic region the response to each laterally shifted mode is the same. In such a case the partially coherent field can be obtained at the end of the optical system by only propagating a single elementary mode through it and convolving the result with the weight function $P(\mathbf{v})$.

When such a shortcut can not be applied the integral over all positions is numerically approximated by a Riemann sum. For brevity of notation only 1D fields are considered, i.e. $\rho = (x, 0)$. To this end the weight function $P(v_x)$ is sampled at discrete locations according to the midpoint rule $v_{x,i} = (i - N/2 - 1/2)\Delta v_x$, with $i \in \{1, 2, ..., N\}$. The CSD is then given by

$$W(x_1, x_2) \approx \Delta v_x \sum_{i=1}^{N} P(v_{x,i}) e^*(x_1 - v_{x,i}) e(x_2 - v_{x,i}). \tag{5.57}$$

For accurate representation both the spacing between the modes Δv_x and the number of elementary modes N must be determined. The truncation of the number of modes can only be made if the modes adequately sample the optical system they are propagated through, i.e. it is assumed that adjacent modes do not vary greatly. Hence the spacing between the modes (and number of modes) not only depends on β but also on how sensitive the optical system is to lateral displacement of the field. At the waist of the source the error can be quantified by use of the same definition for error as in Eq. (5.44),

$$\Delta I = \int_{-\infty}^{\infty} \left| w_0 \sqrt{\frac{2}{\pi}} \exp\left(-\frac{2x^2}{w_0^2}\right) - \frac{\Delta v_x w_0}{\beta w_p} \sum_{i=1}^{N} \exp\left(-\frac{2v_{x,i}^2}{w_p^2}\right) \exp\left(-\frac{2(x - v_{x,i})^2}{w_e^2}\right) \right| dx, \tag{5.58}$$

for which no analytical expression could be found. To keep errors within bounds a large enough portion of the weight function $P(v_x)$ should be sampled by choosing $N \geq 3w_p/\Delta v_x$. The elementary modes should at least partially overlap, which is ensured if $\Delta v_x \leq 0.8 w_e$.

If the modes are spaced slightly too far apart then the CSD will show undersampling errors as shown in Figure 5.3. In this figure a GSM source with $\beta = 0.2$ is represented by $N = 13$ modes spaced $\Delta v_x = 1.25 w_e$ apart.

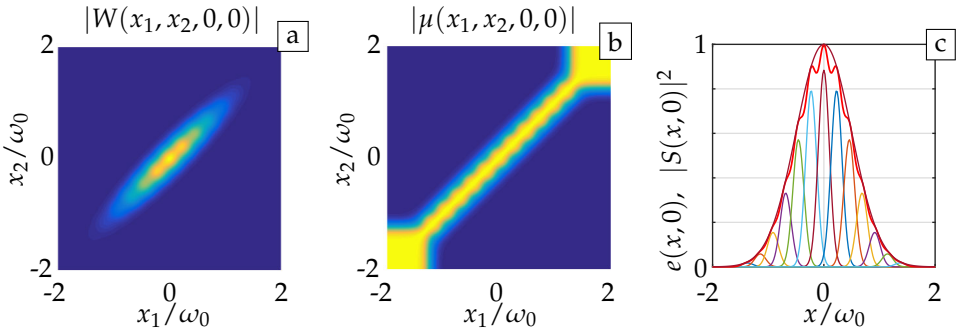

Figure 5.3: A cross-section of the (a) CSD and (b) normalized CSD for a GSM source with $\beta = 0.2$ represented with (c) $N = 13$ Gaussian elementary modes. This figure also shows the cross-section of the intensity profile $|S(x,0)|^2$ in red.

6 Field Propagation Operators

6.1 INTRODUCTION

A number of approaches to model field propagation in X-ray systems exist [49–52] most relying on ray-tracing techniques with various levels of wave-optics related features. In ray optics field information is contracted to a single point and propagated through space. In this diffraction is typically ignored or modeled by various ray-equivalent approximations. The operators and propagation methods described here are part of the Virtual Fusion software package [61] and aim to provide a full EM field description at any point in the optical system with the least amount of computational effort possible.

In field tracing the goal is to solve the Maxwell equations for an optical system given an input field, the propagation media and optical components along the way. This task can be conceptually visualized as a series of free-space propagation operations and optical component operators in a field tracing diagram. An example of such a field tracing diagram is illustrated in Figure 6.1.

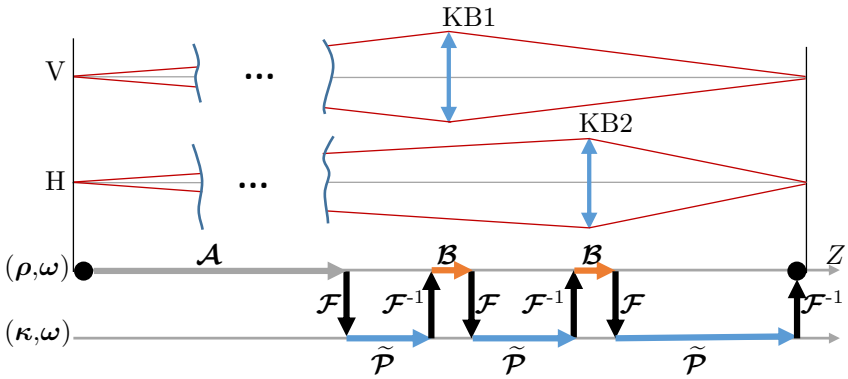

Figure 6.1: The horizontal and vertical cross-sections of the setup with below the field tracing diagram used for the optical modeling of the setup. The field tracing diagram indicates in which order the operators are used to propagate the input field through the optical system.

Ideally the chosen operators solve the Maxwell equations with a high degree of accuracy with minimal computational cost. This can be done leveraging specialized Maxwell solvers that are able to (efficiently) solve the Maxwell equations under a specific set of constraints. These solvers can range from analytical solutions to specific problems, numerical solutions under specific constraints or more general rigorous Maxwell solvers. Choosing which approach fits the problem requires a catalogue of these solvers, knowledge in which domain they solve their problem accurately, an estimation of their computation cost and the ability to switch between the methods on the fly. As the full EM field is to be determined at the end of the setup these solvers should be capable of handling the full EM field description in

their respective domain without loss of information (on phase, polarization etc.).

Of the (large) list of (possible) operators that exist only a small portion will be used to simulate the X-ray imaging setup shown in Chapter 7. An overview of the used operators is given in Table 6.1 along with the section number in which their limitations and operation are discussed.

Table 6.1: Operators that will be used to propagate an X-ray source through setup along with section that describes said operator.

$\boldsymbol{\mathcal{A}}$	Analytical equations, Section 5.4.2
$\boldsymbol{\mathcal{F}}_k$	Fourier Transform, Section 6.2
$\widetilde{\boldsymbol{\mathcal{P}}}$	Propagation Operator, Section 6.2-6.4
$\boldsymbol{\mathcal{B}}$	Plane Wave/Plane Interface, Section 6.5

6.2 SPECTRUM OF PLANE WAVES

A field $\mathbf{E}(\rho, z, \omega)$ at plane z can be decomposed into its plane wave components by way of a Fourier Transform [5, 53]

$$\widetilde{\mathbf{E}}(k_x, k_y, z, \omega) = \boldsymbol{\mathcal{F}}_k \left\{\mathbf{E}(\rho, z, \omega)\right\} \tag{6.1}$$

$$= \frac{1}{2\pi} \iint_{-\infty}^{\infty} \mathbf{E}(\rho, z, \omega) \exp\left(-ik_x x - ik_y y\right) \mathrm{d}x\mathrm{d}y. \tag{6.2}$$

In this equation the wave-vector $\mathbf{k} = (k_x, k_y, k_z)$ has its size given by the wavenumber $k = ||\mathbf{k}|| = n\omega/c = nk_0$.

This plane wave decomposition allows one to compute any of the other four EM field components from E_x and E_y. For plane waves the EM field components depend on each other as [5]

$$\widetilde{E}_z(\mathbf{k}, \omega) = -\frac{k_x \widetilde{E}_x(\mathbf{k}, \omega) + k_y \widetilde{E}_y(\mathbf{k}, \omega)}{k_z} \tag{6.3}$$

and

$$\widetilde{\mathbf{H}}(\mathbf{k}, \omega) = \sqrt{\frac{\epsilon_0}{\mu_0}} \frac{\mathbf{k} \times \widetilde{\mathbf{E}}(\mathbf{k}, \omega)}{k_0}. \tag{6.4}$$

As a result knowledge of $\mathbf{E}_\perp(\mathbf{r}, \omega) = (E_x(\mathbf{r}, \omega), E_y(\mathbf{r}, \omega))$ is sufficient to compute the entire the field in an isotropic homogenous media. Therefore only the electric field components (E_x, E_y) need to be considered during propagation as others can be computed on demand by a set of Fourier transforms [54].

Propagating $\widetilde{\mathbf{E}}_\perp(k_x, k_y, z, \omega)$ through free space over a distance of $\Delta z = z'' - z'$ between the two parallel planes located at $z = z'$ and $z = z''$ can be done by a multiplication [2, 5]:

$$\widetilde{\mathbf{E}}_\perp(k_x, k_y, z'', \omega) = \widetilde{\boldsymbol{\mathcal{P}}} \left\{\widetilde{\mathbf{E}}_\perp(k_x, k_y, z', \omega)\right\}$$

$$= \widetilde{\mathbf{E}}_\perp(k_x, k_y, z', \omega) \exp(ik_z \Delta z), \tag{6.5}$$

$$k_z = \left[k_0^2 n^2 - (k_x^2 + k_y^2)\right]^{1/2}. \tag{6.6}$$

If the planes are not parallel then an additional coordinate transform needs to be applied [55]. Both of these operations require little computational resources to perform.

The field in space domain (ρ-domain) can be obtained by an inverse Fourier transform

$$\begin{aligned}\mathbf{E}(\rho, z'', \omega) &= \mathcal{F}_k^{-1}\left\{\mathbf{E}(\rho, z'', \omega)\right\} \\ &= \frac{1}{2\pi}\iint_{-\infty}^{\infty} \widetilde{\mathbf{E}}(k_x, k_y, z'', \omega)\exp\left(ik_x x + ik_y y\right)\mathrm{d}k_x\mathrm{d}k_y \\ &= \mathcal{F}_k^{-1}\widetilde{\boldsymbol{\mathcal{P}}}\mathcal{F}_k\mathbf{E}(\rho, z', \omega),\end{aligned} \tag{6.7}$$

with the Fourier transform and propagation operators working in the indicated sequential order. So far the only the assumption of homogenous isotropic media was made for the propagation in free space operation. Any inhomogeneity in the propagation media will therefore show up in the field tracing diagram as an optical element with its appropriate (Maxwell) solver.

On the numerical side this propagation method relies on the computationally resource efficient Fourier transform operator. A sufficiently dense sampling grid over a large enough computation domain is required for this operator to work accurately. For a field with a strongly variable wavefront $\phi(\rho)$ such an approach can become prohibitively expensive as $\exp(i\phi) = \cos(\phi) + i\sin(\phi)$ will oscillate rapidly. This in turn can require a prohibitive amount of sampling points to represent accurately and Fourier transform.

It therefore makes sense to look at mapping operators that can accurately and quickly switch field representations between the x and k domains. To this point we look at the two techniques called the Semi-analytical Fourier Transform and Geometric Fourier Transform in the upcoming sections. Both of these methods avoid the oscillating term by treating it separately during the Fourier transform.

6.3 SEMI-ANALYTICAL FOURIER TRANSFORM

Computational speed can be improved significantly if fewer sampling points are needed to accurately represent the field. The concept is to treat the strong wavefront phase variation caused by a quadratic phase factor separately in the Fourier transform operator and thereby significantly reduce the sampling points required. Strong quadratic phase variation is typically acquired under propagation as it is a major term in spherical phase [57].

To treat the quadratic phase separately one first has to split the field into a quadratic phase contribution and residual field. Let $V(\rho) = V(\rho, \omega)$ denote the field component of interest, i.e. $E_x(\rho)$ or $E_y(\rho)$, at fixed plane z and given frequency ω, then

$$V(\rho) = |V(\rho)|\exp[i\phi(\rho)]\exp[i\psi_q(\rho)] = U(\rho)\exp(i\psi_q(\rho)), \tag{6.8}$$

where ψ_q is the quadratic phase factor

$$\psi_q(\rho) = Cxy + D_x x^2 + D_y y^2. \tag{6.9}$$

If the strong wavefront phase variation is caused by a quadratic phase factor, then the residual field $U(\rho)$ can be faithfully represented with relatively few sampling points as it will not oscillate as strongly.

After splitting the field into a residual and quadratic phase factor the field in the k-domain is given by the convolution

$$\widetilde{V}(\mathbf{k}) = \widetilde{U}(\mathbf{k}) \star \boldsymbol{\mathcal{F}}_k \left\{\exp(i\psi(\rho))\right\}(\mathbf{k}). \tag{6.10}$$

To simplify the term $\mathcal{F}\left\{\exp(i\psi(\rho))\right\}(\mathbf{k})$ the following analytical formula [2] can be used:

$$\int_{-\infty}^{\infty} \exp(-ax^2 + bx + c)dx = \sqrt{\frac{\pi}{a}} \exp\left(\frac{b^2}{4a} + c\right), \tag{6.11}$$

given that $a, b, c \in \mathbb{C}$, $\mathbb{R}\{a\} \geq 0$ and $a \neq 0$. As such the Fourier transform of the quadratic phase can be written in the form

$$\boldsymbol{\mathcal{F}}_k \left\{\exp(i\psi(\rho))\right\}(\mathbf{k}) = \frac{-i}{\sqrt{\gamma}} \exp(i\widetilde{\psi}(\mathbf{k})), \tag{6.12}$$

with

$$\widetilde{\psi}(\mathbf{k}) = -\frac{k_x^2}{D_x} - \frac{k_y^2}{D_y} + \frac{C^2}{4\gamma}\left[\frac{k_x^2}{D_x} + \frac{k_y^2}{D_y} - 4k_x k_y\right], \tag{6.13}$$

$$\gamma = C^2 - 4D_x D_y. \tag{6.14}$$

Inserting this into Eq. (6.10) and changing the order of integration gives

$$\begin{aligned}\widetilde{V}(\mathbf{k}) &= \frac{-i}{\sqrt{\gamma}} \int_{-\infty}^{\infty}\int \widetilde{U}(\mathbf{k}') \exp\left[i\widetilde{\psi}(\mathbf{k}' - \mathbf{k})\right] \mathrm{d}k_x' \mathrm{d}k_y' \\ &= \frac{-2\pi i}{\sqrt{\gamma}} \exp\left[i\widetilde{\psi}(\mathbf{k})\right] \widetilde{U}_\alpha(\mathbf{k}),\end{aligned} \tag{6.15}$$

with

$$\begin{aligned}\widetilde{U}_\alpha(\mathbf{k}) &= \boldsymbol{\mathcal{F}}_\alpha \left\{\widetilde{U}(\mathbf{k}) \exp\left[i\widetilde{\psi}(\mathbf{k})\right]\right\}. \\ &= \frac{1}{2\pi} \int_{-\infty}^{\infty}\int \widetilde{U}(\mathbf{k}') \exp\left[i\widetilde{\psi}(\mathbf{k}')\right] \\ &\quad \times \exp\left[i\left(\frac{2k_x}{D_x} + \frac{b^2}{\gamma}k_y\right)k_x' + i\left(\frac{2k_y}{D_y} + \frac{b^2}{\gamma}k_x\right)k_y'\right] \mathrm{d}k_x' \mathrm{d}k_y'.\end{aligned} \tag{6.16}$$

For larger values of C, D_x, D_y this Fourier transform followed by the appropriate coordinate transformation leads to a significant reduction in the number of sampling points required [57].

As an example, suppose a 1-D field component $V(x)$ that according to Eq. (6.8) can be decomposed into the residual field component $U(x) = \exp[-(ax)^2 + ik_0 bx^3]$ and quadratic phase factor $\psi_q(x) = k_0 Dx^2$, with $k_0 = 2\pi/\lambda$. Then for a large enough quadratic phase factor the real and imaginary parts of the field will start to oscillate as shown in Figure 6.2(a). For the chosen parameters the residual field requires much fewer sampling points to be accurately represented as shown in Figure 6.2(b). The quadratic phase factor D is stored as a single number and thus the quadratic phase requires no sampling. Using the 1-D equivalent of Eq. (6.12–6.16) yields the

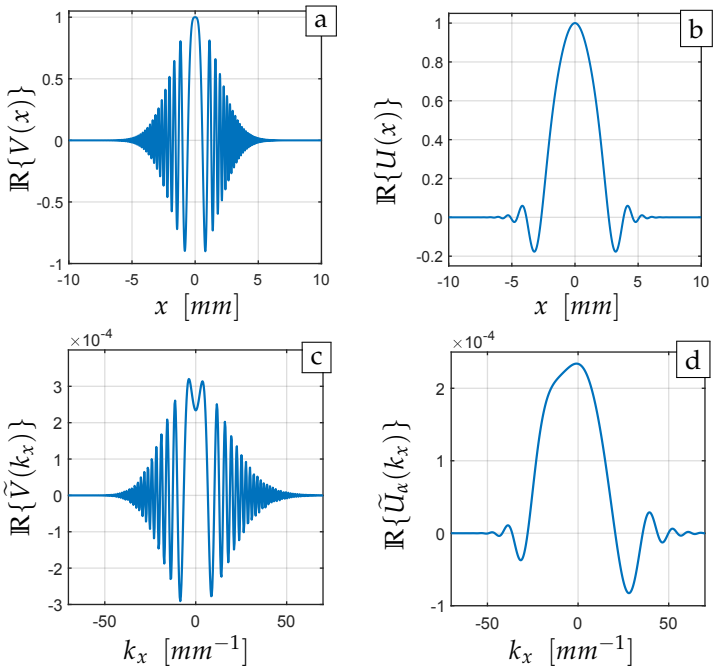

Figure 6.2: a) The real part of a field with a quadratic and cubic phase term. b) The real part of the residual field (field without the quadratic phase term) c) The Fourier transform of the full field and d) the residual field as obtained by the semi-analytical Fourier transform. Parameters used: $\lambda = 532$ nm, $a = 400$, $D = 0.4$ and $b = 7$.

residual field $\widetilde{U}_\alpha(k_x)$ shown in Figure 6.2(d) which can also be represented with fewer sampling points. From the 1-D equations one finds that $\widetilde{\psi}_q(k_x) = -k_x^2/(4D)$. Adding the quadratic phase factor to its corresponding residual field will yield the representation shown on the left of Figure 6.2 without error.

It should be noted that the spherical phase given by

$$\phi(\rho) = \exp\left[ikr\sqrt{(x/r)^2 + (y/r)^2 + 1}\right] \tag{6.17}$$

contains non-quadratic phase phase terms as well. For small values of r these non-quadratic terms become relevant as the residual field will contain all of them. If these terms are significant then the number of sampling points required for the residual field grows (greatly). Next section discusses the Geometric Fourier Transform (GFT), which deals with situations where the non-quadratic phase components are strong enough to warrant its use.

6.4 GEOMETRIC FOURIER TRANSFORM

When wanting to Fourier transform a field with significant non-quadratic phase terms the Geometric Fourier Transform (GFT) can be used to (greatly) reduce the computational cost [58].

As defined in Section 6.3 let $V(\rho) = V(\rho, \omega)$ denote the field component of

interest at plane z and frequency ω. This field can be decomposed as

$$V(\rho) = U(\rho)\exp[i\phi(\rho)], \tag{6.18}$$

where $U(\rho)$ is assumed to have at most weak wavefront phases while $\phi(\rho)$ consists of strong wavefront phases. For the GFT it is assumed that the wavefront $\phi(\rho)$ is smooth so that it can be accurately interpolated on a non-equidistant grid. It is also assumed that the derivative of the wavefront phase is a monotonically increasing/decreasing function on the computational domain so that the geometric mapping conditions that will be used are not violated. As such it is assumed that the field exhibits no caustic effects on the selected plane and that the linear and even order polynomials dominate the field curvature. The decomposition that is shown in Eq. (6.18) is general such that $U(\rho)$ and $\phi(\rho)$ can be chosen to satisfy the above requirements. Like with the semi-analytical Fourier transform the concept is do the Fourier transform without having to sample a (residual) field with strong wavefront factors.

The Fourier transform of Eq. (6.18) is given by

$$\widetilde{V}(\mathbf{k}) = \frac{1}{2\pi}\iint U(\rho)\exp\left\{i[\phi(\rho) - \mathbf{k}_\perp \cdot \rho]\right\}\mathrm{d}\rho, \tag{6.19}$$

with $\mathbf{k}_\perp = (k_x, k_y)$. As $\phi(\rho)$ is assumed to posses a 'large' gradient, the term $\exp\{i[\phi(\rho) - \mathbf{k}_\perp \cdot \rho]\}$ oscillates (rapidly) with respect to $U(\rho)$ aside of specific points. The points where the phase term is stationary (in both directions) are called the critical points and are given by

$$\nabla_\perp \phi(\rho) - \mathbf{k} = 0. \tag{6.20}$$

This equation links coordinates ρ and $\mathbf{k}$ together and can be thought of as a mapping operator. It is assumed that this mapping operator is bijective, open and continuous. This is to say that both spaces are homeomorphic; they contain the same topological features. Roughly put this means that one can go from one space to another by means of a geometric distortion, i.e. by streching/compressing and bending of the space. As $\mathbf{k}$ is a monotonic (increasing/decreasing) function, $\nabla_\perp \phi(\rho)$ must be as well. This requirement is fulfilled when the wavefront has at most a single minimum or maximum on the computation domain. Under these conditions the existence of the inverse mapping operator $\rho(\mathbf{k})$ is guaranteed.

Similar to the Laplace's method only a small region near the critical points will contribute to the integral [2]. If the field is nonzero at the edge of the domain then also the points on the edge of the domain can contribute to the integral. In this section these contributions are skipped as the considered fields have a finite extent and drop to zero at the edge of the computation domain.

Let $\rho(\mathbf{k}) = (x(\mathbf{k}), y(\mathbf{k}))$ be the critical point described by Eq. (6.20). In the neighborhood of this point the phase factor can be approximated as

$$\begin{aligned}\phi(\rho) - \mathbf{k}_\perp \cdot \rho \approx \phi(\rho(\mathbf{k})) - \mathbf{k}_\perp \cdot \rho(\mathbf{k}) + \frac{1}{2}(x - x(\mathbf{k}))^2 \phi_{xx}|_{\rho(\mathbf{k})} \\ + (x - x(\mathbf{k}))(y - y(\mathbf{k}))\phi_{xy} + \frac{1}{2}(y - y(\mathbf{k}))^2 \phi_{yy}|_{\rho(\mathbf{k})},\end{aligned} \tag{6.21}$$

with $\phi_{xy}|_{\rho(\mathbf{k})} = \partial^2\phi(\rho)/\partial x \partial y$ evaluated at $\rho(\mathbf{k})$ and similarly for ϕ_{xx} and ϕ_{yy}.

Substituting Eq. (6.21) into Eq. (6.19) under the stationary phase consideration results in

$$\begin{aligned}\widetilde{V}(\mathbf{k}) \approx & \frac{1}{2\pi} U(\rho(\mathbf{k})) \exp(i[\phi(\rho(\mathbf{k})) - \mathbf{k}_\perp \cdot \rho(\mathbf{k})]) \\ & \cdot \iint_{-\infty}^{\infty} \exp\left\{ i \left[\frac{1}{2}(x - x(\mathbf{k}))^2 \phi_{xx}|_{\rho(\mathbf{k})} + (x - x(\mathbf{k}))(y - y(\mathbf{k}))\phi_{xy} \right] \right\} \\ & \cdot \exp\left\{ i \frac{1}{2}(x - x(\mathbf{k}))^2 (y - y(\mathbf{k}))^2 \phi_{yy}|_{\rho(\mathbf{k})} \right\} \mathrm{d}x\mathrm{d}y,\end{aligned} \tag{6.22}$$

which is an integral over a quadratic exponential function of which the solution is known. This solution can be written as

$$\widetilde{V}(\mathbf{k}) \approx a(\mathbf{k}) \widetilde{A}(\mathbf{k}) \exp(i\widetilde{\phi}(\mathbf{k})), \tag{6.23}$$

with the functions

$$\widetilde{\phi}(\mathbf{k}) = \phi(\rho(\mathbf{k})) - \mathbf{k}_\perp \cdot \rho(\mathbf{k}), \tag{6.24}$$

$$\widetilde{A}(\mathbf{k}) = U(\rho(\mathbf{k})), \tag{6.25}$$

$$a(\mathbf{k}) = \frac{i\sigma(\mathbf{k})}{\Delta(\mathbf{k})}. \tag{6.26}$$

The factor $\sigma = -i$ if $\Delta < 0$ or otherwise $\sigma = \text{sign}\{\Sigma(\mathbf{k})\}$ if $\Delta(\mathbf{k}) > 0$. The functions $\Delta(\mathbf{k})$ and $\Sigma(\mathbf{k})$ are given by

$$\Delta(\mathbf{k}) = \phi_{xx}|_{\rho(\mathbf{k})} \phi_{yy}|_{\rho(\mathbf{k})} - \phi_{xy}^2|_{\rho(\mathbf{k})}, \tag{6.27}$$

$$\Sigma(\mathbf{k}) = \phi_{xx}|_{\rho(\mathbf{k})} + \phi_{yy}|_{\rho(\mathbf{k})}, \tag{6.28}$$

where it is required that $\Delta(\mathbf{k}) \neq 0$ and both functions are either positive or negative on the computation domain.

By sampling all critical points the stationary phase method ensures that the Geometric Fourier Transform (GFT) asymptotically approximates the Fourier transform so that the difference between exact vanishes rapidly when strong wavefront phase variations are present.

Under this condition the number of sampling points needed is greatly reduced as (the dense) equidistant sampling of the oscillating term $\exp(i\phi)$ is replaced by the non-equidistant sampling of the continuous phase function $\phi(\rho)$. Given the lack of strong wavefront curvature the function $U(\rho)$ and $\widetilde{A}(\mathbf{k})$ can be sampled with much fewer sampling points on an equidistant grid while the phase functions $\phi(\rho)$ and $\widetilde{\phi}(\mathbf{k})$ can be stored and acted upon separately from their respective partners until they are needed together.

Using a similar method as used for the Semi-analytical let us consider the 1-D field component $V(x)$ decomposed as $U(x) = \exp[-(ax)^2]$ and $\phi(x) = k_0(Dx^2 + bx^3)$. The values of b are chosen such that the cubic phase term alone would significantly oscillate the field while D is chosen large enough so that $\partial\phi/\partial x$ is a monotonic (increasing/decreasing) function on the computation domain. Such choices would lead to an undesirable high computation effort even for the Semi-analytical Fourier Transform. The real part of $V(x)$ shown in Figure 6.3(a) can be represented with much less computational effort by the separate residual component $U(x)$ shown in

Figure 6.3(b) and phase component $\phi(x)$ shown Figure 6.3(c). Inserting these into the 1-D equivalent of Eqs. (6.20)-(6.26) yields the residual field and phase function shown in Figure 6.3(e,f). Due to the coordinate transformation these functions live on a different (non-equidistant) grid. After putting them on the same grid the resulting function is compared against the direct (numerical) FT of the field in Figure 6.3(d). The difference between the result is negligible.

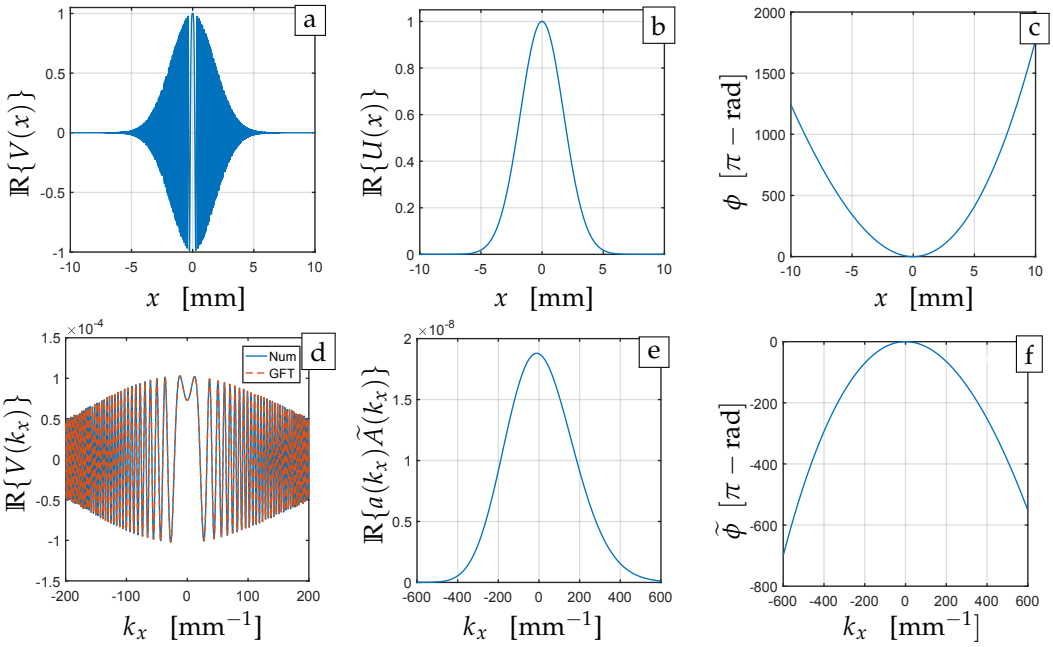

Figure 6.3: a) The real part of a field with a strong quadratic and cubic phase term, b) the residual field and c) the separated phase component. d) Direct FT and GFT compared where e) shows the residual field as obtained by GFT and f) the phase component as obtained by GFT. Parameters used: $\lambda = 532$ nm, $a = 400$, $D = 4$ and $b = 70$.

6.5 SURFACE MODELING

To determine the reflected and/or transmitted field at a given interface requires solving the EM-boundary conditions. In principle this could be done with rigorous solvers such as FMM or FTDT, but when a well defined wavefront and smooth surface is considered this can be done (with good accuracy) with a Local Plane Wave (LPWA), Local Plane Interface Approximation (LPIA).

The solution to a vectorial plane wave interacting with a plane interface is known explicitly in the form of Fresnel's reflection and transmission coefficients which can be applied with minimal computational effort. If a twice differential curved wavefront is considered, then the wavefront can be approximated as a patchwork of many (local) plane waves with finite area. This approximation of the wavefront is referred to as the Local Plane Waves Approximation (LPWA). Figure 6.4 depicts such a mesh that divides the smooth wavefront into many (triangle shaped) local plane waves. For a given mesh of plane waves at a plane interface one can obtain the reflected

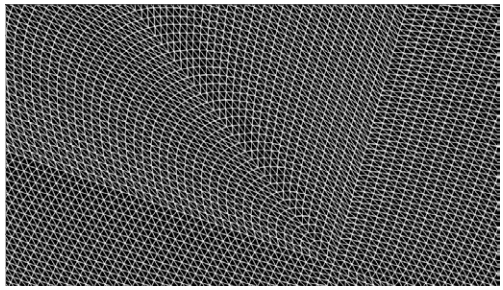

Figure 6.4: Mesh at a given plane that divides the wavefront into small area's. Each area represented by three adjacent grid points visualizes a local plane wave traveling along the normal of the wavefront at that location.

and/or transmitted field by applying the appropriate Fresnel coefficient to each plane wave at the surface of the interface.

If the (smooth) field interacts with a sufficiently smooth surface the same approximation can be applied to the surface in the form of a Local Plane Interface Approximation (LPIA) [59]. This requires that the smooth surface features are larger then the considered wavelength(s) such that diffraction/scattering effects at/near the surface can be safely neglected. As such the field interacting with the curved surface is locally described by a plane wave interacting with a plane interface. This is done by propagating the mesh to the surface of interest, apply the Fresnel coefficients to each plane wave interacting with their respective plane interface and propagating the result to a plane before/after the interface in order to reconstruct the reflected/transmitted field. This interaction requires a sufficiently fine mesh so that the optical response of the interface properly sampled [54, 60].

7 X-ray Field Tracing

7.1 X-RAY IMAGING SETUP

This chapter covers the X-ray imaging setup and the simulation results of said setup. The described setup and simulation results were implemented and obtained using Virtual Lab [61]. The setup in question consists of two grazing mirrors with figure errors that image a partially coherent Synchrotron Radiation (SR) source. A sketch of this setup is shown in Figure 7.1 with the field trace diagram shown earlier in Figure 6.1.

This section will describe the parameters used for the setup starting with the SR source parameters and followed by the mirror description.

7.1.1 Source

The source considered is a X-ray Synchrotron Radiation (SR) source as created by a Free-Electron Laser (FEL). In order to model the source accurately with the model described in Chapter 5 it needs to adhere to the assumptions made in that section.

To start, modern free-electron lasers provide short and intense photon pulses in the extreme ultraviolet and X-ray regime [62, 63]. It is mathematically possible for the spatial coherence properties to strongly fluctuate over the very short pulse duration. Given that no physical mechanisms are known that enable such a change in spatial coherence properties one could assume such variations do not occur. Therefore the narrow bandwidth and the high directionality properties of the FEL sources allows one to considered them to be quasi-monochromatic and paraxial. Furthermore the majority of FEL sources polarize the field linearly as it would require a special configuration to control polarization [65]. As such the use of a scalar MCF to represent the FEL is justified. Lastly the pulses were assumed to be quasi-stationary with respect to pulse duration, this would require the coherence time to be (much) shorter then the pulse duration. This is indeed the case for FEL sources [63, 64].

Under these considerations the SR source is assumed to be of GSM form such that it can be described by the shifted elementary mode representation given by section 5.4.2. To this purpose the (mean) wavelength $\lambda = 173$ pm (7.18 keV) and separable anisotropic Gaussian intensity profile is used for the rest of this chapter.

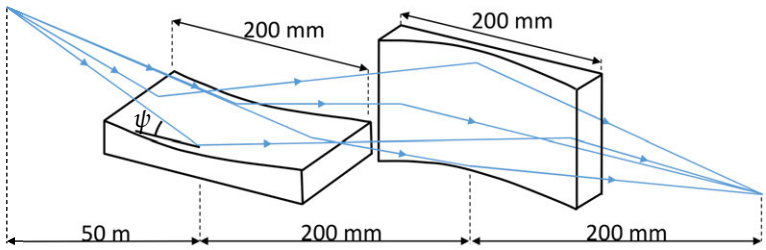

Figure 7.1: A sketch of the X-ray imaging setup, the grazing angle $\psi = 3$ mrad.

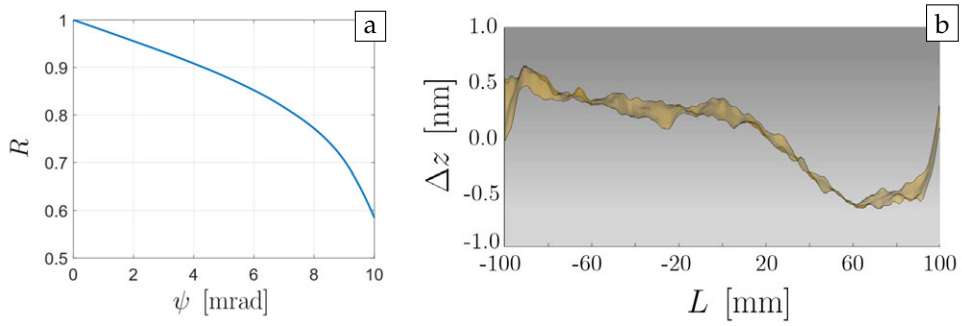

Figure 7.2: a) The reflectance coefficient of gold for TE-polarized plane wave as function of grazing angle (same curve for TM). b) Side view of the error map without mirror curvature.

The beam width at the source plane is taken to be $w_{0,H} = 22$ µm horizontally (H) and $w_{0,V} = 4.4$ µm vertically (V) while the far field beam divergence angle taken as $\theta_0 = 12.4$ µrad in both H and V direction. From Eq. (5.40) it follows that $\beta \approx 1 \times 0.2$ in (V×H) direction, i.e. the field is fully coherent vertically and partially coherent horizontally. The fully coherent field along the vertical direction is a simplification form the real world case as clarified in 7.3.

7.1.2 Mirrors

The considered mirrors are cylindrical grazing incidence mirrors also refereed to as Kirkpatrick-Baez (KB), this type of mirrors was first introduces to enable X-ray microscopy [66]. The grazing incidence refers to the very small angle between the mirrors surface and propagation direction of the light that is to be reflected off the mirrors. Figure 7.2(a) shows the reflectance coefficient for a plane wave falling on a gold coated plane surface as function of the grazing angle (angle between surface and propagation direction). For the setup considered a grazing $\psi = 3$ mrad is taken with the mirrors themselves being gold coated and elliptically shaped in one direction. Both have a length times width of 200×12 mm and are separated center to center by 200 mm. The source lies 50 m in front of the first mirrors center and the foci 200 mm after the second mirrors center, the foci of the elliptical shape of both mirrors is taken to coincide with the source and focal plane as shown in Figure 7.1.

For the simulation also the figure errors on the mirrors are taken into account. This error map was provided by Brookhaven National Laboratory of which a side view is shown in Figure 7.2(b).

Spot size

When using ideal mirrors one expects that the system focal spot size is given by the Rayleighs spot size:

$$\delta x = \frac{\lambda F}{D}, \tag{7.1}$$

where D describes the (effective) aperture size of the KB mirrors. By rough approximation this aperture size depends on the incident angle and length of the mirrors as

$$D \approx L \sin \psi, \tag{7.2}$$

and would result in an effective aperture of $D \approx 600 \times 600\mu$m. The more accurate equation presented in Appendix D shows that this description goes awry when angles become small and the edges of the mirror sufficiently large. To more accurately determine the spot size one needs to know the height of the side edges of both mirrors. For the setup of interest these are $\Delta h_1 = 30$ μm, $\Delta h_2 = 52$ μm for the horizontal mirror and $\Delta h_1 = 17$ μm, $\Delta h_2 = 22$ μm for the vertical mirror.

Plugging the edge height and focal length, F = 400, 200 mm (H,V), Eq. (D.13) yields an effective aperture size of $D = 716 \times 624$ μm for the horizontal and vertical mirror respectively. This results (for a wavelength of $\lambda = 0.173$ nm) in an expected focal spot size of 48.3×111 nm (H,V), which is a bit smaller then the 57.7×115 nm (H,V) if the aperture size simple approximation is used.

Strehl ratio

For an ideal mirror the outgoing wavefront should form a (truncated) sphere, if any errors are present on the mirrors surface a deviation in this wavefront will occur, i.e. wavefront aberrations. For a mirror with grazing angle ψ and height error $h(x)$ the induced wavefront aberration $W(x)$ is

$$W(x) = 2h(x) \sin \psi. \tag{7.3}$$

when assuming planar incidence.

The Strehl ratio indicates how strongly the wavefront aberrations affect the focal spot by comparing the real peak intensity (with aberrations) to the ideal peak intensity (no aberrations) at the focal plane:

$$D_s = \frac{I_{\text{PSF}}^{(\text{real})}(0,0)}{I_{\text{PSF}}^{(\text{ideal})}(0,0)}. \tag{7.4}$$

The Strehl ratio is a single value bound to $0 \leq D_s \leq 1$, with 1 indicating an ideal optical system. If the Strehl ratio is $D_s > 0.8$ the system is said to be diffraction limited. A diffraction limited system has its focal spot for the most part limited by diffraction and thereby produces a spot size close to the Rayleigh spot size. To see how much aberration is allowed to affect the wavefront before the system is no longer diffraction limited two common criteria are used: the Rayleigh and Marechal criteria.

The Rayleigh criterion requires the wavefront aberrations to be small enough so that destructive interference is avoided, i.e. peak to valley wavefront aberrations are smaller than a quarter of the wavelength ($W_{\text{PV}} < \lambda/4$). It should be noted that this criterion was specified by assuming that only spherical aberrations are present. From Eq. (7.3) it follows that the peak valley height error should uphold $h_{\text{PV}} < \lambda/(8 \sin \psi) \approx 4.2$ nm.

When all aberration types are present the Marechal criterion gives a more accurate estimation. This states that the system is diffraction limited if the root mean square wavefront error upholds $W_{\text{RMS}} < \lambda/14$, i.e. $h_{\text{RMS}} < \lambda/(28 \sin \psi) \approx 1.2$ nm.

The error map shown in Figure 7.2 has an peak valley height error of $h_{\text{PV}} \approx 1.24$ nm and RMS height error of $h_{\text{RMS}} \approx 0.38$ nm. Both of them are more than a factor three below the Rayleigh and Marechal criterion respectively, as such the system should be diffraction limited. From this it is also expected that exaggerating the errors by a factor 5 will cause the optical system to no longer be diffraction limited. The results part of this chapter covers both situations.

7.2 SIMULATION RESULTS

7.2.1 Coherent source results

The ideal mirrors with a coherent Gaussian source use the parameters $\lambda = 173$ pm (7.18 keV), $w_0 = 4.4$ µm in both horizontal and vertical directions. The coherent source with ideal mirrors will be taken as reference, as such all indicated intensities in this chapter are normalized with respect to the found peak intensity for the ideal case. The 2-D intensity profile at the focal plane when using ideal mirrors and aberrated mirrors is shown in Figure 7.3 together with the profile obtained when the error-map illustrated in Figure 7.2(b) is taken into account.

As indicated by the normalized intensity the Strehl ratio of the mirror system with aberrated mirrors is $D_s \approx 0.98$. As such the mirrors are well diffraction limited.

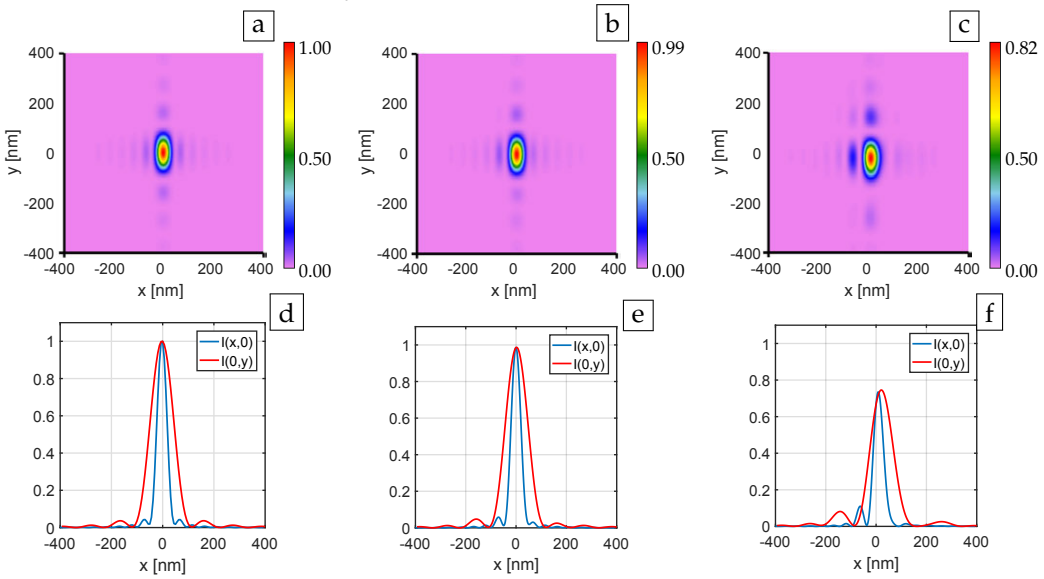

Figure 7.3: Coherent field, a) the 2-D and d) 1-D focal spot when using ideal mirrors along with b) the 2-D and e) 1-D focal spot when using abberated mirrors. In c) and f) the error map was increased by a factor 5.

Increasing the errors given by the error map by a factor 5 results in Figure 7.3(c,d). In Figure 7.3(f) the 1D cross-section no longer goes through the peak intensity as the tip and tilt error become significant. While the peak intensity is 0.83 of the ideal intensity, the Strehl ratio is defined on the center and thereby is only $D_s \approx 0.75$. This is in good agreement with the Rayleigh and Marechal criteria.

In Figure 7.3(b) the Rayleigh spot size is $x = 50.5 \pm 0.5$ nm and $y = 116 \pm 0.5$ nm (H,V), which is a bit larger than the 48.3×111 nm (H,V) expected Rayleigh spot size. As illustrated in Figure 7.4 the found effective aperture size matches the calculated one but the assumption of a uniform intensity is not upheld. This deviation is attributed to the Gaussian shape of the source profile and angular dependence of the Fresnel coefficients.

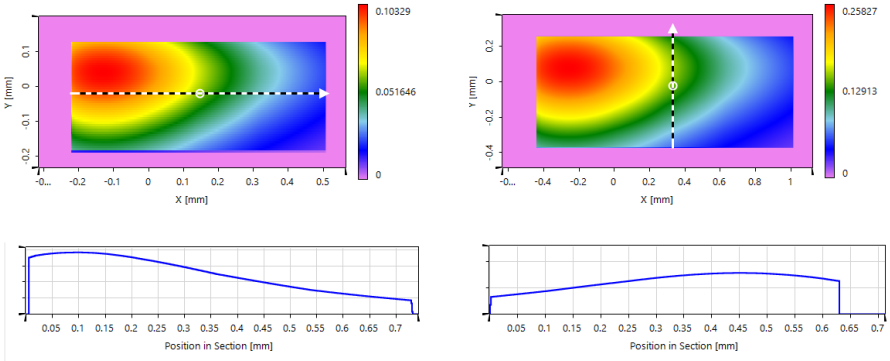

Figure 7.4: The field intensity at $F = 200$ mm (left) and $F = 400$ mm (right) after the focal plane. The found effective aperture is $717 \times 624 \pm 1$ µm at $F = 200, 400$ (H,V) respectively. The cross-sections show that the illumination across this aperture deviates from uniform illumination.

7.2.2 Incoherent source results

For this section the partially coherent source description given by Eq. (5.57) with source parameters given in Section 7.1.1 are used. In this description $N = 17$ elementary modes starting from location $v_{x,1} = -1.4w_\mathrm{p}$, $w_\mathrm{p} \approx 21.5$ µm and spaced by a distance $\Delta v_x = 2.8w_\mathrm{p}/(N-1)$ were sufficient. For ideal mirrors the 1-D and 2-D intensity distribution at the focal plane in given in Figure 7.5. The figure also depicts the cross-section of all elementary modes along with the field amplitudes of elementary modes number e_7, e_9 and e_{11}.

In Figure 7.5(c-e) the shape of adjacent elementary modes gradually change as a function of position, showing that the aplanatic region has a similar extent as the spacing of the modes. As such increasing the number of modes showed no change in the resulting focal spot.

As the aberrations on the fabricated mirror are very small the resulting figure would be nearly identical to that of the ideal mirrors. As such this figure is omitted and a $5\times$ increased error map is plotted instead in Figure 7.6.

Comparing the elementary modes of the $5\times$-aberrated mirrors shown in Figure 7.6(c) with the ideal mirror case (Figure 7.5(c)) shows a significant change in the side-lobes. This has however made little change to the focal spot along the x-direction as these contributions are averaged out when summed. Due to this summing the tilt aberration has shifted the maximum amplitude a longer distance in y-direction than in x-direction. As such the amplitudes of the cross-sections in Figure 7.6(c) are no longer the same.

Figure 7.7 illustrates the resulting CSD and MCF at the source plane along with the CSD and MCF at the image plane when no mirror aberrations are present or when the $5\times$ measured error map is used. For the image plane figures, the line pattern around the central lobe comes from the side-lobes of the elementary modes at the focal plane shown in Figure 7.5(c). In MCF figures the width of the diagonal in $\mu(x_1, x_2)$ determines the coherence width at the diagonal. For Shell model sources this width should stay constant along the diagonal as can be seen at the source plane. At the image plane the coherence width is roughly constant at the region of

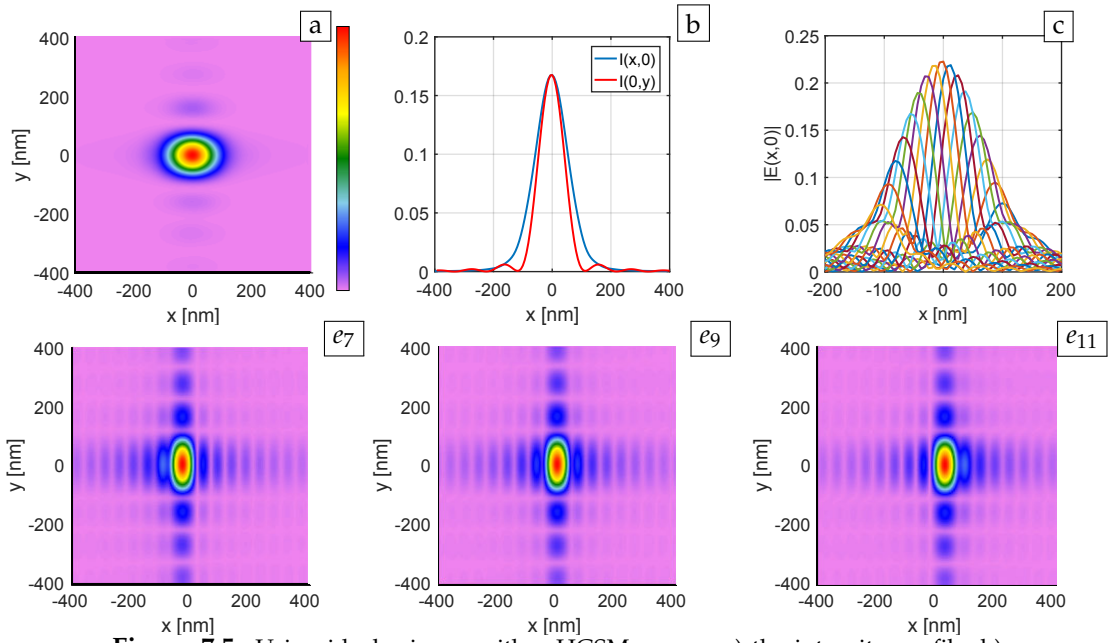

Figure 7.5: Using ideal mirrors with a HGSM source, a) the intensity profile, b) its cross-section at the focal plane and c) the x-cross-section of all elementary mode field amplitudes. The 2-D cross-section shown in the bottom half of this figure depict elementary modes 7, 9 and 11.

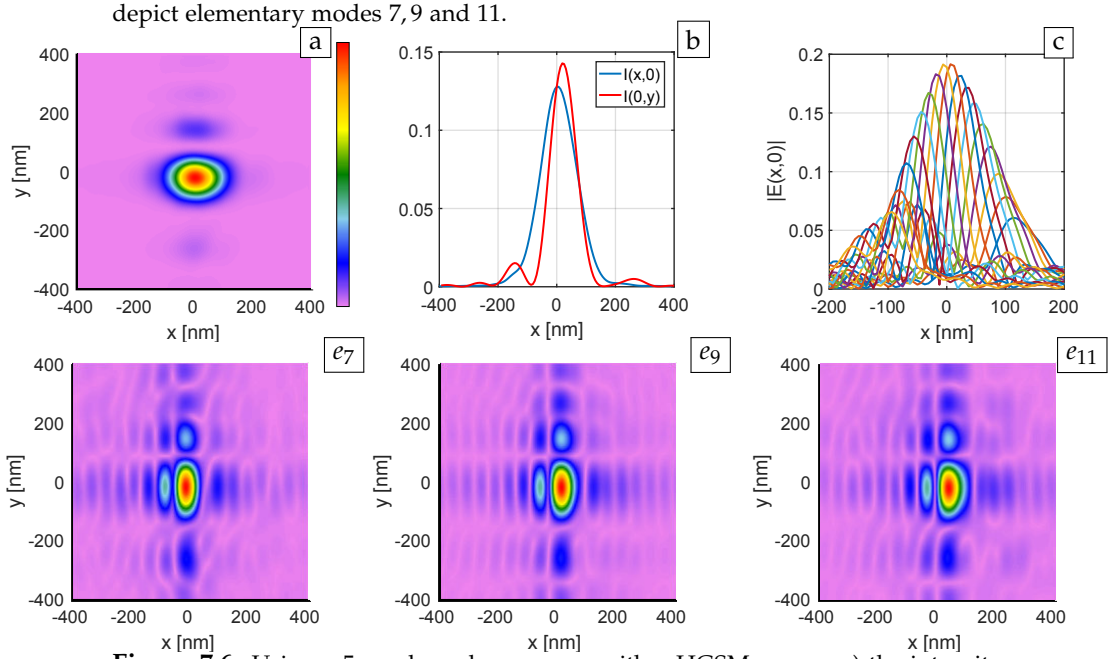

Figure 7.6: Using a 5× enlarged error-map with a HGSM source, a) the intensity profile, b) its cross-section at the focal plane and c) the x-cross-section of all elementary mode field amplitudes. The 2-D cross-section shown in the bottom half of this figure depict elementary modes 7, 9 and 11.

high intensity and grows in width towards the edges of the diagonal. As such the field at the image plane is only approximately of the Shell-model form.

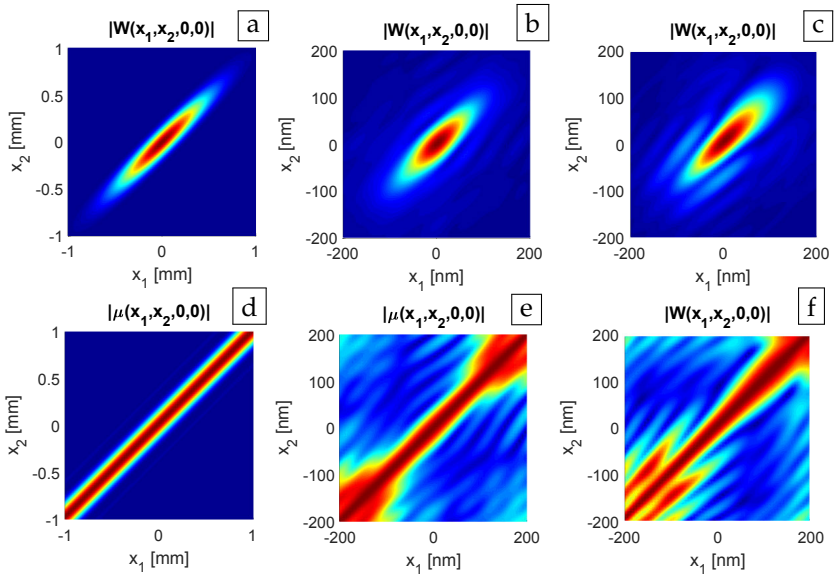

Figure 7.7: The CSD (top) and MCF (bottom) at a,d) the source, at the focal plane if using b,e) ideal mirrors (middle) or c,f) 5× error map.

7.3 OUTLOOK

For sake of argumentation suppose an FEL source with a beam width of $w_0 = 22.0 \times 548$ µm and a divergence angle of $\theta_0 = 12.4 \times 24.8$ µrad in (x, y) direction.

The focal spot of such a source would be very large in y-direction and destroy any imaging capabilities with it. To avoid this fate an additional mirror and aperture are used in the configuration given by Figure 7.8.

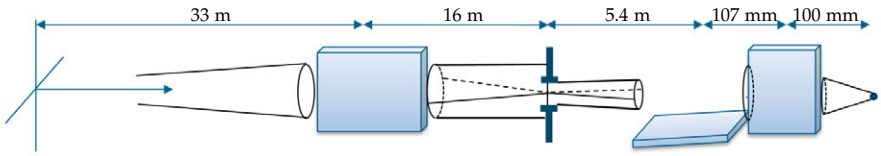

Figure 7.8: Setup taken from [67]. The coherence of the FEL source is significantly increased by focusing the most coherent direction (here x-axis) onto an aperture before using two focal mirrors to create a focal spot.

The additional mirror focuses in the x-direction, causing most of the partially coherent field to go through and only a small fraction of the strongly incoherent field. The limited extent of the elementary modes allows this computation to be done with a small fraction of the total amount of modes. For the considered source $\beta \approx 0.2 \times 0.004$ (H,V) so that about 17×1200 modes are needed for accurate rep-

resentation. One would for instance need about 17×45 elementary modes if the aperture is placed 49 m from the source and has a square aperture opening of 50×50 μm. In this estimation any mode that does not have its center outside the aperture area by 2 times the elementary mode's width w_e was counted.

To perform this simulation with the methods described at the start of this chapter would require that one can change the representation of the field directly after the aperture. At that point the field was given in terms of amplitude with a relatively strong numerical phase. As such one would ideally use the semi-analytical Fourier transform or Geometric Fourier transform to propagate the field with minimal effort. Both these methods would require that the strong phase terms can be separated out from the numerical data, which in turn requires that the wavefront can be determined/unwrapped and the analytical/strong phase factors subtracted from it. While possible as amplitude and phase are well sampled, this is out of scope of this thesis. This meant that the rest of the computation would be limited by having to include this strong phase in all computations that followed and thereby could not be computed on the available computer hardware. As such this task is put forth as an outlook.

8 Discussion and Conclusions

In this thesis the mathematical concept of Signal Relevant Efficiency (SRE) and scalar diffraction theory were presented. Spatial coherence theory and field propagation have also been discussed in detail and used to simulate an X-ray beamline.

In Chapter 2 the concept of SRE has been reformulated into a notation that is more easy to apply and understand. The resulting SRE description was applied to the Iterative Fourier Transform Algorithm in Chapter 3 in order to improve its performance when designing gratings made of lossy material. By applying the SRE to scalar diffraction theory clear theoretical insights emerged in Chapter 4 that explained which grating profile shapes are preferential. As a direct consequence the grating profiles that maximize any single or two diffraction order efficiencies under any phase-amplitude constraint can now be directly obtained from this theorem.

The analytical expression for the grating profile that creates three equal diffraction orders was derived for lossy media and shown in Appendix B. This result was used in Chapter 4 as a reference to test the extended design algorithm against. In this is was found that the made alterations significantly improve the designs algorithm's performance. The design algorithm was applied to design the grating spacings for V-shaped microstructure such that it produced three, five or eight equal diffraction orders. As discussed in [34] the fabricated V-shape microstructures maintain good performance over a broad wavelength and angular range.

The Gaussian Shell Model (GSM) theory was presented in Chapter 5 along with reasoning when and why this description can be applied to the source description of Free-electron lasers used in X-ray experiments. As part of this the elementary field representation was derived from the Hermite Gaussian Shell Model description in Appendix C, yielding a relation connection between their weights.

The elementary mode description of Chapter 5 was used in combination with the field propagation methods explained in Chapter 6 to simulate an X-ray beamline system described in Chapter 7. In this it was found that the focal spot is smaller than expected, the cause of this is the elliptical geometry of the mirrors combined with the very small grazing angles of the X-rays as detailed in Appendix D. The resulting simulation results agree with aberration theory and show that the measured mirror error-maps leave the system nicely diffraction limited. The modeling method should be extended in the future so that the full system with aperture can be modeled as well. It would also be useful to look into how alignment errors (position and rotation) affect the performance of these systems so that placement accuracy can be taken into account when building them.

BIBLIOGRAPHY

[1] H. Aagedal, "Simulation und Design paraxialer diffraktiver Systeme," Ph.D. thesis (Universität Karlsruhe, 1998).

[2] L. Mandel and E. Wolf, *Optical Coherence and Quantum Optics* (Cambridge University Press, Cambridge, 1995).

[3] S. A. Collins, Jr., "Lens-system diffraction integral written in terms of matrix optics," J. Opt. Soc. Am. 60, 1168–1177 (1970).

[4] P. R. Halmos, *A Hilbert Space Problem Book* (Springer-Verlag, New York, 1974).

[5] J.W. Goodman, *Introduction to Fourier Optics* (McGraw-Hill, New York, 1968).

[6] R. W. Gerchberg and W. O. Saxton, "A practical algorithm for the determination of phase from image and diffraction plane structures," Optik 35, 237–246 (1971).

[7] D. P. Feder, "Automatic Optical Design," Appl. Opt. **2**, 1209- 1226 (1963).

[8] J. R. Fienup, "Phase retrieval algorithms: a comparison," Appl. Opt. **21**, 2758-2769 (1982).

[9] H. Schwefel, *Evolution and Optimum Seeking* (Wiley, New York, 1995)

[10] R. Hauck and O. Bryngdahl, "Computer-generated holograms with pulse-density modulation," J. Opt. Soc. Am. A **1**, 5-10 (1984).

[11] K. Heggarty and R. Chevallier, "Signal window minimum average error algorithm for computer-generated holograms," J. Opt. Soc. Am. A 15, 625-635 (1998).

[12] J. Turunen, and F. Wyrowski, eds. *Diffractive Optics for Industrial and Commercial Applications* (Wiley-VCH, 1997).

[13] C. Rydberg, J. Bengtsson, and T. Sandstrom, "Performance of diffractive optical elements for homogenizing partially coherent light", J. Opt. Soc. Am. A. **24**, 3069-3079 (2007).

[14] M. G. Moharam and T. K. Gaylord, "Rigorous coupled-wave analysis of planar-grating diffraction," J. Opt. Soc. Am. **71**, 811–818 (1981).

[15] L. Li, "Fourier modal method for crossed anisotropic gratings with arbitrary permittivity and permeability tensors," J. Opt. A: Pure Appl. Opt. **5**, 345–355 (2003).

[16] B. Lee, H. Kim, and J. Park, *Fourier Modal Method and Its Applications in Computational Nanophotonics* (CRC Press, Boca Raton, 2012).

[17] L. Li. *Fourier Modal Method* E. Popov, ed. Gratings: Theory and Numeric Applications, SecondRevisited Edition, (Aix Marseille Université, CNRS, Centrale Marseille, Institut Fresnel, 13.1–13.40,2014)

[18] H. Ichikawa, "Electromagnetics analysis of diffraction gratings by the finite-difference time domain method," J. Opt. Soc. Am. A **15**, 152–157 (1998).

[19] T. Delort and D. Maystre, "Finite-element method for gratings," J. Opt. Soc. Am. A **10**, 2592–2601 (1993).

[20] P. Vincent, "Differential methods," in *Electromagnetic Theory of Gratings*, R. Petit, ed. (Springer-Verlag, Berlin, 1980), 101–121.

[21] B. Kleeman, A. Mitreiter, and F.Wyrowski, "Integral equation method with parametrization of grating profile," J. Mod. Opt **43**, 1323–1349 (1996).

[22] J. W. Goodman, and A. M. Silvestri, "Some effects of Fourier domain phase quantization," IBM J. Res. Dev. **14**, 478–484 (1970).

[23] F. Gori, M. Santarsiero, S. Vicalvi, R. Borghi, G. Cincotti, E. Di Fabrizio, and M. Gentili, "Analytical derivation of the optimum triplicator," Opt. Commun. **157**, 13–16 (1998).

[24] J. Ge, D. McDavitt, J. Bernecker, S. Millerand, D. Cairlo, and P. Kuzmenko, "Development of silicon grisms and immersions gratings for high resolution infrared spectroscopy," Proc. SPIE **4485**, 393–404 (2002).

[25] L. Escoubas, J. J. Simon, M. Loli, G. Berginc, F. Flory, and H. Giovannini, "An antireflective silicon grating working in the resonance domain for the near infrared spectral region," Opt. Commun. **226**, 81–88 (2003).

[26] N. Rajkumar and J. N. McMullin, "V-groove gratings on silicon for infrared beam splitting," Appl. Opt. **34**, 2556–2559 (1995).

[27] J. Turunen and E. Noponen, "V-groove gratings on silicon for infrared beam splitting: comment," Appl. Opt. **35**, 807–808 (1996).

[28] A. Brockmeier, F. J. S. Rodriguez, M. Harrison, and U. Hilleringmann, "Surface tension and its role for vertical wet etching of silicon," J. Micromech. Microeng. **22**, 125012 (2012).

[29] A. W. Lohmann, and D. P. Paris, "Binary Fraunhofer holograms, generated by computer," Appl. Opt. **6**, 1739–48 (1967).

[30] H. Haidner, J. T. Sheridan, and N. Streibl, 'Design of blazed grating consisting of metallic subwavelength binary grooves,' Opt. Commun. 98, 5–10 (1993).

[31] E. Noponen and J. Turunen, "Complex-amplitude modulation by high carrier-frequency diffractive elements," J. Opt. Soc. Am. A **13**, 1422–1428 (1996).

[32] W. Stork, N. Streibl, H. Haidner, and P. Kipfer, "Artificial distributed-index media fabricated by zero-order gratings," Opt. Lett. **16**, 1921–1923 (1991).

[33] R. Petit, ed., *Electromagnetic Theory of Gratings* (Springer,Berlin, 1980).

[34] G. Bose, *Diffractive optics based on V-shaped structures and its applications*, (Dissertation in Forsestry and Natural Sciences, University of Eastern Finland, 2016).

[35] G. Bose, A.D. Verhoeven, I. Vartiainen, M. Roussey, M. Kuittinen, J. Tervo and J. Turunen, 'Diffractive optics based on modulated subwavelength-domain V-ridge gratigns,' J. Opt. **18**, 085602 (2016).

[36] A. C. Schell, 'A technique for the determination of the radiation pattern of a partially coherent source,' IEEE Trans. Antennas Propag. AP **15**, 187–188 (1967).

[37] F. Gori and C. Palma, 'Partially coherent sources which give rise to highly directional fields,' Opt. Commun. **27**, 185–187 (1978).

[38] P. Vahimaa and J. Turunen, 'Finite elementary source model for partially coherent radiation,' Opt. Express **14**, 1376–1381 (2006).

[39] J. Tervo, J. Turunen, P. Vahimaa, and F. Wyrowski, 'Shifted elementary mode representation for partially coherent vectorial fields,' J. Opt. Soc. Am. A **27**, 2004–2014 (2010).

[40] J. Turunen, 'Elementary-field representations in partially coherent optics,' J. Mod. Opt. **58**, 509–527 (2011).

[41] A. T. Friberg and R. J. Sudol, 'Propagation parameters of gaussian Schell-model beams,' Optics Commun. **41**, 383–387 (1982).

[42] F. Gori, 'Matrix treatment for partially polarized, partially coherent beams' Opt. Lett. **23**, 241–243 (1998).

[43] F. Gori, and M. Santarsiero, 'Devising genuine spatial correlation functions,' Opt. Lett. **32**, 3531–3533 (2007).

[44] J. Tervo, T. Setälä, and A. T. Friberg, 'Theory of partially coherent electromagnetic fields in the spacefrequency domain,' J. Opt. Soc. Am. A **21**, 2205–2215 (2004).

[45] A. C. Schell, 'A technique for the determination of the radiation pattern of a partially coherent source,' IEEE Trans. Antennas Propag. **15**, 187–188 (1967).

[46] F. Gori, 'ColletWolf sources and multimode lasers,' Optics Communnications **32**, 301–305 (1980).

[47] S. Saitoh, *Integral Transforms, Reproducing Kernels and their Applications*, Pitman Research Notes in Mathematics Series, Addison Wesley Longman, UK369 (1997).

[48] R. Martínez-Herrero, P.M. Mejías, and F. Gori, 'Genuine cross–spectral densities and pseudo-modal expansions', Opt. Lett.**34**, 1399–1401 (2009).

[49] S. Matsuyama, H. Mimura and H. Yumoto, "Diffraction-limited two-dimensional hard-x-ray focusing at the 100 nm level using a Kirkpatrick-Baez mirror arrangement" Am. Institute of Physics **76**, 083114 (2005).

[50] C. Morawe and M. Osterhoff, "Hard X-Ray Focusing with Curved Refective Multilayers" X-ray Optics and Instrumentation **2010**, 479631 (2010).

[51] N. Canestrari, O. Chubar, and R. Reininger, 'Partially coherent x-ray wavefront propagaion simulation including grazing incidence focusing optics', J. Synchrotron Rad. **21** 1110-1121 (2014).

[52] X. Shi, R. Reininger, M. S. del Rio and L. Assoufid, "A hybrid method for X-ray optics simulation: combining geometric ray-tracing and wavefront propagation" J. Synchrotron Rad. **21** 669-678 (2014).

[53] E.O. Brigham, *The Fast Fourier Transform* (Prentice-Hall: Englewood Cliffs, 1974).

[54] F. Wyrowski and M. Kuhn, 'Introduction to field tracing,' J. Mod. Opt. **58**, 449–466 (2011).

[55] S. Zhang, D. Asoubar, C. Hellmann, and F. Wyrowski, 'Propagation of electromagnetic fields between non-parellel planes: a fully vectorial formulation and an efficient implementation', Appl. Opt. **55**, 529–538 (2016).

[56] J. A. C. Veerman, J. J. Rusch, and H. P. Urbach, 'Calculation of the Rayleigh-Sommerfeld diffraction integral by exact integration of the fast oscillating factor', J. Opt. Soc. Am. A. **22**, 636-646 (2005).

[57] Z. Wang, S. Zhang, and F. Wyrowski, 'The Semi-analytical Fast Fourier Transform', in *Proc. DGaO* **118**, P2 (2017).

[58] F. Wyrowski and C. Hellmann, 'The Geometric Fourier Transform', in *Proc. DGaO* **118**, P37 (2017).

[59] A. Pfeil, and F. Wyrowski, 'Wave-optical structure design with the local planeinterface approximation', Opt J. Mod. Optics **47**, 2335–2350 (2000).

[60] F. Wyrowski, 'Unification of the geometric and diffractive theories of electrodynamic fields', in *Proc. DGaO* **118**, A36 (2017).

[61] *Wyrowski VirtualLab Fusion*, LightTrans GmbH, Jena, Germany.

[62] W. Ackermann, G. Asova, V. Ayvazyan, A. Azima, N. Baboi J. Bahr, V. Balandin, et al., ' Operation of a free-electron laser from the extreme ultraviolet to the water window.' Nature Photonics **1**, 336–342 (2007).

[63] P. Emma, R. Akre, J. Arthur, R. Bionta, C. Bostedt, J. Bozek A. Brachmann, et al., 'First lasing and operation of an angstrom-wavelength free-electron laser', Nature Photonics **4**, 641–647 (2010).

[64] S. Roling, B. Siemer, M. Wostmann, H. Zacharias, R. Mitzner, A. Singer, K. Tiedtke, et al. 'Temporal and spatial coherence properties of free-electron-laser pulses in the extreme ultraviolet regime', Phys. Rev. ST Accel. Beams **14**, 080701 (2011).

[65] E. Ferrari, E. Allaria, J. Buck, G. De Ninno, B. Diviacco, D. Gauthier L. Giannessi, et al. ' Single shot polarization characterization of XUV FEL pulses from corssed polarized undulators', Scientific Reports **5**, 13531 (2015).

[66] P. Kirkpatric, and A.V. Baez, 'Formation of optical images by x-rays', J. Opt. Soc. Am. **38**, 766 (1948).

[67] De Andrade, V., Thieme, J., Chubar, O. and Idir, M. (2011). Proc. SPIE, 8141, 81410L.

[68] F. Gori, M. Santarsiero, S. Vicalvi, R. Borghi, G. Cincotti, E. Di Fabrizio, and M. Gentili, 'Analytical derivation of the optimum triplicator,' Opt. Commun. **157**, 13–16 (1998).

[69] S. Saitoh, *Integral Transforms, Reproducing Kernels and their Applications*,Pit-man Research Notes in Mathematics Series, Addison Wesley Longman, UK369 (1997).

[70] F. Gori, and M. Santarsiero, 'Devising genuine spatial correlation functions,' Opt. Lett **32**, 3531–3533 (2007).

[71] R. Martínez-Herrero, P.M. Mejías, and F. Gori, 'Genuine cross-spectral densities and pseudo-modal expansions', Opt. Lett.**34**, 1399-1401 (2009).

[72] Digital Library of Mathmatical Functions: `https://dlmf.nist.gov/18.10`.

[73] S. Matsuyama, H. Mimura, H. Yumoto, K. Yamamura, Y. Sano, K. Endo, Y. Mori, et. al., 'Diffraction-limited two-dimensional hard-x-ray focusing at the level using a Kirkpatrick-Baez mirror arrangement', Rev. Sci. Instrum. **76**, 083114 (2005).

[74] C. Morawe, and M. Osterhoff, 'Hard X-Ray Focusing with Curved Reflective Multilayers', X-ray optics and Instrumentation **2010**, 479631 (2010).

A Projection A_c maximizing SRE

In this appendix the projection operator that projects the transmittance function onto constraint A_c for a given absorption level $\kappa/\Delta n$ and maximizes SRE is determined. The constraint to which the transmittance values are limited to is given by

$$A_c(\phi) = \exp[(i - \kappa/\Delta n)\phi], \tag{A.1}$$

where $\phi \in [0, 2\pi)$. Suppose the transmission function to be projected consists of a distribution of angles $\theta \in [0, 2\pi)$ and some amplitude $|A|$. Then to maximize SRE the projection one should minimize

$$\mathbf{t}_{\text{opt}} = \underset{t \in A_c}{\operatorname{argmin}} \lim_{r \to \infty} ||\mathbf{t} - r|A|\exp[i\theta]||^2, \tag{A.2}$$

where $\mathbf{t}_{\text{opt}}$ denotes the transmittance function obtained from projecting onto A_c. As $r \to \infty$ the amplitude of the to be projected function $|A|$ can be ignored and only a distribution of angles at infinity needs to be considered.

The constraint of Eq. (A.1) has its shortest projection path along its normal, which at angle ϕ goes out under the angle

$$\phi = \theta - \arctan(\kappa/\Delta n). \tag{A.3}$$

Hence for the continuous part of the constraint, this would be the resulting phase value when trying to project angle θ onto A_c.

As ϕ is discontinuous at $\phi = 0$ and $\phi = 2\pi$ the edge cases should be handled separately. To this point the constraint of Eq. (A.1) is written in Cartesian coordinates as

$$x(\phi) = \mathbb{R}\{A_c(\phi)\} = \exp[-(\kappa/\Delta n)\phi]\cos\phi \tag{A.4}$$
$$y(\phi) = \mathbb{I}\{A_c(\phi)\} = \exp[-(\kappa/\Delta n)\phi]\sin\phi \tag{A.5}$$

so that at $\phi = 0$ the normal is given by

$$\theta_0 = \arctan\left[-\frac{x(0)}{y(0)}\right] = \arctan(\kappa/\Delta n). \tag{A.6}$$

In this edge case the angles under $0 \leq \theta < \theta_0$ should be projected to $\phi = 0$.

For the second edge case the illustration in Figure A.1 is used, which shows a tangential line that goes trough points $A_c(\phi_M)$ and $A_c(0)$. The two lines that lie perpendicular to this tangential line go out under angle $\theta_M = \phi_M + \arctan(\kappa/\Delta n)$ and indicate that for the angles $\theta_M < \theta < 2\pi$ lie closer to $A_c(0)$ than any other point on A_c.

Hence if ϕ_M is known, any value $\lim_{r \to \infty} r\exp(i\theta)$ should be projected onto A_c as

$$\phi_{\text{proj}} = \begin{cases} \theta - \arctan(\kappa/\Delta n) & \text{if } 0 \leq \theta - \arctan(\kappa/\Delta n) \leq \theta_{\text{M}} \\ 0 & \text{otherwise.} \end{cases} \tag{A.7}$$

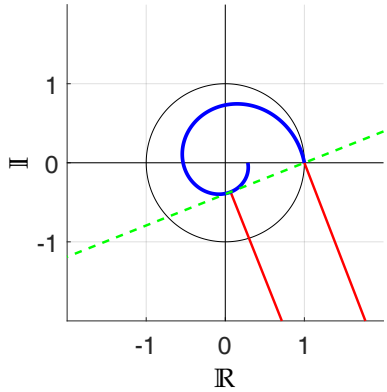

Figure A.1: The inward spiral depicts A_c given by Eq. (A.3) for $\kappa/\Delta n = 0.2$. The tangent to A_c is shown as the dashed line that also goes through the points $A_c(\phi_M)$ and $A_c(0)$. The two lines that originate out of these two points represent the normal of the tangent.

To find ϕ_M the tangent has to be defined. It is known that the tangent runs through $(x, y) = (x(\phi_M), y(\phi_M))$ and $(x, y) = (1, 0)$ so that it is defined by

$$t \left.\frac{\mathrm{d}x}{d\phi}\right|_{\phi_M} + x(\phi_M) = x(0), \tag{A.8}$$

$$t \left.\frac{\mathrm{d}y}{d\phi}\right|_{\phi_M} + y(\phi_M) = y(0), \tag{A.9}$$

where t is a running parameter. Combining these equations for the tangent with Eq. (A.5) yields

$$\exp\left(-\frac{\kappa}{\Delta n}\phi_M\right)\left(-\frac{\kappa}{\Delta n}\cos\phi_M - \sin\phi_M\right) t + \exp\left(-\frac{\kappa}{\Delta n}\cos\phi_M\right) = 1, \tag{A.10}$$

$$\exp\left(-\frac{\kappa}{\Delta n}\phi_M\right)\left(-\frac{\kappa}{\Delta n}\sin\phi_M - \cos\phi_M\right) t + \exp\left(-\frac{\kappa}{\Delta n}\sin\phi_M\right) = 0, \tag{A.11}$$

From here one finds that

$$t = \frac{\sin\phi_M}{-\frac{\kappa}{\Delta n}\sin\phi_M - \cos\phi_M} \tag{A.12}$$

so that t can be eliminated and in doing so we obtain

$$1 + \frac{\kappa}{\Delta n}\exp\left(\frac{\kappa}{\Delta n}\phi_M\right)(\cos\phi_M - \sin\phi_M) = 0 \tag{A.13}$$

or alternatively

$$\sqrt{1 + \kappa/\Delta n}\cos\left[\phi_M + \arctan(\kappa/\Delta n)\right]\exp\left(\frac{\kappa}{\Delta n}\phi_M\right) = 1. \tag{A.14}$$

As this equation can not be reduced any further a numerical solver is required to find ϕ_M when $\kappa/\Delta n > 0$, but as soon as ϕ_M is found the projection goes as given by Eq. (A.7).

B Triplicator for lossy material

A triplicator refers to a diffractive element that splits a beam into three equal intensity diffraction orders. In this appendix the design of such a diffractive element is derived analytically and proven to be the best one available while restricted to phase-dependent absorption. The derivation is a direct extension of the derivation for a phase-only design presented in [23]. In short the proof consists of three parts: the first part derives an upper bound, the second part shows when the upper bound results in an equality and the third part uses these results to derive the triplicator profile.

B.1 UPPER BOUND

For brevity of notation we set $\alpha = \kappa/\Delta n$ so that the profile must be of the form

$$t(x) = \exp[(i-\alpha)\phi(x)], \tag{B.1}$$

with $\phi \in [0, 2\pi)$. From here the phase is separated in an even and odd part $\phi = \phi_e + \phi_o$, with $\phi_o \in [-\pi, \pi)$, and the notation is shortened by leaving out the $x-$dependence. With this separation t can be written as

$$t(x) = e^{(i-\alpha)\phi_e}[\cosh(\alpha\phi_o) - \sinh(\alpha\phi_o)](\cos\phi_o + i\sin\phi_o). \tag{B.2}$$

When the grating period is normalized to unity (as can be done without loss of generality), the complex amplitude of the n'th diffraction order is given by

$$T_n = \int_{-1/2}^{1/2} t(x)\exp(-i2\pi nx)\mathrm{d}x. \tag{B.3}$$

The goal is to find the profile $t(x)$ that maximizes the amplitudes of T_0 and $T_{\pm 1}$ while keeping them equal. Computing these three amplitudes by using Eq. (B.2) and crossing out all the integrals over odd functions gives

$$T_0 = \int_{x\in R} \mathrm{d}x + \int_{x\notin R} e^{(i-\alpha)\phi_e}[\cosh(\alpha\phi_o)\cos\phi_o - i\sinh(\alpha\phi_o)\sin\phi_o]\mathrm{d}x \tag{B.4}$$

and

$$\begin{aligned} T_1 = &\int_{x\in R} e^{-i2\pi x}\mathrm{d}x \\ &+ \int_{x\notin R} e^{(i-\alpha)\phi_e}\sin(2\pi x)[i\cosh(\alpha\phi_o)\sin\phi_o - \sinh(\alpha\phi_o)\cos\phi_o]\mathrm{d}x \\ &+ \int_{x\notin R} e^{(i-\alpha)\phi_e}\cos(2\pi x)[\cosh(\alpha\phi_o)\cos\phi_o - i\sinh(\alpha\phi_o)\sin\phi_o]\mathrm{d}x. \end{aligned} \tag{B.5}$$

In these expressions the integration domain R denotes the region where $\phi_e(x) + \phi_o(x) = 0$.

From here on two ambiguities are used to make the solution unique. The first is fixing the phase ambiguity by demanding that $T_1 = -T_{-1}$ so that Eq. (B.5) becomes

$$\begin{aligned} T_1 = &\int_{x\in R} i\sin(2\pi x)\mathrm{d}x \\ &+ \int_{x\notin R} e^{(i-\alpha)\phi_\mathrm{e}}\sin(2\pi x)[i\cosh(\alpha\phi_\mathrm{o})\sin\phi_\mathrm{o} - \sinh(\alpha\phi_\mathrm{o})\cos\phi_\mathrm{o}]\mathrm{d}x. \end{aligned} \tag{B.6}$$

The second ambiguity is that a periodic grating shifted by an arbitrary value remains the same grating. This ambiguity is fixed by demanding that the function is centered and minimal at $x = 0$. To impose this demand the function in Eq. (B.7) and (B.8) is shifted in phase by $-\pi/2$ and the integration domain is set to $x \in [-1/2, 1/2)$, which yields

$$T_0 = 2R + \int_R^{1/2} e^{(i-\alpha)\phi_\mathrm{e}}[\cosh(\alpha\phi_\mathrm{o})\cos\phi_\mathrm{o} - i\sinh(\alpha\phi_\mathrm{o})\sin\phi_\mathrm{o}]\mathrm{d}x \tag{B.7}$$

and

$$\begin{aligned} T_1 =&\sin(2\pi R)/\pi \\ &+ 2\int_R^{1/2} e^{(i-\alpha)\phi_\mathrm{e}}\cos(2\pi x)[i\cosh(\alpha\phi_\mathrm{o})\sin\phi_\mathrm{o} - \sinh(\alpha\phi_\mathrm{o})\cos\phi_\mathrm{o}]\mathrm{d}x. \end{aligned} \tag{B.8}$$

By taking the absolute value of the functions inside the integral shows that the amplitudes of the diffraction orders are bound by

$$|T_0| \leq 2R + \int_R^{1/2} e^{-\alpha\phi_\mathrm{e}}[\cosh(\alpha\phi_\mathrm{o})|\cos\phi_\mathrm{o}| + |\sinh(\alpha\phi_\mathrm{o})\sin\phi_\mathrm{o}|]\mathrm{d}x \tag{B.9}$$

and

$$\begin{aligned} |T_1| \leq&\sin(2\pi R)/\pi \\ &+ 2\int_R^{1/2} e^{-\alpha\phi_\mathrm{e}}\cos(2\pi x)[\cosh(\alpha\phi_\mathrm{o})|\sin\phi_\mathrm{o}| + |\sinh(\alpha\phi_\mathrm{o})\cos\phi_\mathrm{o}|]\mathrm{d}x, \end{aligned} \tag{B.10}$$

respectively.

B.2 CONDITIONS FOR EQUALITY UPPER BOUND

The next step is to find the conditions for which the $\leq$ in Eqs. (B.9) and (B.10) becomes an equality. For this purpose the following notation is introduced:

$$I_1 = I_P + I_Q, \tag{B.11}$$

$$|I_2| = I_{|P|} + I_{|Q|}, \tag{B.12}$$

$$I_P = \int_0^{1/2} |P|\exp(i\phi_p)\mathrm{d}x, \tag{B.13}$$

$$I_{|P|} = \int_0^{1/2} |P|\mathrm{d}x, \tag{B.14}$$

where ϕ_P is the phase of $P(x)$. As

$$|I_1|^2 = |I_P|^2 + |I_Q|^2 + 2|I_P||I_Q|, \tag{B.15}$$
$$|I_2|^2 = I_{|P|}^2 + I_{|Q|}^2 + 2I_{|P|}I_{|P|}, \tag{B.16}$$

can only be a solution of $|I_1|^2 = |I_2|^2$ if and only if

$$|I_P|^2 = I_{|P|}^2 \quad \text{and} \quad |I_Q|^2 = I_{|Q|}^2. \tag{B.17}$$

To find when such an equality is satisfied the functions $|I_P|^2$ and $I_{|P|}^2$ are expressed as a Riemann sum with integration step δ so that,

$$\begin{aligned} |I_P|^2 &= \delta^2 \sum_{k=1}^{N} |P_k|^2 + \delta^2 \sum_{k=1}^{N} \sum_{h\neq k} |P_k||P_h| \exp\left[i\left(\phi_{p,k} - \phi_{p,h}\right)\right] \\ &= \delta^2 \sum_{k=1}^{N} |P_k|^2 + 2\delta^2 \sum_{k=1}^{N} \sum_{h>k} |P_k||P_h| \cos\left(\phi_{p,k} - \phi_{p,h}\right) \end{aligned} \tag{B.18}$$

and

$$I_{|P|}^2 = \delta^2 \sum_{k=1}^{N} |P_k|^2 + 2\delta^2 \sum_{k=1}^{N} \sum_{h>k} |P_k||P_h|. \tag{B.19}$$

By taking the limit $\delta \to 0$ the statement $|I_1|^2 = |I_2|^2$ can only be true if

$$\cos(\phi_{p,k} - \phi_{p,h}) = 1 \quad \forall (h,k), \tag{B.20}$$
$$\cos(\phi_{q,k} - \phi_{q,h}) = 1 \quad \forall (h,k). \tag{B.21}$$

Hence the functions $P(x)$ and $Q(x)$ must be constants. Looking at Eq. (B.9), the function's P and Q are

$$P = e^{(i-\alpha)\phi_e} \cosh(\alpha\phi_o) \cos\phi_o \tag{B.22}$$
$$Q = -ie^{(i-\alpha)\phi_e} \sinh(\alpha\phi_o) \sin\phi_o, \tag{B.23}$$

so that their phase functions are given by

$$\phi_p = \phi_e + \arg(\cos\phi_o) = \phi_e + \phi_{\cos}, \tag{B.24}$$
$$\begin{aligned} \phi_q &= \phi_e + \arg[\sinh(\alpha\phi_o)\sin\phi_o] + 3\pi/2 \\ &= \phi_e + \phi_{\text{sinhsin}} + 3\pi/2. \end{aligned} \tag{B.25}$$

As shown these phase functions must be constant for the equality to hold, i.e.

$$\phi_e + \phi_{\cos} = \Phi_{c1}, \tag{B.26}$$
$$\phi_e + \phi_{\text{sinhsin}} + 3\pi/2 = \Phi_{c2}. \tag{B.27}$$

with Φ_{c1} and Φ_{c2} being constants.

Likewise, doing the same for Eq. (B.10) results in the functions

$$P = e^{(i-\alpha)}\phi_{\mathrm{e}}\cosh(\alpha\phi_{\mathrm{o}})\sin\phi_{\mathrm{o}}\cos(2\pi x), \tag{B.28}$$

$$Q = e^{(i-\alpha)}\phi_{\mathrm{e}}\sinh(\alpha\phi_{\mathrm{o}})\cos\phi_{\mathrm{o}}\cos(2\pi x), \tag{B.29}$$

with phase functions

$$\phi_p = \phi_{\mathrm{e}} + \arg(\sin\phi_{\mathrm{o}}) = \phi_{\mathrm{e}} + \phi_{\mathrm{sin}}, \tag{B.30}$$

$$\begin{aligned}\phi_q &= \phi_{\mathrm{e}} + \arg[\sinh(\alpha\phi_{\mathrm{o}})\cos\phi_{\mathrm{o}} + \pi/2 \\ &= \phi_{\mathrm{e}} + \phi_{\mathrm{sinhcos}} + \pi/2.\end{aligned} \tag{B.31}$$

These should also be constant for the inequality to turn into an equality, i.e.

$$\phi_{\mathrm{e}} + \phi_{\mathrm{sin}} = \Phi_{c3}, \tag{B.32}$$

$$\phi_{\mathrm{e}} + \phi_{\mathrm{sinhcos}} + \pi/2 = \Phi_{c4}, \tag{B.33}$$

with Φ_{c3} and Φ_{c4} being constants.

In summary, the equality sign in (B.10) requires that, in the integration domain $x \in [0, 0.5]$, angles $\phi_{\mathrm{cos}} = \phi_{\mathrm{sin}} = \phi_{\mathrm{sinhsin}} = \phi_{\mathrm{sinhcos}}$ are equal, i.e., they are all either positive or negative valued; then also ϕ_{e} will be constant. This is the same as saying that $\phi_{\mathrm{cos}} = \phi_{\mathrm{sin}}$, or alternatively $\max(\phi_{\mathrm{e}} + \phi_{\mathrm{o}}) - \min(\phi_{\mathrm{e}} + \phi_{\mathrm{o}}) \leq \pi$. When this condition is violated (B.10) will result in a strict inequality and this proof will not yield the ideal profile.

B.3 TRIPLICATOR PROFILE

The conditions required to find the optimum triplicator are known and can now be inserted into Eqs. (B.9) and (B.10) giving

$$\begin{aligned}T_0 = 2R + 2\int_R^{1/2} &\exp(-\alpha\phi_{\mathrm{e}})\exp(i\phi_{\mathrm{cos}}) \\ &\times[\cosh(\alpha\phi_{\mathrm{o}})\cos\phi_{\mathrm{o}} + \sinh(\alpha\phi_{\mathrm{o}})\sin\phi_{\mathrm{o}}]\,\mathrm{d}x\end{aligned} \tag{B.34}$$

and

$$\begin{aligned}T_1 = \sin(2\pi R)/\pi + 2\int_R^{1/2} &\exp(-\alpha\phi_{\mathrm{e}})\exp(i\phi_{\mathrm{cos}})\cos(2\pi x) \\ &\times[\cosh(\alpha\phi_{\mathrm{o}})\sin\phi_{\mathrm{o}} + \sinh(\alpha\phi_{\mathrm{o}})\cos\phi_{\mathrm{o}}]\,\mathrm{d}x,\end{aligned} \tag{B.35}$$

in which it was used that $\arg(\cos\phi_{\mathrm{o}}) = \arg(\sin\phi_{\mathrm{o}}) = \phi_{\mathrm{cos}}$ and $\phi_{\mathrm{e}} = \Phi_c$.

The optimum triplicator is found by maximizing the function $F(\phi_{\mathrm{o}}) = |T_0| + \alpha|T_1|$ in which a is a yet to be determined constant. At the functions maximum the following relation should hold:

$$\delta F = \lim_{\epsilon\to 0}[F(\phi_{\mathrm{o}} + \epsilon) - F(\phi_{\mathrm{o}})] = 0. \tag{B.36}$$

Inserting (B.9) and (B.10) into $F(\phi_o)$ yields

$$\begin{aligned} F(\phi_o) = 2R + a\sin(2\pi R)/\pi + 2\int_R^{1/2} & \exp(-\alpha\phi_e)\exp(i\phi_{cos}) \\ & \times [\cosh(\alpha\phi_0)\cos\phi_o + \sinh(\alpha\phi_o)\sin\phi_o]\,dx \\ - 2a\int_R^{1/2} & \exp(-\alpha\phi_e)\exp(i\phi_{cos})\cos(2\pi x) \\ & \times [\cosh(\alpha\phi_o)\sin\phi_o + \sinh(\alpha\phi_o)\cos\phi_o]\,dx. \end{aligned} \tag{B.37}$$

The term $F(\phi_o + \epsilon)$ is approximated by a first order Taylor series as

$$\begin{aligned} F(\phi_o + \epsilon) \approx 2R + a\sin(2\pi R)/\pi + 2\int_R^{1/2} & \exp(-\alpha\phi_e) \\ & \times \{[\cosh(\alpha\phi_o) + \epsilon\alpha\sinh(\alpha\phi_o)](\cos\phi_o - \epsilon\sin\phi_o) \\ & + [\sinh(\alpha\phi_o) + \epsilon\alpha\cosh(\alpha\phi_o)(\sin\phi_o + \epsilon\cos\phi_o)\}\,dx \\ - 2a\int_R^{1/2} & \exp(-\alpha\phi_e)\cos(2\pi x) \\ & \times \{[\cosh(\alpha\phi_o) + \epsilon\alpha\sinh(\alpha\phi_o)](\sin\phi_o + \epsilon\cos\phi_o) \\ & + [\sinh(\alpha\phi_o) + \epsilon\alpha\cosh(\alpha\phi_o)](\cos\phi_o - \epsilon\sin\phi_o)\}\,dx. \end{aligned} \tag{B.38}$$

Combining these expressions to compute δF gives

$$\begin{aligned} \delta F = 2\epsilon\int_R^{1/2} & \exp(-\alpha\phi_e) \\ & \times \{-\cosh(\alpha\phi_o)\sin\phi_o + \alpha\sinh(\alpha\phi_o)\cos\phi_o \\ & + \sinh(\alpha\phi_o)\cos\phi_o + \alpha\cosh(\alpha\phi_o)\sin\phi_o \\ & - a\cos(2\pi x)[\cosh(\alpha\phi_o)\cos\phi_o + \alpha\sinh(\alpha\phi_o)\sin\phi_o \\ & - \sinh(\alpha\phi_o)\sin\phi_o + \alpha\cosh(\alpha\phi_o)\cos\phi_o]\}\,dx = 0. \end{aligned} \tag{B.39}$$

Dropping the integral gives us the analytical equation from which the optimum triplicator profile will be determined:

$$\begin{aligned} & (1-\alpha)[\cosh(\alpha\phi_o) - a\cos(2\pi x)\sinh(\alpha\phi_o)]\sin\phi_o \\ & = (1+\alpha)[\sinh(\alpha\phi_o) - a\cos(2\pi x)\cosh(\alpha\phi_o)]\cos\phi_o. \end{aligned} \tag{B.40}$$

The phase constant ϕ_e needs to be fixed so that $\phi_e + \phi_o \in [0, 2\pi)$ and efficiency maximized. The only logical choice is $\phi_e = -\min[\phi_o(x)], x \in [R, 1/2)$ as any other choice will cause absorption to eat up efficiency. With this choice the proof is valid if $0 \le \phi(x) \le \pi$ and the phase function is given by

$$\phi(x) = \begin{cases} 0 & \text{if } |x| < R \\ \phi_o + \phi_e & \text{if } R \le |x| < 1/2, \end{cases} \tag{B.41}$$

There are two other constants that have to be fixed, the first is the region where R phase is zero and the other is the value α such that the amplitudes of the diffraction orders are equal, i.e. $|T_0| = |T_1|$. This is done by solving Eq. (B.40) and searching for the values a and R that would result in an optimum efficiency triplicator profile.

In the special case that no absorption takes place, i.e $\alpha = 0$, (B.40) reduces to

$$\sin\phi_o = -a\cos(2\pi x)\cos\phi_o, \tag{B.42}$$

or

$$\phi_o = -\arctan\left[a\cos(2\pi x)\right], \tag{B.43}$$

so that one ends up with the same profile as derived in [23] be it spatially shifted to be minimal at $x = 0$.

C Gaussian Shell Model Kernel

In this section the goal is to show that the Gaussian Shell Model (GSM) represented by a Hermite Gaussian basis can also be written as a sum of shifted elementary Gaussian modes without loss of generality. Only the field along the x-coordinate at constant plane z is considered for simplicity.

For any CSD is non-negative definite can be represented as an coherent mode representation [2]

$$W(x_1, x_2) = \sum_{m=0}^{\infty} a_m \psi_m^*(x_1)\psi_m(x_2), \tag{C.1}$$

The eigenvalues and eigenfunctions are determined by solving the Fredholm integral equation

$$\int_{-\infty}^{\infty} W(x_1, x_2)\psi_m(x_1)\mathrm{d}x_1 = a_m\psi_m(x_2). \tag{C.2}$$

The eigenfunctions ψ_m themselves are orthonormal as

$$\int_{-\infty}^{\infty} \psi_m^*(x)\psi_n(x)\mathrm{d}x = \delta_{mn} \tag{C.3}$$

with δ_{mn} the Kronecker delta function.

For a Gaussian Shell model source both the spectral density and spatial degree of coherence are Gaussian functions

$$S(x) = S_0 \exp\left(-\frac{2x^2}{w_0^2}\right), \tag{C.4}$$

$$\mu(\Delta x) = \exp\left[-\frac{(x_2 - x_1)^2}{2\sigma_0^2}\right], \tag{C.5}$$

$$W(x_1, x_2) = \sqrt{S(x_1)S(x_2)}\mu(\Delta x). \tag{C.6}$$

Solving the Fredholm integral equation for such a source gives an analytical expression for the eigenvalues and eigenfunction [46]. The eigenfunctions are the orthonormal Hermite Gaussian functions given by

$$\psi_m(x) = \left(\frac{2}{\pi}\right)^{1/4} \frac{1}{\sqrt{2^m m! w_\mathrm{c}}} H_m\left(\frac{\sqrt{2}x}{w_\mathrm{c}}\right) \exp\left(-\frac{x^2}{w_\mathrm{c}^2}\right), \tag{C.7}$$

with constant $w_\mathrm{c} = \sqrt{\beta}w_0$, w_0 the beam width and $0 \leq \beta \leq 1$ a measure for coherence. If $\beta = 1$ the field is fully coherent and only one mode (Gaussian) mode is needed to represent it a completely incoherent field, $\beta = 0$, requires infinite Hermite Gaussian modes to be represented. The weight of each of these modes are given by

the eigenvalue a_m

$$a_m = S_0 \frac{\sqrt{2\pi} w_0}{1 + 1/\beta} \left(\frac{1-\beta}{1+\beta} \right)^m. \tag{C.8}$$

Since the CSD is non-negative definite, then it can also be written in the form [69,70]

$$W(x_1, x_2) = \int_{-\infty}^{\infty} p(v_x) H^*(x_1, v_x) H(x_2, v_x) \mathrm{d}v_x \tag{C.9}$$

where $p(v_x)$ is a non-negative weight function and $H(x, v_x)$ an arbitrary kernel. More specifically the kernel can be represented by a set of eigenfunctions [71]

$$W(x_1, x_2) = \int_{-\infty}^{\infty} L^*(x_1, v_x) L(x_2, v_x) \mathrm{d}v_x, \tag{C.10}$$

$$L(x, v_x) = \sqrt{p(v_x)} H(x, v_x) = \sum_{m=0}^{\infty} \sqrt{a_m} \psi_m^*(x) \Phi_m(v_x). \tag{C.11}$$

with Φ_m an arbitrary chosen set of orthonormal basis functions that form a complete set and ψ the same eigenfunctions as before. The arbitrary choice of Ψ_m allows one to make the choice $\Phi_m(v_x) = \sqrt{|\alpha|} \psi_m(\alpha v_x)$ with $\psi_m(x)$ being the Hermite Gaussian eigenfunctions (Eq. (C.7)) for Gaussian Shell model sources. The value for the real constant α can be chosen freely as it merely scales the Hermite Gaussian functions that remain orthonormal regardless the choice for α. It is from Eq. (C.11) that the Gaussian elementary mode representation will be derived. For this purpose the value of α will be kept as a free parameter to simplify the notation of the equations later on.

Inserting the eigenfunctions Eq. (C.7) and eigenvalues Eq. (C.8) into the kernel (Eq. (C.11)) with the choice $\Phi_m(v_x) = \sqrt{|\alpha|} \psi_m(\alpha v_x)$ yields

$$L(x, v_x) = \left(\frac{2 S_0 w_0}{1 + 1/\beta} \right)^{1/2} \left(\frac{2}{\pi} \right)^{1/4} \frac{\sqrt{|\alpha|}}{w_{\mathrm{c}}} \exp\left(-\frac{x^2 + \alpha^2 v_x^2}{w_{\mathrm{c}}^2} \right) F(x, v_x) \tag{C.12}$$

$$F(x, v_x) = \sum_{m=0}^{\infty} \frac{1}{2^m m!} \left(\frac{1-\beta}{1+\beta} \right)^{m/2} H_m\left(\frac{\sqrt{2} x}{w_{\mathrm{c}}} \right) H_m\left(\frac{\sqrt{2} \alpha v_x}{w_{\mathrm{c}}} \right). \tag{C.13}$$

To compute the summation over all Hermite Gaussian modes the function $F(x, v_x)$ is rewritten in the compact form

$$F(x, v_x) = \sum_{m=0}^{\infty} H_m(x) H_m(y) \frac{t^m}{2^m m!}, \tag{C.14}$$

where $x = \sqrt{2} x / \omega_c$, $y = \sqrt{2} v_x / w_{\mathrm{c}}$ and

$$t = \left(\frac{1-\beta}{1+\beta} \right)^{1/2}. \tag{C.15}$$

Next the Hermite Gaussian mode H_m is rewritten in its integral form [72]

$$H_m(x) = \frac{1}{\sqrt{\pi}} \int_{-\infty}^{\infty} (-2ix')^m \exp\left[-(x'^2 - ix)^2 \right] \mathrm{d}x', \tag{C.16}$$

so that upon inserting Eq. C.16 into Eq. C.14 the integral form can be used to compute the summation over all Hermite Gaussian modes

$$
\begin{aligned}
F(x, x_v) &= \sum_{m=0}^{\infty} H_m(x) H_m(y) \frac{t^m}{2^m m!} \\
&= \sum_{m=0}^{\infty} \frac{t^m}{2^m m!} \frac{1}{\pi} \int_{-\infty}^{\infty} \int_{-\infty}^{\infty} (-2ix')^m \exp\left[-(x'^2 - ix)^2\right] (-2iy')^m \exp\left[-(y'^2 - iy)^2\right] \mathrm{d}x' \mathrm{d}y' \\
&= \frac{1}{\pi} \int_{-\infty}^{\infty} \int_{-\infty}^{\infty} \exp\left[-(x'^2 - ix)^2 - (y'^2 - iy)^2\right] \sum_{m=0}^{\infty} \frac{(-2ix'y't)^m}{m!} \mathrm{d}x' \mathrm{d}y' \\
&= \frac{1}{\pi} \int_{-\infty}^{\infty} \int_{-\infty}^{\infty} \exp\left[-(x'^2 - ix)^2 - (y'^2 - iy)^2\right] \exp\left[-2tx'y'\right] \mathrm{d}x' \mathrm{d}y' \qquad \text{(C.17)} \\
&= \frac{1}{\pi} \int_{-\infty}^{\infty} \exp\left[-(x'^2 - ix)^2 - 2itx'y + tx'^2\right] \int_{-\infty}^{\infty} \exp\left[-(y' - iy + tx')^2\right] \mathrm{d}x' \mathrm{d}y' \\
&= \frac{1}{\pi} \int_{-\infty}^{\infty} \exp\left[-(1 - t^2)x'^2 + x^2 + 2ix'(x - ty)\right] \mathrm{d}x' \sqrt{\pi} \\
&= \frac{1}{\sqrt{\pi}} \exp\left[x^2\right] \int_{-\infty}^{\infty} \exp\left[-P^2 + 2iP \frac{x - ty}{\sqrt{1 - t^2}}\right] \frac{\mathrm{d}P}{\sqrt{1 - t^2}}
\end{aligned}
$$

where $P = \sqrt{1 - t^2} x'$. This equation can be further simplified by noting that the exponential has an alternative expression is of the integral form [72]

$$
\exp\left(-x^2\right) = \frac{1}{\sqrt{\pi}} \int_{-\infty}^{\infty} \exp\left[-x'^2 + 2ixx'\right] \mathrm{d}x'. \qquad \text{(C.18)}
$$

Note that this is a different representation than $H_0(x)$ from Eq. (C.16). Using Eq. (C.18) to simplify Eq. (C.17) gives

$$
\begin{aligned}
F(x, x_v) &= \sum_{m=0}^{\infty} H_m(x) H_m(y) \frac{t^m}{2^m m!}, \\
&= \frac{1}{\sqrt{1 - t^2}} \exp\left[x^2 - \frac{(x - ty)^2}{1 - t^2}\right], \qquad \text{(C.19)} \\
&= \frac{1}{\sqrt{1 - t^2}} \exp\left[\frac{2txy - t^2(x^2 + y^2)}{1 - t^2}\right].
\end{aligned}
$$

Substituting $x = \sqrt{2}x/\omega_c$, $y = \sqrt{2}\alpha v_x / w_\mathrm{c}$ back into Eq. C.19 and combining this

with Eq. C.13 gives the kernel in its new form as

$$\begin{aligned} L(x,v_x) &= \left(\frac{2S_0w_0}{1+1/\beta}\right)^{1/2}\left(\frac{2}{\pi}\right)^{1/4}\frac{\sqrt{|\alpha|}}{w_{\,\mathrm{c}}}\exp\left(-\frac{x^2+\alpha^2v_x^2}{w_{\mathrm{c}}^2}\right) \\ &\quad \frac{1}{\sqrt{1-t^2}}\exp\left[2\frac{2tx\alpha v_x - t^2(x^2+\alpha^2v_x^2)}{w_{\mathrm{c}}^2(1-t^2)}\right] \\ &= \left(\frac{2S_0w_0}{1+1/\beta}\right)^{1/2}\left(\frac{2}{\pi}\right)^{1/4}\frac{\sqrt{|\alpha|}}{\sqrt{1-t^2}w_{\,\mathrm{c}}}G(x,v_x). \end{aligned} \tag{C.20}$$

The only thing to be done is to rewrite this equation and put it in the right form. By taking all the exponential together into the function $G(x,v_x)$ one can reorder it as

$$\begin{aligned} G(x,v_x) &= \exp\left(-\frac{x^2+\alpha^2v_x^2}{w_{\mathrm{c}}^2}+2\frac{2tx\alpha v_x - t^2(x^2+\alpha^2v_x^2)}{w_{\mathrm{c}}^2(1-t^2)}\right) \\ &= \exp\left(-\frac{(1-t^2)(x^2+\alpha^2v_x^2)-4tx\alpha v_x+2t^2x^2+2t^2\alpha^2v_x^2}{(1-t^2)w_{\mathrm{c}}^2}\right) \\ &= \exp\left(-\frac{(1+t^2)(x^2+\alpha^2v_x^2)-4tx\alpha v_x}{(1-t^2)w_{\mathrm{c}}^2}\right) \\ &= \exp\left(-\frac{(1+t^2)}{(1-t^2)}\frac{\left(x+\frac{2t\alpha v_x}{1+t^2}\right)^2+\left(1-\frac{4t^2}{(1+t^2)^2}\right)\alpha^2v_x^2}{w_{\mathrm{c}}^2}\right). \end{aligned} \tag{C.21}$$

By making use of Eq. C.15 we find that

$$\frac{1+t^2}{1-t^2} = \frac{1}{\beta}, \tag{C.22}$$

$$\frac{2t}{1+t^2} = \sqrt{1-\beta^2}, \tag{C.23}$$

so that Eq. C.21 can be further reduced to

$$G(x,v_x) = \exp\left(-\frac{\left(x+\sqrt{1-\beta^2}\alpha v_x\right)^2}{\beta w_{\mathrm{c}}^2}\right)\exp\left(-\frac{\beta\alpha^2v_x^2}{w_{\mathrm{c}}^2}\right). \tag{C.24}$$

Inserting this back into Eq. (C.20) gives the kernel in the form

$$L(x,v_x) = \left(\frac{2S_0w_0}{1+1/\beta}\right)^{1/2}\left(\frac{2}{\pi}\right)^{1/4}\frac{\sqrt{|\alpha|}\exp\left(-\frac{\beta\alpha^2v_x^2}{w_{\mathrm{c}}^2}\right)}{w_{\mathrm{c}}\sqrt{1-t^2}}\exp\left(-\frac{\left(x+\sqrt{1-\beta^2}\alpha v_x\right)^2}{\beta w_{\mathrm{c}}^2}\right) \tag{C.25}$$

As noted before the constant α is a free parameter while $w_{\mathrm{c}} = \sqrt{\beta}w_0$. By choosing $\alpha = -1/\sqrt{1-\beta^2}$ the kernel is represented by a superposition of shifted Gaussian

elementary modes

$$L(x,v_x) = \left(\frac{2S_0 w_0}{\sqrt{1-\beta^2}(1+1/\beta)}\right)^{1/2}\left(\frac{2}{\pi}\right)^{1/4}\frac{\exp\left(-\frac{\beta v_x^2}{(1-\beta^2)w_c^2}\right)}{w_c\sqrt{1-t^2}}\exp\left(-\frac{(x-v_x)^2}{\beta w_c^2}\right),$$
$$= \left(\frac{2S_0\beta w_0}{\sqrt{1-\beta^2}(1+\beta)}\cdot\frac{1+\beta}{2\beta^2 w_0^2}\right)^{1/2}\left(\frac{2}{\pi}\right)^{1/4}\exp\left(-\frac{v_x^2}{w_p^2}\right)\exp\left(-\frac{(x-v_x)^2}{w_e^2}\right), \tag{C.26}$$
$$= \frac{\sqrt{S_0}}{(1-\beta^2)^{1/4}}\exp\left(-\frac{v_x^2}{w_p^2}\right)\left(\frac{2}{\pi}\right)^{1/4}\frac{1}{\sqrt{w_e}}\exp\left(-\frac{(x-v_x)^2}{w_e^2}\right). \tag{C.27}$$

In here the constants w_p and w_e

$$w_p = \sqrt{1-\beta^2}w_0, \tag{C.28}$$
$$w_e = \beta w_0, \tag{C.29}$$

represent the width of the weight function and elementary mode respectively.

Introducing the normalized elementary Gaussian mode $e(x-v_x)$ brings the kernel to its final form

$$L(x,x_v) = \sqrt{p(v_x)}e(x-v_x), \tag{C.30}$$

with

$$e(x) = \left(\frac{2}{\pi}\right)^{1/4}\frac{1}{\sqrt{w_e}}\exp\left(-\frac{x^2}{w_e^2}\right), \tag{C.31}$$

and

$$p(v_x) = p_0\exp\left(-\frac{2v_x^2}{w_p^2}\right), \tag{C.32}$$
$$p_0 = \frac{S_0}{\sqrt{1-\beta^2}}. \tag{C.33}$$

It is this kernel that is used to describe the GSM sources by means of shifted Gaussian elementary modes.

If the found expression is inserted into the CSD then an expression for the coherence width can be found. Inserting Eq. (C.30) into Eq. (C.9) yields

$$W(x_1,x_2) = \frac{p_0}{w_e}\left(\frac{2}{\pi}\right)^{1/2}\int_{-\infty}^{\infty}\exp\left(-\frac{2v_x^2}{w_p^2}\right)\exp\left(-\frac{(x_1-v_x)^2}{w_e^2}\right)\exp\left(-\frac{(x_2-v_x)^2}{w_e^2}\right)\mathrm{d}v_x$$
$$= \frac{S_0}{\sqrt{1-\beta^2}w_e\sqrt{1/w_p^2+1/w_e^2}}\exp\left(-\frac{w_p^2(x_1-x_2)^2+2w_e(x_1^2+x_2^2)}{2w_e^2(w_e^2+w_p^2)}\right) \tag{C.34}$$
$$= S_0\exp\left(-\frac{x_1^2+x_2^2}{w_0^2}\right)\exp\left(-\frac{(x_1-x_2)^2}{2\sigma_0^2}\right),$$

which is exactly Eq. (C.6), the Gaussian Shell Model source that one started with. From here it can also be seen that the coherence width is given by $\sigma_0 = \frac{w_e}{w_p} w_0 = \frac{\beta}{\sqrt{1-\beta^2}} w_0$ or put differently $\beta = 1/\sqrt{1 + (w_0/\sigma_0)^2}$.

D Focal Spot Size with Gracing Mirrors

For standard optical systems the Rayleigh limit describes the size of the focal spot for a lens with a rectangular aperture of size $D \times D$ and focal length F as

$$\delta x = \frac{\lambda F}{D}. \tag{D.1}$$

When grazing incidence mirrors (also named Kirkpatrick-Baez mirrors) are considered D describes the effective aperture. As will be shown the effective aperture is slightly larger than the standard estimation [73,74] $D \approx \theta L$ where θ is the grazing angle and L the length of the KB mirror.

Figure D.1 shows the (exaggerated) geometry used to compute the effective aperture size. In this geometry the origin lies at the center of the KB mirror so that the focus is located at (X, Y) with $X = F\cos\theta$ and $Y = F\sin\theta$. The plane in which the effective window size is measured goes through lies a distance F after the focus and perpendicularly to the local optical axis. The marginal ray shown in orange defines the effective aperture size at this plane.

To compute D some additional notation that is shown in Figure D.2 is introduced. The coordinates (X_1, Y_1) and (X_2, Y_2) denote the end points of the aperture and will be calculated to determine D. There are two similar sets of triangles visible in the figure, one set consisting of solid lines and another set consisting of dashed lines. The triangles share the same slope indicated by the orange line which consists of two sections with lengths R_1 and R_1'. By use of similar triangles knowledge of length P_1 yields the size of R_1' as

$$R_1' = R_1 \frac{F}{P_1}. \tag{D.2}$$

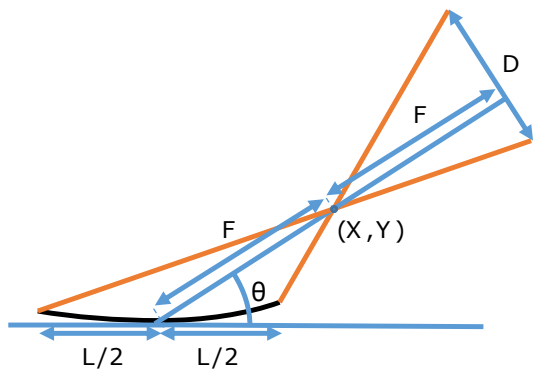

Figure D.1: Sketch of the KB mirror used to compute effective aperture size D. *adapted from Paper **IV**.*

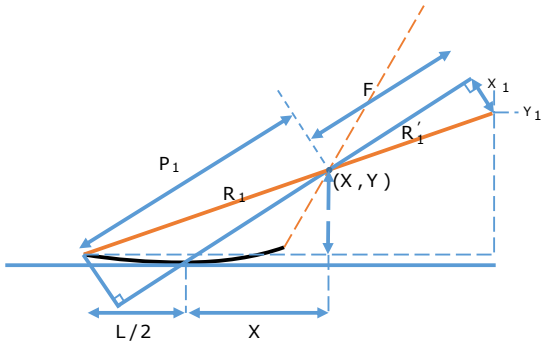

Figure D.2: Same sketch of the setup but with additional visual aid to compute P_1 *adapted from Paper* ***IV***.

By use of the smaller triangle and larger dashed triangle the location of (X_1, Y_1) is given by:

$$X_1 = (X + L/2)\,(1 + F/P_1) - L/2, \tag{D.3}$$
$$Y_1 = (Y - \Delta h_1)\,(1 + F/P_1) + \Delta h_1, \tag{D.4}$$

where $1 + F/P_1$ is the ratio by which the larger triangle is larger then the smaller triangle with height $Y - \Delta h$ inside of it.

From Figure D.3 it follows that P_1 is given by

$$P_1 = Q_1 + F, \tag{D.5}$$

where

$$Q_1 = \sqrt{\Delta h_1^2 + L^2/4}\cos\alpha_1 \tag{D.6}$$
$$\alpha_1 = \theta + \arctan\left(2\Delta h_1/L\right), \tag{D.7}$$

so that all information is known to compute (X_1, Y_1).

Using the notation of Figure D.4 and similar reasoning one can compute (X_2, Y_2). From this figure it follows that

$$X_2 = (X - L/2)\,(1 + F/P_2) + L/2, \tag{D.8}$$
$$Y_2 = (Y - \Delta h_2)\,(1 + F/P_2) + \Delta h_2, \tag{D.9}$$

with

$$P_2 = F - Q_2, \tag{D.10}$$
$$Q_2 = \sqrt{\Delta h_2^2 + L^2/4}\cos\alpha_2, \tag{D.11}$$
$$\alpha_2 = \theta - \arctan\left(2\Delta h_2/L\right), \tag{D.12}$$

so that the effective window size is given by

$$D = \sqrt{(X_2 - X_1)^2 + (Y_2 - Y_1)^2}. \tag{D.13}$$

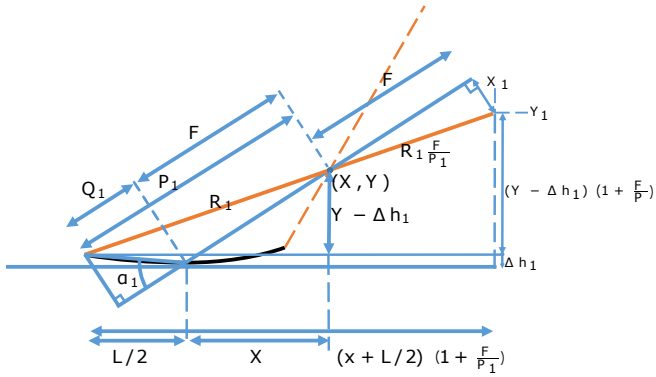

Figure D.3: Visual aid used to compute (X_1, Y_1) *adapted from Paper **IV**.*

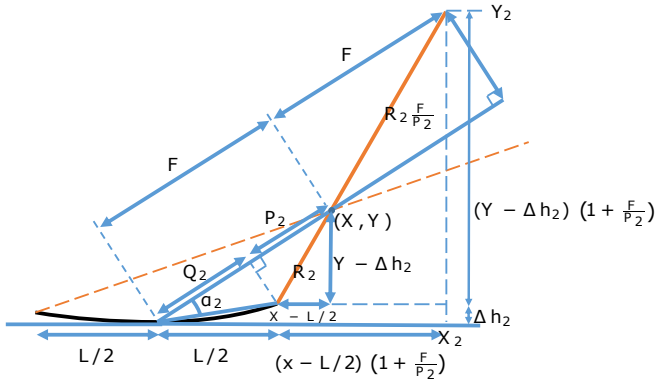

Figure D.4: The KB mirror with the visual aid used for computing (X_2, Y_2) *adapted from Paper **IV**.*

ANTONIE DANIËL VERHOEVEN

The first part of this work describes a general upper bound theorem. This theorem is used to investigate and improve the Iterative Fourier Transform design method for the design of diffractive elements made with absorbing media.

The second part of the work covers spatial coherence theory for x-ray sources and some field propagation methods. These are used for determining the focal spot of an Free Electron Laser grazing mirror beamline setup.

UNIVERSITY OF
EASTERN FINLAND

uef.fi

PUBLICATIONS OF
THE UNIVERSITY OF EASTERN FINLAND
Dissertations in Forestry and Natural Sciences

ISBN 978-952-61-3289-7
ISSN 1798-5668